Ageing studies for the ATLAS MDT Muonchambers and development of a gas filter to prevent drift tube ageing

DISSERTATION

zur

Erlangung des Doktorgrades

der

Fakultät für Mathematik und Physik

der

Albert-Ludwigs-Universität
Freiburg im Breisgau

vorgelegt von

Stefan König

Januar 2008

Dekan:	Prof. Dr. J. Flum
Referent:	Prof. Dr. G. Herten
Korreferent:	Prof. Dr. K. Jakobs
Tag der mündlichen Prüfung:	19. Februar 2008

Ageing studies for the ATLAS MDT Muonchambers and development of a gas filter to prevent drift tube ageing

by

Stefan König

January 2008

Universität
Freiburg im Breisgau

Fakultät für Physik
und Mathematik

Abstract

The muon spectrometer of the ATLAS detector, which is currently assembled at the LHC accelerator at CERN, uses drift tubes as basic detection elements over most of the solid angle. The performance of these monitored drift tubes (MDTs), in particular their spatial resolution of 80 μm, determines the precision of the spectrometer. If ageing effects occur, the precision of the drift tubes will be degraded. Hence ageing effects have to be minimized or avoided altogether if possible. Even with a gas mixture of Ar:CO_2 = 93 : 7, which was selected for its good ageing properties, ageing effects were observed in test systems. They were caused by small amounts of impurities, in particular volatile silicon compounds. Systematic studies revealed the required impurity levels deteriorating the drift tubes to be well below 1 ppm.

Many components of the ATLAS MDT gas system are supplied by industry. In a newly designed ageing experiment in Freiburg these components were validated for their use in ATLAS. With a fully assembled ATLAS gas distribution rack as test component ageing effects were observed. It was therefore decided to install gas filters in the gas distribution lines to remove volatile silicon compounds efficiently from the gas mixture. Finally a filter was designed that can adsorb up to 5.5 g of volatile silicon compounds, hereby reducing the impurities in the outlet gas mixture to less than 30 ppb.

Contents

Chapter 1

Introduction

At the moment particle physicists all over the world are looking expectantly towards CERN[1], close to Geneva in Switzerland. There, the LHC accelerator and its experiments were assembled and are now almost ready to start operations. Once started the standard model of particle physics will be explored at energy densities never reached before.
In section 1.1 this standard theory is briefly outlined. Section 1.2 describes the LHC accelerator, while in section 1.3 one of its experiments, the ATLAS detector, is introduced. After a short look at the physics goals of ATLAS and LHC in section 1.4, the goal and structure of this dissertation is explained in section 1.5.

1.1 The Standard Model

At present, all matter in the universe and their interactions are explained by a quantum field theory, the **Standard Model** of particle physics. In this theory all observable matter is built from 12 elementary particles (and their antiparticles). These 12 particles can be separated into quarks and leptons. Each of these groups consists of 6 particles that can be ordered further in three families each:

$$\begin{pmatrix} \nu_e \\ e \end{pmatrix} \quad \begin{pmatrix} \nu_\mu \\ \mu \end{pmatrix} \quad \begin{pmatrix} \nu_\tau \\ \tau \end{pmatrix} \qquad \text{Leptons}$$

$$\begin{pmatrix} u \\ d \end{pmatrix} \quad \begin{pmatrix} c \\ s \end{pmatrix} \quad \begin{pmatrix} t \\ b \end{pmatrix} \qquad \text{Quarks}$$

The leptons have electrical charge of either -1 (electron e, myon μ and tau τ) or 0 (for the associated neutrinos ν_e, ν_μ and ν_τ) in units of the elementary charge. The charges of the quarks are fractions of the elementary charge, namely $+\frac{2}{3}$ for the up-type quarks (**u**p, **c**harme and **t**op) and $-\frac{1}{3}$ for the down-type quarks (**d**own, **s**trange and **b**ottom). Leptons and quarks are particles with a spin of $\frac{1}{2}\hbar$, therefore they are fermions. Their masses span several orders of magnitude. The lightest

[1] The European center for particle physics

particles are the neutrinos that were assumed as massless in the past. But recent measurements attribute mass to the neutrinos with an upper limit of 1 eV [1]. On the other end of the mass scale the top quark was measured at Fermilab[2] to have a mass of about 174 GeV.
The fermions have certain attributes to which forces can couple. If a particle has for example electrical charge it interacts via the electromagnetic force. All fermionic particles besides the neutrinos have this property. Other properties of the particles are the weak and the strong charge, to which the weak and strong interactions couple. All the fermions have a weak charge, but only the quarks carry the strong charge (or colour charge). In the standard model these interactions are explained by the exchange of other types of particles, the so called gauge bosons. For the electromagnetic interaction there is only one gauge boson, the photon. The weak interaction needs three gauge bosons ($W^{\pm}$ and Z), while the strong interaction requires 8 gauge bosons, the gluons. Since the $W^{\pm}$ carry electrical charges they are allowed to interact among themselves via the electromagnetic force (Triple-gauge-coupling), an experimentally very well confirmed prediction of the standard model. Furthermore the gluons itself carry strong charges and therefore self interactions among gluons are also possible in theory. The experimental verification with the production of quark-gluon plasmas was a further success of the standard model. Likewise the discovery of the $W^{\pm}$ and the Z with the LEP accelerator at CERN in 1983.

1.1.1 Unanswered questions and problems

Although the standard model is the most successful theory in the history of physics, there remain many unanswered questions and problems:

- All standard model particles are massless in theory. One possibility to acquire mass is given by the interaction with a new field, the Higgs field. The Higgs field is connected with at least one new particle, the Higgs boson. This particle has not been found yet.

- Although gravitation does not play an important role in the field of particle physics, it has a big impact on our every day life. Unfortunately there are still unsolved difficulties to include this fourth interaction into the standard model.

- In the standard model there are 21 free parameters with values that seem arbitrary. Is there a smaller subset of free parameters? Why are there exactly three generations of quarks and leptons? For many of these fundamental question the standard model has no answer.

- Particle physicists all over the world are looking for the higgs boson. But even if this particle is found, one major problem remains: The contribution of loop-corrections to the higgs mass are such, that they lead to a very high

[2]Fermilab: Particle physics institute near Chicago, Illinois, USA. Currently the Tevatron at Fermilab accelerates protons and anti-protons to $\sqrt{s} = 1.96$ TeV for two experiment: CDF and D0

value (close to the Planck scale at 10^{16} GeV). But in contrast it is assumed from electroweak fits, that the real Higgs mass is in the region of 130 GeV. The huge difference between the two scales is called the *hierarchy problem*

- The *hierarchy problem* could be solved when radiative corrections are considered. But in this case the radiative corrections from different processes have to be identical with an accuracy of 14 digits even without a fundamental connection between the processes. This is the so called *fine tuning problem*.

Super Symmetry (*SUSY*)

With or without the Higgs boson, the standard model can not be the final theory. There must be a more fundamental theory to which the standard model is only a "low energy" approximation. One candidate for an extension of the standard model which solves some of its problems is *Super Symmetry*. With this new symmetry principle each standard model particle has a super symmetric partner particle. *Super Symmetry* is a symmetry between fermions and bosons. Each fermion has a partner boson and vice versa. With this concept, the hierarchy and fine tuning problem can be solved (super symmetry makes the fundamental connection between the cancelling processes), but other problems remain. A handicap of *Super Symmetry* is its more than 100 free parameters, so it is often analysed as MSSM[3], where a certain number of parameters are fixed.
Super Symmetry is only one of many possible theories. At the moment nobody can tell with confidence which theory is right. Now it is time for the particle physics experiments to chart the course for the future. Two of them are close to completion at the LHC accelerator ring at CERN ...

1.2 The Large Hadron Collider: LHC

In November 2000 it was decided to shut down the LEP accelerator and its experiments ALEPH, DELPHI, L3 and OPAL at CERN, although some of the experiments claimed to have seen hints for the Higgs boson. The reason for the shut-down of LEP was its replacement by the LHC, the next generation particle accelerator. In LEP electrons and positrons were accelerated up to an energy of 105 GeV in a synchrotron with 27 km circumference. At this beam energy the energy loss of the accelerated particles due to synchrotron radiation is substantial. Hence the beam is not very stable and the luminosity therefore rather low. So a lot of running time would have been needed to verify or falsify these hints for new physics.
After the dismantling of LEP the old tunnel was used for the installation of the LHC accelerator. At LHC, protons which have 2000 times the mass of electrons, are accelerated. Since the energy loss due to synchrotron radiation grows with γ^4 ($\gamma = E/mc^2$ for particles with energy E and mass m), this effect is almost negligible at LHC. Thus a beam energy of 7 TeV will be reached during the operation

[3] **M**ininmal **S**upersymmetric **S**tandard **M**odel

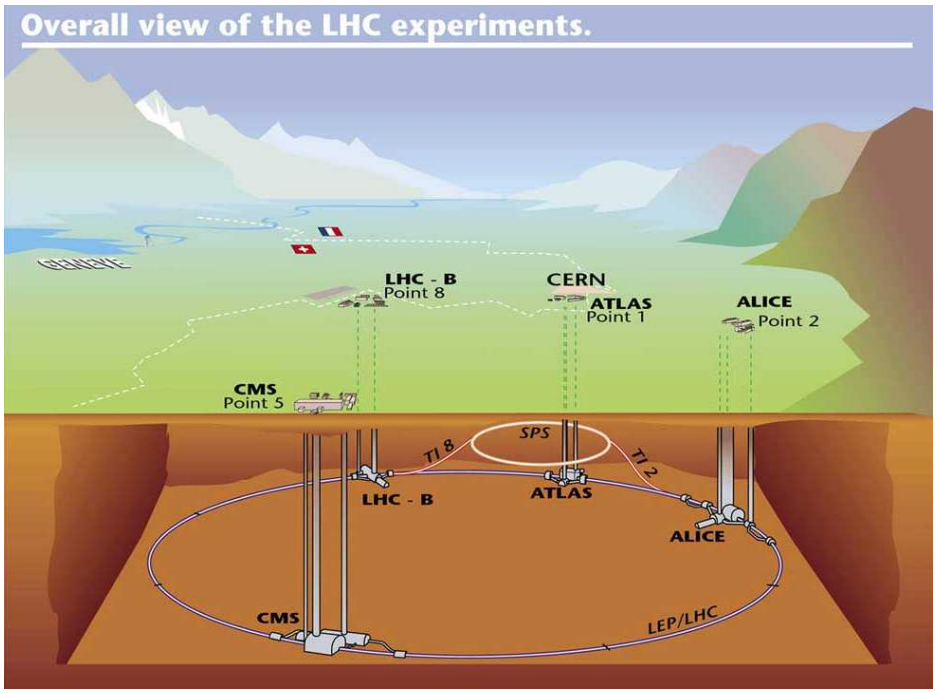

Figure 1.1: *View of the LHC accelerator and its underground experiments at CERN [3]. Before the injection into the LHC accelerator ring the protons will pass several stages of acceleration. In the last stage before the LHC, the SPS will accelerate the particles to* 450 *GeV.*

beginning in 2008. With a centre of mass energy of $\sqrt{s} = 14$ TeV the LHC will surpass the TeVatron - currently the accelerator with the highest beam energy - by a factor of 7. The protons in the beam are clustered in bunches with a length of 7.7 cm. With a bunch crossing time of 25 ns the design luminosity of $10^{34}/(\mathrm{s} \cdot \mathrm{cm}^2)$ is reached, but in the start up phase only 10% of it is aimed for. To force the proton beam onto a circular orbit the charged particles are focused with very high magnetic fields of up to 8.33 T. These fields are generated by more than 1000 superconducting dipole magnets.
In total, four experiments are located along the LHC ring: ALICE, ATLAS, CMS and LHCb. ATLAS and CMS[4] are multi purpose particle physics experiments with their typical shell structure, whereas LHCb will concentrate on the physics of B mesons and CP-violation. In addition to the runs with protons the LHC can be operated with heavy ions. Then the centre of mass energy will be 2.76 GeV per atomic mass unit and the ALICE[5] detector will take data to find out more about heavy ion physics and quark-gluon plasma.
Since the work concluded in this thesis was performed within the ATLAS experiment, the ATLAS detector will be described in more detail in the next section. A layout of the LHC accelerator rings and its four experiments is shown in Fig. 1.1.

[4] **C**ompact **M**uon **S**olenoid
[5] **A** **L**arge **I**on **C**ollider **E**xperiment

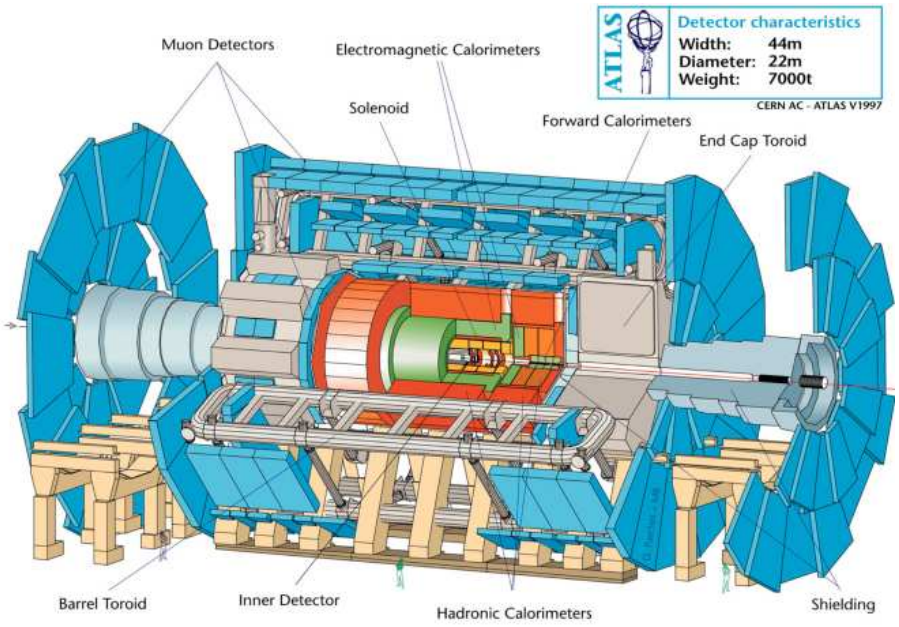

Figure 1.2: *The ATLAS experiment at the LHC comprises several sub detectors. The muon chambers, which are the subject of this thesis, are shown in blue. They can be used as stand alone detector.*

1.3 The ATLAS detector

The ATLAS[6] detector is located close to the CERN main building complex in Meyrin. With its dimensions of 22 m in diameter and a length of 44 m it is the largest experiment at LHC. Like most multi purpose particle physics experiment it is constructed from several functional layers, starting with the inner detector(s) closest to the interaction point (Fig. 1.2). Subsequent to the inner detectors the electromagnetic and hadronic calorimeters are installed. The muon spectrometer as the outermost layer can be used as a stand alone detector. All sub detectors of ATLAS are described briefly in the following.
Because of its cylindrical shape the ATLAS detector is separated into parts called *barrel* and *endcaps*. In the following the beam direction is referred to as *z-axis* and the direction perpendicular to it as r (cylindrical coordinates). The pseudorapidity η is defined as

$$\eta = -\ln\left[\tan\left(\frac{\theta}{2}\right)\right]$$

where θ is the angle between the beam axis and the scattered particle, leaving the interaction point.

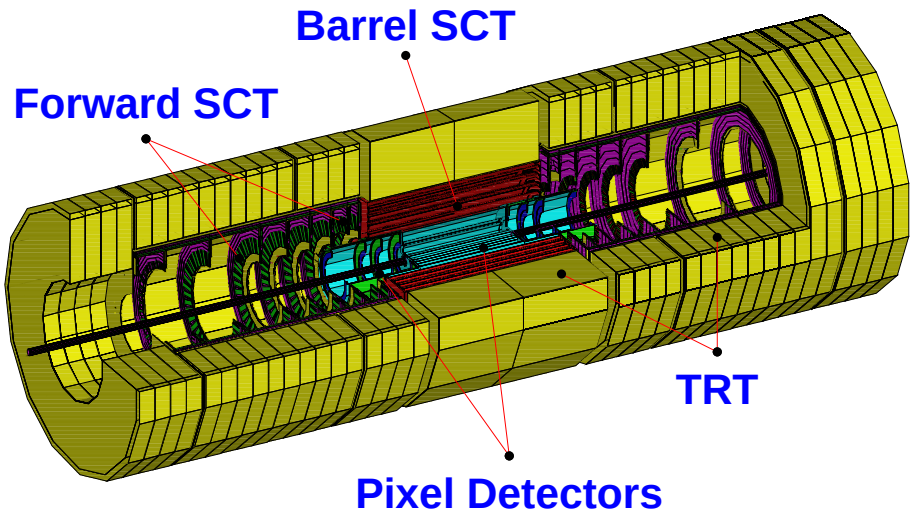

Figure 1.3: *Overview of the different techniques used in the inner detector of ATLAS.*

1.3.1 Inner Detector

In the inner detector three different technologies are used to find the tracks of particles traversing it. The silicon pixel detector is closest to the interaction point. With $1.4 \cdot 10^8$ channels a resolution of 60 μm along the z-axis and 12 μm in ϕ is reached. The silicon pixel detector covers a total area of 2.3 m^2 up to $\eta = \pm 2.5$. Its main purpose is to obtain a set of high-granularity, high-precision measurements as close as possible to the interaction point to find short-lived particles.
Subsequent to the pixel detector a **S**emi**C**onductor **T**racker (SCT) with a total area of 61 m^2 is deployed. Here, silicon microstrips organised in four layers rotated by a small angle (stereo angle) with respect to each other are used as detector material. Each detector consists of 768 readout strips with a width of 80 μm. With this setup a spatial resolution in Rϕ of 16 μm can be achieved. The z-coordinate can be determined with the stereo angle to an accuracy of 580 μm. The SCT was designed to provide four precision measurements along each track in the intermediate radial range, therefore contributing to the momentum measurement, impact parameter and vertex position.
Finally in the outermost layer a different approach is used for the inner detector, a **T**ransition **R**adiation **T**racker. The TRT is made of straw tubes with 4 mm diameter. The proximity to the the interaction point requires high rate capabilities and radiation hardness. Therefore this intrinsically radiation hard technique had been selected. Nevertheless, detailed ageing studies for the straw tubes have been carried out. In fact a beneficial cooperation has occurred in the context of the present dissertation (see 6.4.3). In total there are 420000 electronic channels, providing a drift time measurement and two independent thresholds. The drift time measurement allows a spatial resolution of 170 μm per straw, the thresholds allow to discriminate between tracking hits (passing the lower threshold) and transition-radiation hits (passing the higher threshold). Detailed information about all the inner detectors

[6] **A** **T**orroidal **L**HC **A**pparatu**S**

can be found in [2], an overview of the different detection techniques is shown in Fig. 1.3

1.3.2 Calorimetry

When the particles created in the pp-collisions move further outwards, they reach the electromagnetic calorimeter. Here, a liquid argon [4] sampling calorimeter with "accordion-shaped" electrodes is deployed covering the pseudorapidity interval $|\eta| < 3.2$. In the endcap region, at radii less than 2.2 m ($1.4 \leq |\eta| \leq 4.8$), the same technology is used for the hadronic calorimetry. For radial distances between 2.2 m and 4.23 m a less expensive tile-calorimeter [5] with iron-absorbers and plastic-scintillators comes into operation to measure the energy of hadrons.
In the electromagnetic calorimeter a fine segmentation of the electrodes allows to measure the shower shape very precisely. The energy resolution is $10\%/\sqrt{E} \oplus 0.5\%$ (E in GeV) for electrons. The energy of hadrons can be measured with an accuracy of $50\%/\sqrt{E} \oplus 3\%$ (E in GeV) in the hadronic calorimeter.

1.3.3 Magnetic fields

There are two magnetic field systems installed in ATLAS. One system utilizes a solenoid to generate a magnetic field of 2 T for the inner detectors to bend the tracks of the short-lived particles. The second system uses three air-core superconducting

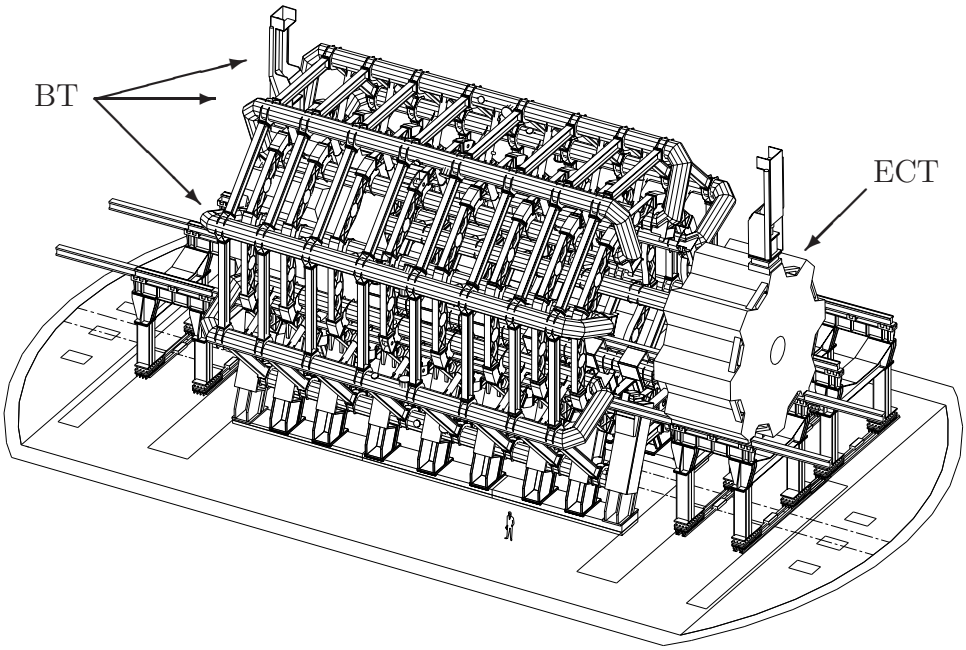

Figure 1.4: *Toroid coils used to produce the magnetic field in the ATLAS Muon spectrometer. In the barrel region the big toroid coils with the support structure for the MDTs can be seen. The right-hand end cap toroid is shown also, but moved away from its original position.*

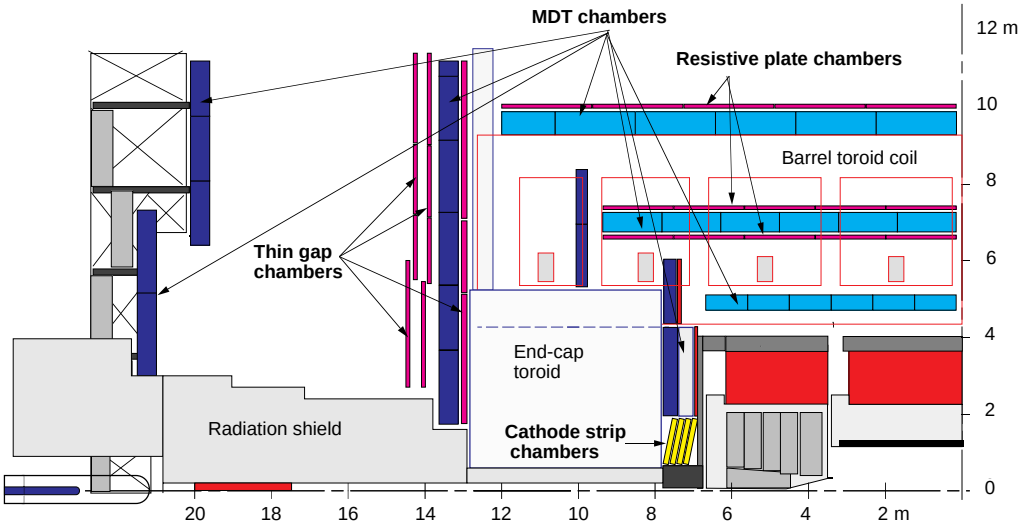

Figure 1.5: *Different detector types used for the ATLAS muon system. The MDTs and CSCs are used to detect traversing muons with a high spatial resolution. To allow this a fast trigger signal is needed. In the barrel region RPCs are used for this task, while in the endcap TGCs come into operation for both, MDTs and CSCs.*

toroids to produce a large magnetic field in the muon spectrometer with magnetic field strength of up to 4.1 T. The barrel toroid (BT) utilizes 8 toroid coils with a length of 25 m and an outer diameter of 20 m. The two endcap toroids (ECT) are 5 m in length and have an outer diameter of 10.7 m. They are rotated by 22.5° (see Fig. 1.4) with respect to the BT coils to provide for radial overlap and optimum bending power.

1.3.4 Muon system

The muon system plays the central role in the work described in this dissertation, hence it is explained in more detail. The muon system is the biggest sub detector of ATLAS in terms of the instrumented volume. In Fig. 1.5 the different techniques for the detection of muons can be seen. In the barrel region within the pseudorapidity range $|\eta| < 1$ Monitored Drift Tube (MDT) chambers are used for the precision measurement of muon tracks. They are employed together with Resistive Plate Chambers (RPCs) serving as trigger chambers. In the endcap section where $1 < |\eta| < 2$ Thin Gap Chambers (TGCs) are used for triggering. In the very forward direction $2 < \eta < 2.7$ where the particle flux is highest, Cathode Strip Chambers (CSCs) are used instead of MDTs.

Monitored Drift Tube Chambers

For the precision measurement of muon tracks with transverse momenta from 20 - 300 GeV a momentum resolution of

$$\frac{\Delta p_T}{p_T} \leq 2\%$$

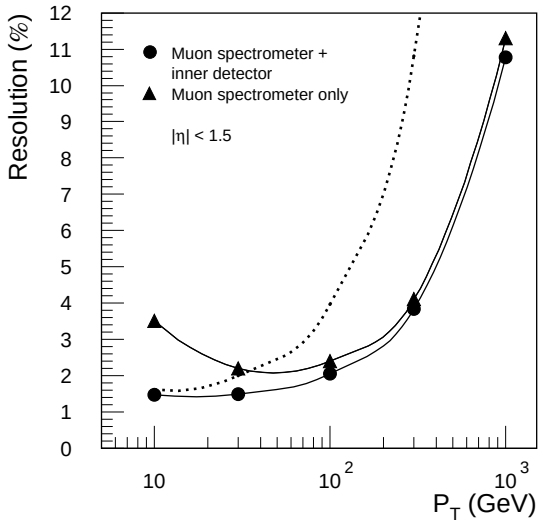

Figure 1.6: *Simulated resolution of the transverse muon momentum p_T averaged over $|\eta| < 1.5$, from [6]. When the information of the inner detectors is included the low p_T momentum resolution can be increased significantly (black circles).*

is desired [6], see also Fig. 1.6. In order to achieve this, MDTs are used over most of the solid angle. The primary detection elements are aluminium tubes of 30 mm diameter with a gold plated W/Re signal wire of 50 μm diameter in the centre. They are filled with a gas mixture of argon and CO_2 and are operated at an absolute pressure of 3 bar. This gas mixture gives a relatively long maximum drift time of 700 ns and thus a high occupancy in the drift tubes. Originally a gas mixture of Ar, CH_4 and N_2 with a maximum drift time of only 480 ns was foreseen. But the ATLAS Muon Collaboration had to switch to Ar:CO_2, since ageing effects were observed when operating the drift tubes with the gas mixture containing CH_4.
An MDT consists of many single drift tubes, glued in several layers on both sides of

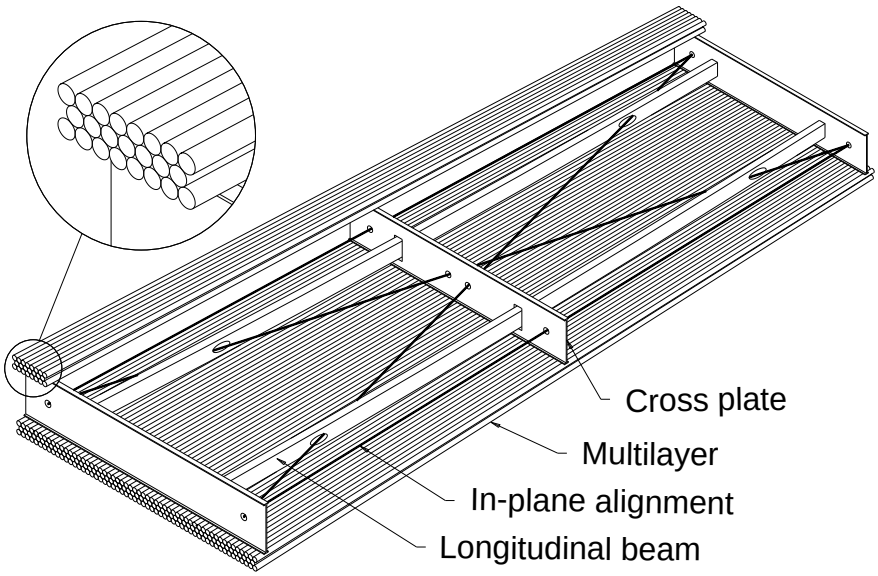

Figure 1.7: *Sketch of a rectangular MDT used in the barrel region of ATLAS. It is constructed from two multilayers of drift tubes. To monitor the shape of the chamber an in-plane alignment system is used together with temperature sensors.*

a support structure ("spacer"), see Fig. 1.7. The shape of the chamber is *monitored* by an internal optical alignment system in connection with temperature sensors.
On top of the outer drift tube layers trigger chambers are mounted. They provide a fast trigger signal, that marks the time of primary gas ionization in the drift tubes. From the measured drift time in the drift tubes the distance of the ionizing particle to the wire can be determined with an accuracy of 80 μm. Using the information of all drift tubes hit by the incident particle, a spatial resolution in the track measurement of 50 μm per chamber is achieved.
The chambers are further interconnected by a global alignment system and a reference alignment system in the endcaps (*alignment bars*). Additionally, the chambers are equipped with sensors for the magnetic field to determine local deviations of the relation between the drift time and the radial distance to the wire (r-t-relation).
MDT chambers are named with the glossary ABC, where $A = \{$**B**arrel,**E**ndcap$\}$, $B = \{$**I**nner,**M**iddle,**O**uter $\}$ and $C = \{$**S**mall,**L**arge$\}$. In the hollow feet of ATLAS, chambers with a special geometry and size were needed. They are named **BOF** and **BOG**.

Cathode strip chambers

In the very forward region CSCs instead of MDTs are used as precision chambers. CSCs are multi wire proportional chambers with segmented cathode strips for the signal readout. A resolution of < 60 μm is achieved by measuring the induced charge on the cathode strips and interpolating between them. The main advantages of the CSCs are small electron drift times, a good time resolution and a low neutron sensitivity. A measurement of the transverse coordinate is performed by a second cathode with orthogonal strips.

Trigger chambers

In the barrel region RPCs are used as trigger chambers. The working principle of RPCs is based on a narrow gas gap formed by two parallel plates composed of

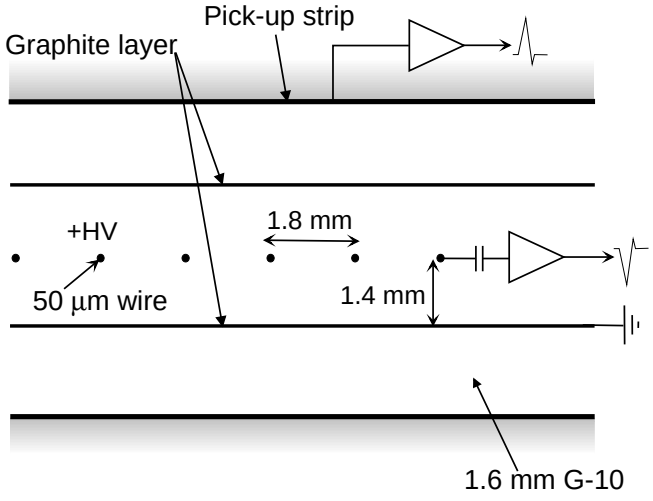

Figure 1.8: *Layout of a TGC cell (from [6]) used as trigger device in the endcaps of the ATLAS muon system.*

resistive Bakelite. This gap is filled with a gas mixture based on tetrafluorethane ($C_2H_2F_4$). Between the two plates an electrical field with a typical field strength of 4.5 kV/mm is used to amplify primary electrons in an avalanche. The signal readout is achieved by capacitive coupling of orthogonal metal strips on each side of the detector. There are two types of readout strips. The η-strips are parallel, the ϕ-strips orthogonal to the wires of the MDTs, therefore providing a second coordinate measurement required for the offline pattern recognition. The 354000 readout channels provide a time resolution of 1.5 ns. One trigger chamber is made of two of these rectangular detector layers.
In the endcap region, TGCs (Fig. 1.8) instead of RPCs are used for triggering. They are designed very much like a multi wire proportional chamber with the difference that the pitch between the anode wires is larger than the distance between anode and cathode. Filled with a highly quenching gas mixture of 55% CO_2 and 45% n-pentane a trigger efficiency of 99% for a gate of 25 ns is reached. Besides the signals on the anode wires parallel to the MDT wires, signals on perpendicular pick up strips are read out. These signal strips are separated from the graphite cathodes by a G-10 layer[7] and measure the second coordinate. More detailed information about the trigger chambers can be found in [6], chapters 8 (RPCs) and 9 (TGCs).

1.4 Physics at the LHC

Higgs One missing piece of the standard model is (are) the yet undiscovered Higgs boson(s). The elementary particles of the standard model are fundamentally massless, in contrast to what is measured in experiments. The Higgs mechanism provides a possibility to generate mass for all these particles. From theoretical considerations an upper limit for the higgs mass of $m_H < 1$ TeV is given. The stability of the electroweak vacuum and the perturbative nature of the standard model set further upper and lower bounds for the higgs mass, depending on the cutoff energy Λ up to which the standard model is valid [7]. If one expects the standard model to be valid up to the Planck mass $\Lambda \approx 10^{16}$ GeV, the higgs mass has to be in the range of $130 \leq m_H \leq 190$ GeV. The problems of the standard model already mentioned in 1.1.1 however suggest new physics (for instance *Super Symmetry*) already at energies of $\Lambda \approx 1$ TeV. In that case the possible range for the higgs boson mass spreads to $50 \leq m_H \leq 800$ GeV.

[7] G-10: Glass reinforced epoxy

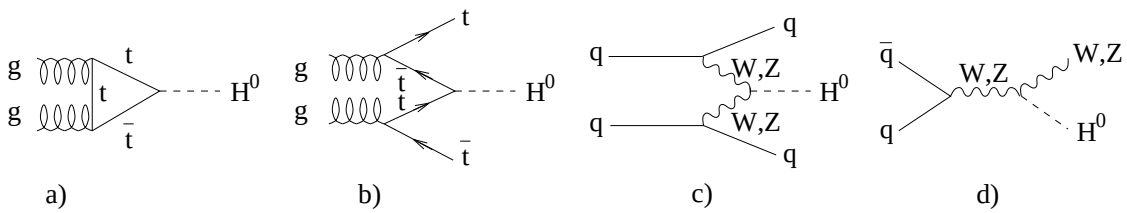

Figure 1.9: *Higgs production processes in proton-proton collisions. At LHC the gluon fusion (a) and W/Z-Fusion (c) will be dominant.*

Previous particle physics experiments set further restrictions: From the LEP experiments a higgs mass below 114.1 GeV is excluded at 95% confidence level. From high precision measurements in the electroweak sector, sensitive to the higgs mass via loop corrections, the current best fit predicts $m_H = 129^{+74}_{-49}$ GeV [8]. In [9] a higgs mass $m_H < 144$ GeV with 95% confidence level is suggested. The ATLAS detector can discover the higgs particle over the whole energy range up to 1 TeV.
In a collider, the higgs boson is mainly created by the processes shown in Fig. 1.9. At LHC in particular the gluon- and W-fusion process are dominant. After the production the higgs boson will decay to the heaviest particles possible. The branching ratio is shown in Fig. 1.10 (left). The most promising subsequent decay chains are:

- $H \rightarrow \gamma\gamma$: This decay is only important for a rather low higgs mass. Because of a large irreducible background an excellent angular and energy resolution in the ECAL is needed to distinguish the higgs peak from noise.

- $H \rightarrow bb$: The dominant decay mode if the higgs mass is less than twice the $W^{\pm}$ mass. Since the direct decay $H \rightarrow bb$ can not be separated from the huge QCD two-jet background, this mode can only be observed if the higgs is produced in association with a $t\bar{t}$ pair or a W. These particles are then used to distinguish signal from background.

- $H \rightarrow ZZ^{(*)} \rightarrow 4l$: The gold-plated channel for $130 \leq m_H \leq 800$ GeV (see also Fig. 1.10 (right)). With four leptons (e,μ) in the final state this decay mode has a clear signature. The design of the ATLAS muon spectrometer was mostly driven by this decay channel.

After 3 years of data taking at low luminosity (10^{33} cm^{-2}s^{-1} = 30fb^{-1}) the standard model higgs can be observed at ATLAS. Moreover a discovery with a statistical

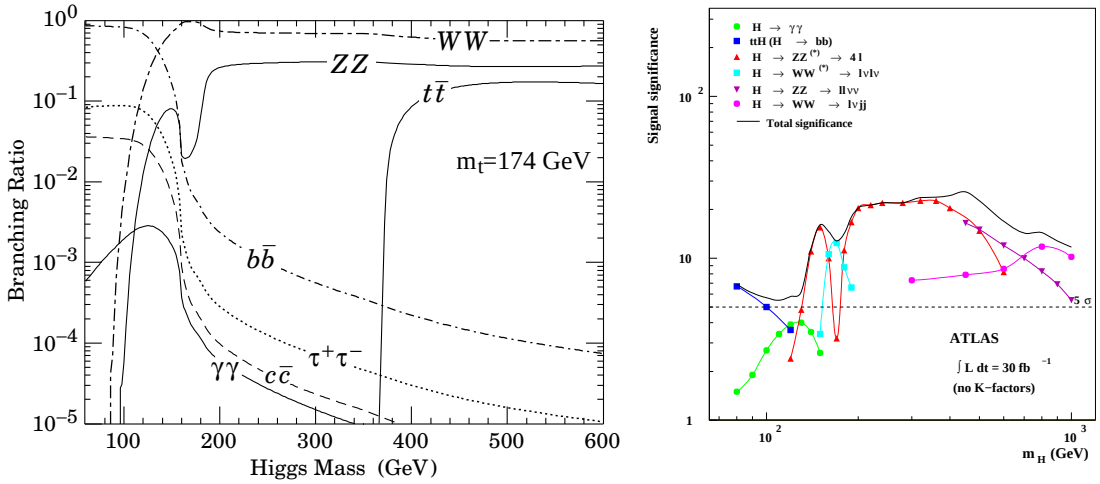

Figure 1.10: **Left:** *Branching ratio of the standard model higgs for different higgs masses [6].* **Right:** *Discovery potential of ATLAS after* $\int Ldt = 30fb^{-1}$ *for the different decay modes [7].*

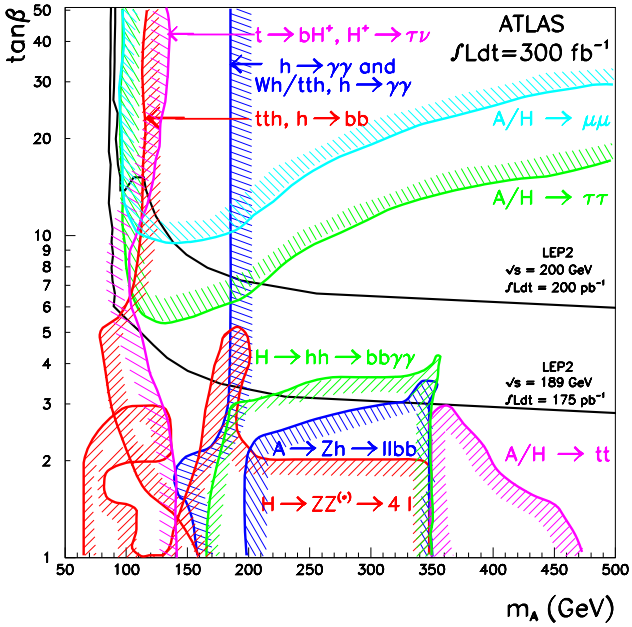

Figure 1.11: *Discovery potential of ATLAS for MSSM higgs particles after running 3 years with high luminosity $L = 10^{34} cm^{-2} s^{-1}$ [7]. Analyses performed with the LEP experiments already excluded quite a lot of the parameter space.*

significance of more than 5σ is possible within the first few years of data taking over the whole mass range up to 1 TeV (see Fig. 1.10 (right)).

Super Symmetry As the most popular extension of the standard model, SUSY predicts the existence of at least five higgs particles (h, H, A, $H^{\pm}$). The higgs masses and couplings are expressed in terms of two variables in the MSSM. The usual choice is a mass m_A and the tangent of the angle β. The $\tan\beta$ is the ratio of the vacuum expectation values of the two higgs-doublets. Depending on the values of m_A and $\tan\beta$, SUSY can be found with ATLAS or not. This is often shown in exclusion plots as in Fig. 1.11. Besides the SUSY higgs particles, ATLAS will also look for other super symmetric particles. When these particles are produced they will decay similarly to the standard model particles. In the end of all decay chains the lightest super symmetric particle (LSP) is left over. The LSP is either stable or decays into standard model particles depending on whether R parity[8] is conserved or not. If R parity is conserved the LSP is a promising candidate for dark matter.

QCD, α_S, top physics

LHC will run at centre of mass energies never reached before by any particle accelerator. Hence QCD will be tested and measured at a new energy scale. The quark- and gluon densities of the proton as well as the value of the strong coupling constant α_S will be measured.
Currently the *Tevatron* produces about $6 \cdot 10^4$ top quarks per year and determines the mass and width of this particle with remarkable accuracy thanks to advanced analysis methods. At LHC, even at low luminosity, one $t\bar{t}$ pair per second will be produced, so that the LHC is often called a *top-factory*. The huge number of

[8] R parity: new quantum number introduced by *Super Symmetry*, $R_{SUSY} = -1$, $R_{SM} = 1$.

top events transforms the determination of the top quark parameters into a simple statistical exercise [10].

1.5 The subject of this thesis

Big efforts were made to build an extremely precise muon system for ATLAS. Unfortunately this precision can be lost quickly if ageing effects occur. For this reason, this thesis investigates how to minimize such negative effects or even better how to avoid them if possible. The results of these studies are presented in this dissertation. As a starting point, the working principle of the ATLAS monitored drift tubes is outlined in chapter 2 together with the problems arising if ageing effects play a role. In chapter 3, previous ageing experiments in Freiburg and at CERN are introduced. Their results made further ageing studies necessary. The experimental setup of these new ageing tests is described in detail in chapter 4. To achieve a deeper understanding of the whole setup, a Monte Carlo simulation was developed. Chapter 5 shows the key features and predictions of this tool. In chapter 6 the results of the new ageing experiment are shown and discussed. As a result of the measurements a gas filter was required to allow a safe operation of the MDTs in the ATLAS muon spectrometer. The design features of the filter and results of intensive tests are presented in chapter 7. Finally a summary is given in chapter 8.

Chapter 2

Drift tubes

Being the main detection element of the ATLAS MDT muon chambers, drift tubes are introduced in this chapter. At first the requirements on drift tubes for the ATLAS muon chambers are outlined briefly. In section 2.2 the different steps of signal generation in a drift tube are explained. Section 2.3 discusses the background radiation expected in ATLAS. Finally a model to explain the general ageing mechanism in wire chambers is given in section 2.4.

2.1 Layout of the ATLAS muonsystem drift tubes

The parts that make up an ATLAS muonsystem drift tube can be seen in Fig. 2.1. They are assembled at the production sites of the institutes participating in the ATLAS muon collaboration. An aluminium tube with an outer diameter of 29.97 mm and a wall thickness of 400 μm is used as the cathode. For the anode, a gold-plated W/Re signal wire with 50 μm diameter is put into the middle of the aluminium tube. The accuracy of drift time measurements determines the spatial

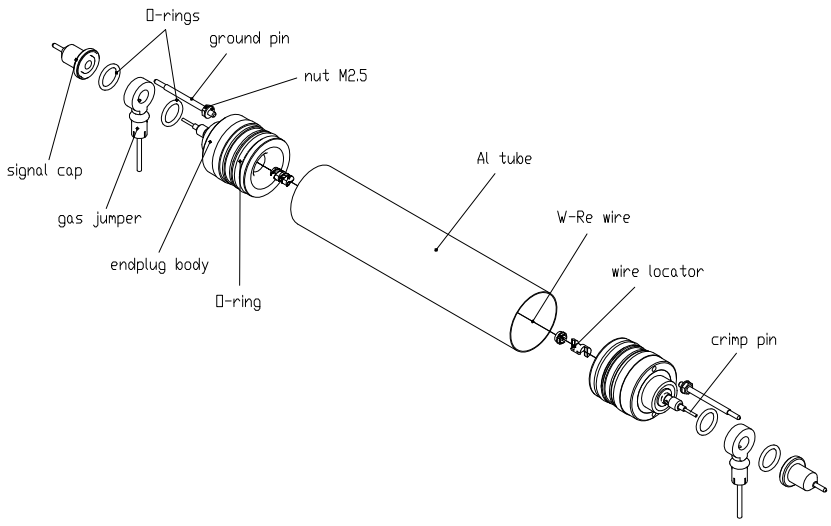

Figure 2.1: *Exploded view of a single ATLAS muonsystem drift tube taken from [11].*

resolution of the tube, thus it is crucial to place the signal wire as good as possible in the tube centre. This is achieved with the help of an end plug with a precisely machined outer aluminium ring. When the individual drift tubes are glued together, the aluminium ring serves as a reference to adjust the relative wire positions with an accuracy of 20 μm. Apart from the aluminium ring the end plug body is composed of glass fibre reinforced Noryl and a brass core. The body incorporates a so called *wire locator* to define the wire position with respect to the aluminium ring. Furthermore the end plug has to accomplish the following tasks:

- high voltage insulation between the signal wire (anode) and the aluminium tube wall (cathode)
- connection to the gas distribution
- connection to the front-end electronics for signal readout
- connection to the high voltage supply

2.2 Working principle

The aluminium drift tubes are operated with a gas mixture of Ar:CO_2 at a ratio 93 : 7 at an absolute pressure of 3 bar. When an ionizing particle traverses the gas in the tube it creates pairs of electrons and ions. The electrical field, generated by the high voltage between signal wire and tube wall pulls the separated charges further apart. The electrons are accelerated towards the wire, the ions to the tube wall. The electrical field has a radial symmetry and increases rapidly in the vicinity of the wire. At distance r the field strength is given by

$$E(r) = \frac{U}{ln(r_t/r_w)} \cdot \frac{1}{r} \tag{2.1}$$

with the anode voltage U, the tube radius r_t and the wire radius r_w.

2.2.1 Primary ionization

The primary ionization in the drift tubes can either be caused directly by charged particles, or indirectly in case of neutral particles, such as photons and neutrons. The underlying effects for ionization are different for the two cases:

Charged particles: The Bethe-Bloch formula [20] applies to all charged particles. With its help the average energy loss per unit path length can be calculated:

$$\frac{dE}{dx} = -4\pi N_A r_e^2 m_e c^2 \frac{Z}{A}\frac{1}{\beta^2} z^2 \rho \Big(\ln \frac{2m_e c^2 \beta^2 \gamma^2}{I} - \beta^2 \Big) \tag{2.2}$$

where N_A is Avogadro's number, m_e the electron rest mass, r_e the classical electron radius and c the speed of light. For the ionized medium the following quantities

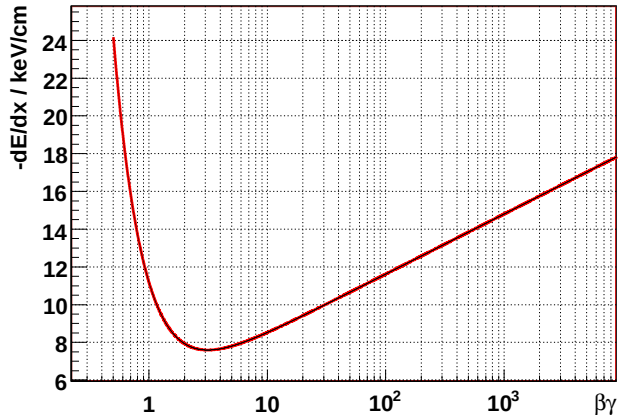

Figure 2.2: *Qualitative progression of the Bethe-Bloch formula Eq. 2.2. At $\beta\gamma \approx 3\ldots4$ a minimum is obtained. The curve shown here was calculated for argon at 3 bar and a charge of the incident particle of $Q = \pm 1$.*

are of importance: the density ρ, the ionization potential I, the molecular weight A and the charge Z. The properties of the incident particle enter the equation with the speed (expressed in terms of β and γ) and the charge Z. In Fig. 2.2 the qualitative progression of the Bethe-Bloch formula with its characteristic minimum at $\beta\gamma = 3\ldots4$ is shown. Eq. 2.2 describes only the average energy loss per unit path length and is therefore well suited for thick absorbers. In thin absorbers (like the gas in the drift tubes) the energy loss fluctuates according to a landau distribution. In its original form the landau distribution is defined as a complex integral, but it can be approximated by [12]:

$$L(\lambda) = \frac{1}{\sqrt{2\pi}} \cdot exp\Big(-0.5 \cdot (\lambda + e^{-\lambda})\Big) \tag{2.3}$$

where

$$\lambda = \frac{\Delta E - \Delta E^{mp}}{\xi} \qquad \text{and} \qquad \xi = 2\pi N_A r_e^2 m_e c^2 \frac{Z}{A} z^2 \frac{1}{\beta^2} \rho x \tag{2.4}$$

ΔE is the actual energy loss in a detector of thickness x, while ΔE^{mp} is the most probable value of the energy loss, calculated with Eq.2.2. The parameter ξ characterizes the width of the Landau distribution.
For a minimum ionizing cosmic muon with $E \approx 350$ MeV the average energy loss in 3 cm Ar at 3 bar can be calculated to $\Delta E^W \approx 22.6$ keV and the width to $\xi \approx 1.15 keV$. However the most probable energy loss in 3 cm argon at 3 bar is less than 22.6 keV, so that the Landau distribution in Fig. 2.3 is obtained. With an average energy for a single ionisation

$$\bar{E}_{ion} = 26eV \tag{2.5}$$

this corresponds to about 870 primary electrons. These electrons are created along the whole track in several clusters with different cluster sizes. The cluster size distribution in Ar and CO_2 was measured in [13] and is shown in Fig.2.4 for Ar:CO_2 93 : 7. Clusters with sizes of $n > 50$ are not unlikely for a muon track with many primary ionizations. If in addition the muon traverses the drift tube close to the wire, where the range of drift times for the clusters spreads from zero to the maximum

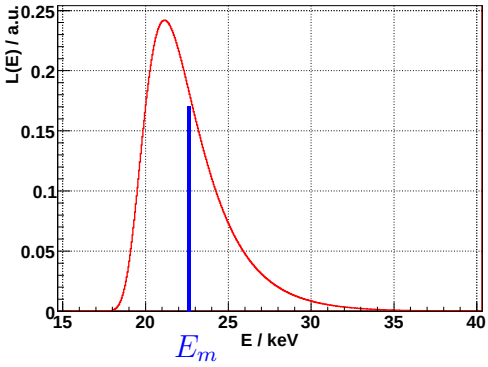

Figure 2.3: *Probability distribution for the actual energy loss of a minimum ionizing particle in an ATLAS muonsystem drift tube. The mean value E_m is different from the most probable energy loss.*

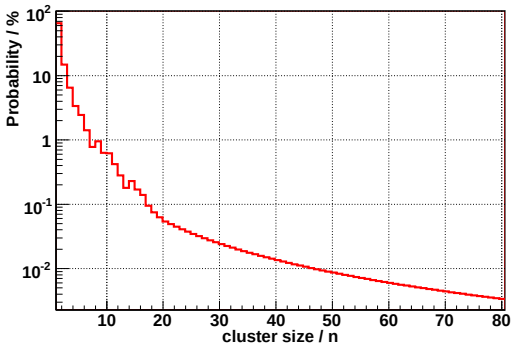

Figure 2.4: *Cluster size distribution in argon, calculated from [13]. The probability for a cluster size of $n > 50$ is $p(n > 50) \approx 0.32\%$.*

drift time t_{max}, the arrival of individual clusters on the wire can be resolved, see Fig. 2.5 (left).

Neutrons: For neutrons as uncharged particles, Eq.2.2 does not apply. At low kinetic energies (thermal) neutrons mainly activate matter due to capture by nuclei of the surrounding matter. The subsequent β^- decay of the nucleus allows detection of the neutron. At higher kinetic energies, neutrons can interact with matter via elastic or inelastic scattering. In the case of inelastic scattering the recoil nucleus is left in an excited state. The subsequent de-excitation results in the emission of a photon. The recoil nucleus itself slows down in collisions with other atoms and via ionization. Since the nucleus has only a low kinetic energy the number of liberated electrons per unit path length is much higher as for minimum ionizing muons or photons. Thus neutrons contribute to the expected background radiation at ATLAS.

Photons

Photons interact with matter via three different processes: For low photon energies the photoelectric effect is dominant. Hereby the photon ionizes an atom by liberating an electron, predominantly from the innermost shell. The photon is completely absorbed in this process.
If the photon energy exceeds about 100 keV (in gases only $20-30$ keV) the dominant absorption process is Compton scattering. Then only part of the photon energy E_γ is transferred to a quasi-free valence electron in the scattering process. The cross section for the energy of the recoil electrons E_e follows the Klein-Nishina-formula [14]:

$$\frac{d\sigma}{dE_e} = \frac{\pi r_e^2}{m_e c^2 \gamma^2}\Big[2 + \frac{s^2}{\gamma^2(1-s^2)} + \frac{s}{1-s}\Big(s - \frac{2}{\gamma}\Big)\Big] \tag{2.6}$$

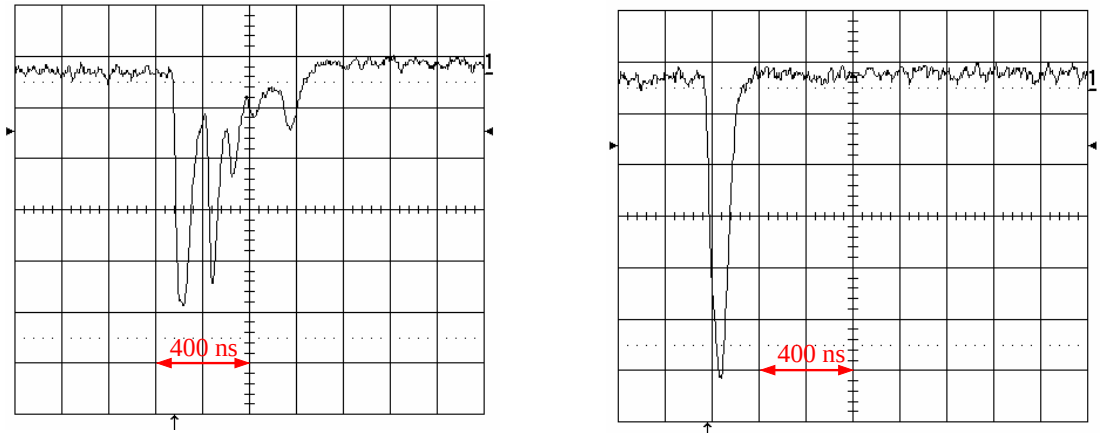

Figure 2.5: *Signals in a MDT, generated by a muon (***left***) and by a photon with* $E \approx 22$ *keV (***right***) from a* ^{109}*Cd source. The muon signal shows several peaks from different clusters along the track. The photon signal shows only a single peak due to the localized primary ionization. The pictures were taken from [25].*

where $s := E_e/E_\gamma$ is the fraction of the photon energy transferred to the electron and $\gamma := E_\gamma/m_e c^2$. The maximum value for E_e is given by the Compton edge at:

$$E_e^{max} = E_\gamma \cdot \frac{2\gamma}{1+2\gamma} \tag{2.7}$$

When the photon energy exceeds twice the rest mass of an electron ($E_\gamma > 1.022$ MeV), electron positron pairs can be produced in the field of a nucleus.
In all three processes free electrons are produced and subsequently detected. For the liberated electrons one can calculate a mean path length (Eq. 2.2), depending on their energy. In a drift tube at operating conditions the range of electrons with an energy of $E = 16$ keV is only about 2 mm. In the vicinity of their track the number of

$$N = \frac{E}{\bar{E}_{ion}} = 615 \tag{2.8}$$

primary ionizations occur. In contrast to the minimum ionizing muon, the clusters are now distributed over the small range of 2 mm. Hence the measured signals show only a single peak, as can be seen in Fig. 2.5 (right).
More details about the interaction of photons with matter, in particular with respect to drift tubes, can be found in chapter 5.

2.2.2 Electron drift and gas amplification

The electrons, liberated in the processes described above, gain kinetic energy from the electric field in the drift tube (Eq. 2.1). Far away from the wire the electrons scatter from atoms before having enough kinetic energy to ionize them. Consequently they slow down and an average drift velocity can be observed on a macroscopic scale. This allows to compute a relation between the distance r to the wire

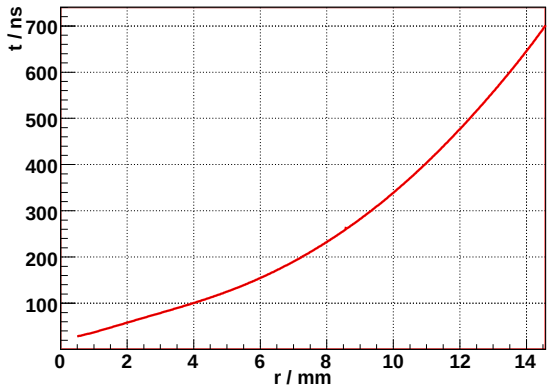

Figure 2.6: *r(t)-relation between the radial distance from the wire and the drift time of electrons. The curve shown here was calculated with a polynomial function of 9th order with parameters taken from the MDT digitization package.*

and the drift time t, see Fig. 2.6. The maximum drift time of $t_{max} \approx 700$ ns is reached for electrons starting from the the tube wall. However, velocity and drift time of the electrons depend strongly on the composition of the gas. By changing the ratio of Ar:CO_2 the drift time changes also. The amount of water in the operating gas, that is needed at a low level of ≈ 500 ppm, also has an impact on the drift velocity. The dependence of the maximum drift time on the argon and water content of the gas is given in Fig. 2.7.
Close to the wire the drifting electrons gain enough kinetic energy between two successive collisions to further ionize the argon atoms. In an avalanche more and more free charges are created and separated. In the end the number of electrons has dramatically increased. This process is known as gas amplification. The multiplication factor or gas gain G is given by the ratio of electrons on the wire divided by the number of primarily created electrons N. The first Townsend-coefficient α gives the probability for secondary ionization per unit path length. With this coefficient α,

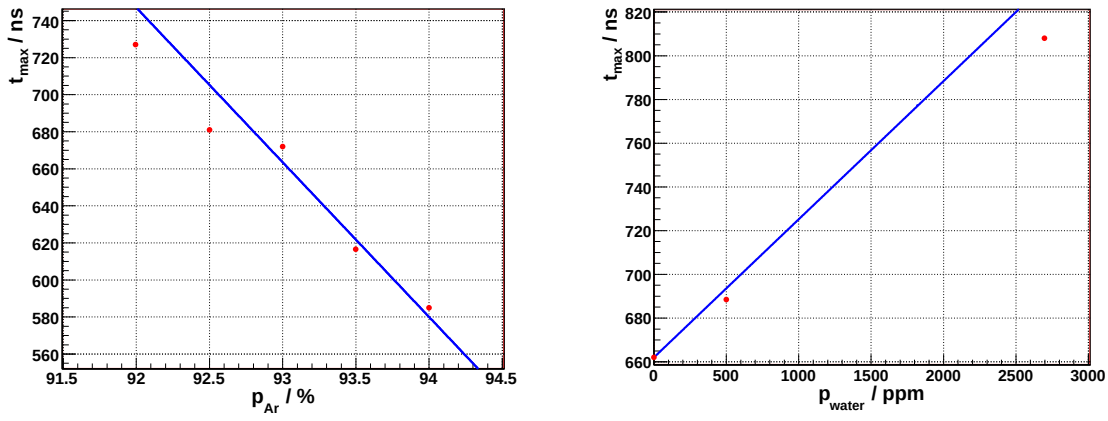

Figure 2.7: *Maximum drift time as a function of the argon (***left***) and water content (***right***) of the gas mixture. The red data points correspond to measurements conducted at the Gamma Irradiation Facility (GIF) [15], while the blue line is retrieved from a GARFIELD[16] simulation.*

the number of newly created electrons dN along dx can be calculated to:

$$dN = \alpha \cdot N \cdot dx \tag{2.9}$$

α depends on the gas mixture, the electrical field and the gas density. By integrating Eq.2.9 from the point where gas amplification sets in to the surface of the wire and assuming a linear dependence of α on the electric field, one finds the Diethorn formula:

$$G = \Big[\frac{U}{r_w \cdot ln(r_t/r_w) \cdot E_{min}(\rho_0) \cdot (\rho/\rho_0)}\Big]^{\frac{U \cdot ln2}{ln(r_t/r_w)\Delta V}} \tag{2.10}$$

E_{min} is the field strength needed for gas amplification and ΔV the potential difference needed to ionize the gas. r_w and r_t are the radii of the signal wire and the drift tube respectively. A detailed derivation of the Diethorn formula can be found in [17]. The values of the parameters E_{min} and ΔV were measured for Ar:CO_2 = 93 : 7 in [18] to:

$$\Delta V = 34V \qquad E_{min} = 24kV/cm \tag{2.11}$$

at ρ_0 corresponding to 1 bar and $T = 25°C$. The accuracy of these measurements is estimated to $\pm 10\%$. In Fig. 2.8 (left) the gas gain is plotted for two different values of the parameter E_{min}, that differ by $\approx 2\%$. The difference causes a dramatic change in G, that is due to the exponential multiplication of electrons in the avalanche. With regard to the uncertainties of $\pm 10\%$ for the Diethorn parameters in 2.11 there are limitations in setting an absolute value of G with Eq. 2.10. Nevertheless for a given gas mixture the Diethorn formula has proven to be a good tool to extrapolate the progression of the gas gain as a function of voltage.
When measuring the charge of an avalanche induced by a single primary electron several times, one would not always measure $G \cdot e^-$, but rather a fluctuation of $G \cdot e^-$

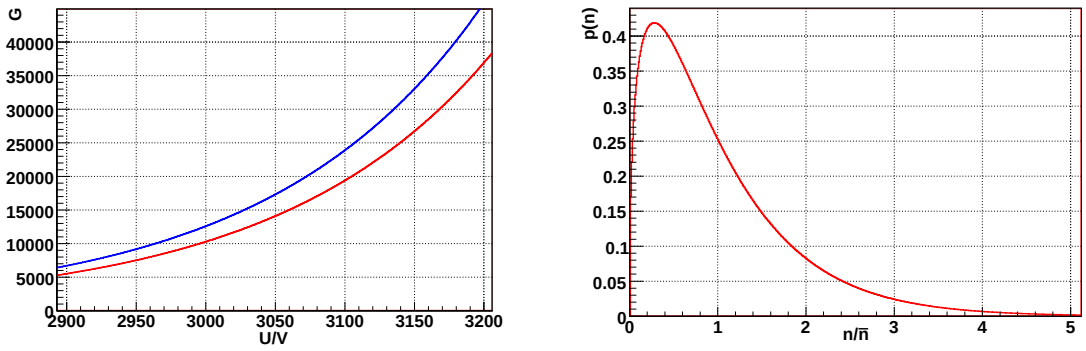

Figure 2.8: **Left:** *Gas gain as a function of the voltage, calculated with the Diethorn formula for $E_{min} = 24kV/cm$ (red) and $E_{min} = 23.5kV/cm$ (blue). The absolute difference in G is huge, nevertheless the progression of G is similar.* **Right:** *Polya distribution with parameter $\theta = 0.4$. The x-axis has to be identified with the gas gain ($1 \equiv 2 \cdot 10^4$)*

that follows a Polya distribution:

$$P(n) \propto \left(\frac{n}{\bar{n}}\right)^{\theta} \cdot e^{-(\theta+1)(\frac{n}{\bar{n}})}$$

where n has to be identified with G and $\bar{n}$ with $\bar{G}$. The parameter θ describes the development of an avalanche at different stages. With a value of $\theta = 0.4$ measured data is described reasonably [20]. The shape of the Polya distribution is shown in Fig. 2.8 (right).

2.2.3 Ion drift and signal generation

When the electrons are accelerated towards the wire by the electric field, positively charged ions are left behind, which in turn move towards the tube wall with a velocity:

$$v_{ion} = \mu_{ion} \cdot \frac{E}{p} \tag{2.12}$$

where μ_{ion} is the ion mobility and p the gas pressure. This equation is valid up to a field strength of $E \approx 45$ kV/cm at 3 bar for Ar^+ ions, see Fig. 2.9. In comparison to the electrons the velocity of the ions is rather low, so that they reach the tube wall only after roughly 4 ms. With the assumption that the potential U is kept constant, Ramo's theorem [20] allows to calculate the current of moving charges in an electric field:

$$I(t) = \frac{P(t)}{U} = \frac{F(t) \cdot v(t)}{U} = -q \cdot \frac{\vec{E}(r(t))\vec{v}(r(t))}{U} \tag{2.13}$$

Since almost all ions are produced very close to the wire, their drift starts in a region with a high electrical field strength and thus their impact on the current is bigger than the current induced by the electrons. For a cylindrical drift tube with an electric field as in Eq.2.1 and ions moving as specified in Eq.2.12 one finds:

$$I(t) = \frac{q}{2 \cdot \ln(r_w/r_t)} \cdot \frac{1}{t + t_0} \qquad \text{with} \qquad t_0 = \frac{r_w^2}{2\mu_{ion} \cdot U} \cdot \ln(r_w/r_t) \tag{2.14}$$

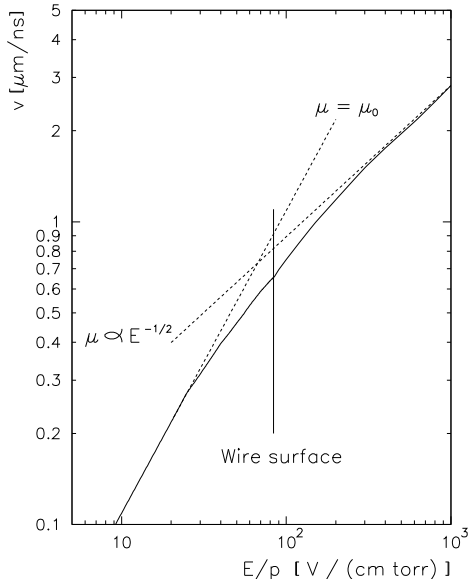

Figure 2.9: *Ion velocity in Argon from [19]. Up to a field strength of $E/p \approx 20$ V/(cm · Torr) (equivalent to $E \approx 45$ kV/cm at 3 bar) a linear relation between v and E is observed. At higher field strength the dependence of v on E/p is $\propto (E/p)^{-1/2}$. The electric field strength at the wire surface is indicated by the vertical line.*

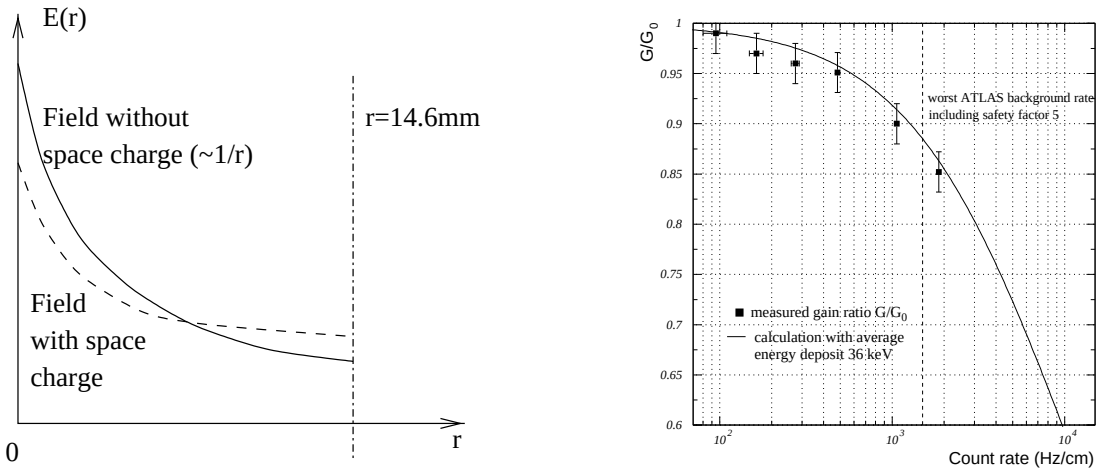

Figure 2.10: **Left:** *Reduction of the electric field due to the presence of space charges. The resulting drop in gas gain is shown on the* **right** *picture. The data points are measurements at* $G = 2 \cdot 10^4$*, the solid line refers to a calculation with an analytical model for space charges. Both diagrams were taken from [18].*

for the induced current of a single ion with charge q.

Space charge effects When the tubes are operated with a high gas gain or irradiated at a high rate, many separated charges are moving in the tube at the same time. The ions drifting slowly to the tube wall create a space charge that changes the electric field (Fig. 2.10, left) for subsequently drifting electrons and ions, thus changing also the gas gain (Fig. 2.10, right). For the ATLAS muon spectrometer drift tubes, a maximum background counting rate of 1500 Hz/cm (section 2.3) is expected corresponding to a reduction in gas gain of about 12%.

2.3 Irradiation expected at ATLAS

When the protons of the LHC beams collide in ATLAS with a bunch crossing time of 25 ns, many scattering processes will happen. Thereby the processes of interest involving new physics (section 1.4) are only a minority. The majority of signals arises from softly scattered particles in the calorimeters, the magnet coils, in the radiation shield around the beam pipe and other massive parts of the detector. After several scattering processes mostly neutrons and photons are left. They are uncorrelated to the primary event and penetrate the muon system as a constant flux of background radiation.
In Fig. 2.11 the expected fluxes for photons and neutrons in the ATLAS detector are shown. In the small wheel, closest to the point where CSCs are employed, the particle flux is highest. To determine the background counting rate the photon flux of $f_\gamma \approx 8$ kHz/cm^2 and the neutron flux $f_n \approx 2.5$ kHz/cm^2 have to be multiplied by the photon and neutron detection efficiency. They are averaged over the energy spectrum for each particle species. When protons, pions and other charged particles

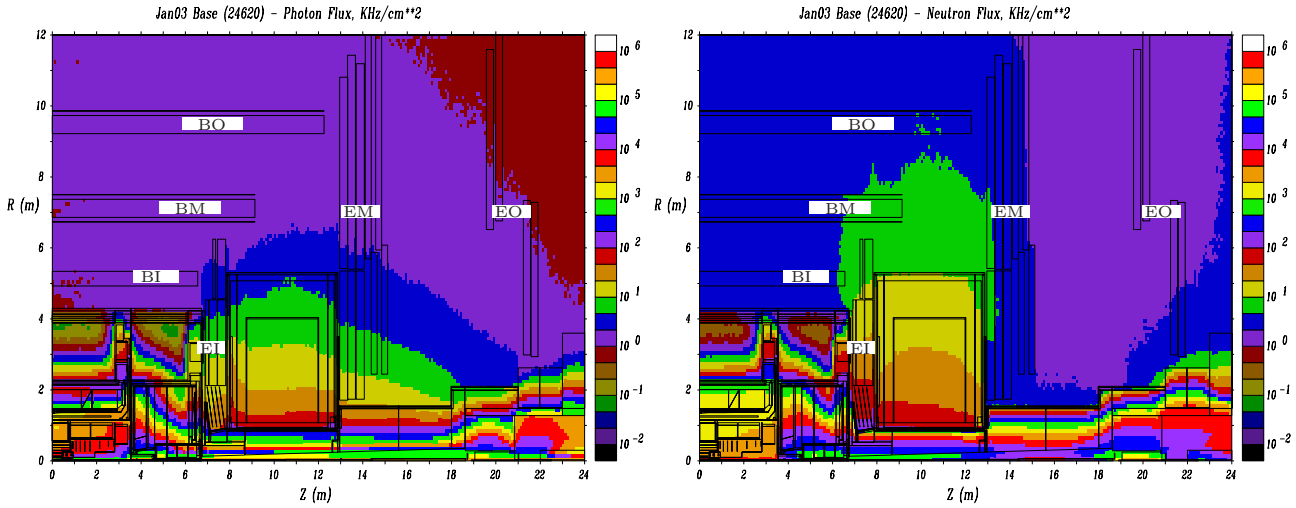

Figure 2.11: *Latest results of GCALOR simulations for the expected fluxes of photons (***left***) and neutrons (***right***) in ATLAS, calculated for the design luminosity of* 10^{34} $cm^{-2}s^{-1}$*, taken from [21]. The highest fluxes for the MDTs occur in the inner region of the small wheel (labelled with "EI")*

are included, one arrives at the single plane counting rate:

$$R = f_n \cdot \epsilon_n + f_\gamma \cdot \epsilon_\gamma + f_p + f_\pi + f_\mu + f_e \cdot \epsilon_e \tag{2.15}$$

with the efficiencies $\epsilon_n \approx 3 \cdot 10^{-4}$ for neutrons and $\epsilon_\gamma \approx 5 \cdot 10^{-3}$ for photons. The factor ϵ_e avoids double counting of electrons. The many details were worked out by the ATLAS background radiation task force and are reported in [21]. For the different regions of the muon spectrometer the counting rates shown in Fig. 2.12 are expected. The maximum of 103 Hz/cm^2 is obtained in the MDTs of the small wheel closest to the beam pipe. With a tube diameter of $d \approx 3$ cm a background counting rate of

$$R = 3cm \cdot \frac{103Hz}{cm^2} = 309\frac{Hz}{cm} \tag{2.16}$$

must be expected. The combination of detection efficiencies and energy spectrum results in an average pulse charge of 3.9 pC for photons at the nominal voltage of 3080 V. The ATLAS running time of 10 years can be approximated by 10^8 s, taking into account shutdown periods for repairs, etc. By treating all hits as photons events one ends up with

$$Q = 309\frac{Hz}{cm} \cdot 3.9 \cdot 10^{-12}C \cdot 10^8 s = 121\frac{mC}{cm} \tag{2.17}$$

as estimation for the integrated charge on the wire. With a safety factor of 5, accounting for uncertainties in the simulation and design changes of the radiation shielding[1], the drift tubes must sustain an integrated charge of 600 mC/cm.

[1]The layout of the shielding was not fixed when a safety factor of 5 was introduced.

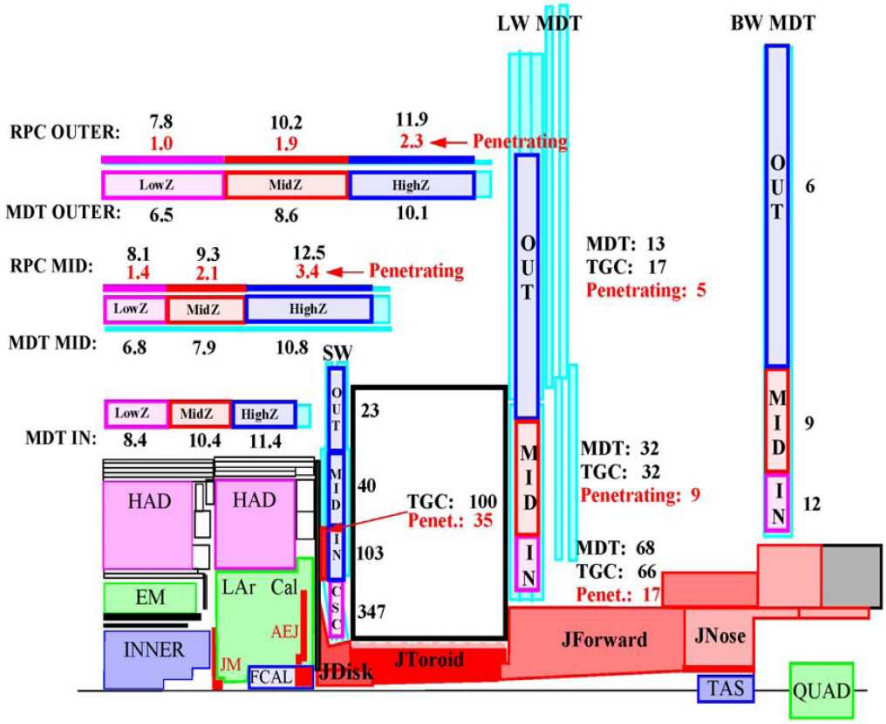

Figure 2.12: *Expected single plane counting rates in Hz/cm^2 due to background events in ATLAS. The highest counting rate is predicted in the inner MDTs of the small wheel.*

2.4 Ageing processes

In wire chambers operated with gases containing hydro carbons, like CH_4, ageing effects are frequently observed. Very often, the observed degradation of the chambers was caused by deposits on the anode wire(s). The origin of these deposits is explained by a plasma chemistry model in section 2.4.1. The consequences for the ATLAS muon spectrometer are briefly outlined in section 2.4.2.

2.4.1 A plasma chemistry model

In a small range around the anode wire the high electrical field strength creates a plasma with electron energies of a few eV. Electrons with energies at the upper end of the energy spectrum cause further ionization and hence gas amplification. But there is also a broad distribution of electrons with less energy; they can break bonds of molecules and thereby create fragments and radicals. Typical dissociation energies of molecular bonds are shown in Tab. 2.1. For the fragmentation

$$C_2H_6 \rightarrow C_2H_4 + H_2$$

an electron energy of only 1.4 eV is needed. In the plasma ionized states and neutral radicals of hydro carbons are also produced. These neutral molecules do not participate in a chemical bond, unless they find another molecule with only one valence electron. The reactions between these radicals can finally result in the

Bond or compound	Dissociation energy
H-C_2H_5	4.3 eV
H-CH_3	4.6 eV
H-CH_2	4.8 eV
H-C	3.5 eV
H_2	4.5 eV
H-OH	5.2 eV
O=CO	5.5 eV
CO	11.2 eV
Si-O	8.3 eV
Si-C	4.7 eV

Table 2.1: *Dissociation energies for various bonds from [22] and [23]. The silicon bond with oxygen is very stable and can be the starting point for silica polymerization. The strength of the CO bond is presumably the reason for the good ageing behaviour of the gas mixture chosen for the ATLAS MDT muon system.*

formation of polymers. For example in the presence of ethylene C_2H_4 the following reaction can happen:

$$CH_3 \cdot + C_2H_4 \rightarrow C_3H_7 \cdot$$

and further

$$C_3H_7 \cdot + C_2H_4 \rightarrow C_5H_{11} \cdot$$

In this manner, longer and longer chains of polymers are formed. At some point they condensate from the gas phase and deposit onto the electrodes.

Silicone ageing In materials science the plasma polymerization of silicones is a commonly used technique for surface treatment [23], particularly to improve surfaces that are in contact with harsh environments. In the plasma, surrounding the anode wire of the drift tubes, silicon compounds (if present) can be fragmented in the same way. Due to the high dissociation energy of the Si-O bond this structure often remains and serves as starting point for the silica polymer to which other molecules are then attached.

2.4.2 Consequences for the ATLAS Muonspectrometer

When polymers deposit on the wire they change the effective wire diameter and the dielectrical constant. Both effects change the electrical field strength close to the wire and hence the gas amplification and drift time of electrons in the tube. Since the readout electronics can not be continuously replaced to adapt for longer drift times and lower pulse heights, the high voltage has to be increased to compensate for the ageing effects. This in turn accelerates the ageing processes significantly. Other possible solutions to remove the deposits, like an inverse high voltage treatment during shutdowns with additives in the gas, were also tried [27]. The results were ambiguous.
If ageing effects are caused by contaminants in the gas mixture, they are limited to a section of the drift tube, until the contaminant has been deposited on the electrodes. Since the readout electronics is the same for the whole tube it is even more complicated or even impossible to account for the undesired effects.

Chapter 3

Ageing studies before 2004

Ageing experiments were carried out in Freiburg for a long time. Already in the planning stage of the ATLAS muon spectrometer different components, setups and gas mixtures were tested with respect to their ageing properties. As a consequence a gas mixture with good ageing properties was selected as operating gas for the MDTs. But in the Beatrice experiment carried out in the GIF[1] at CERN it was found, that tiny impurities in the gas system can cause severe damage to the drift tubes. Some of these experiments and their results are briefly summarized in this chapter.

3.1 Setups I-V, Merlin and Setup VI

In total seven ageing experiments are reviewed in this section. Six of them were built in Freiburg (*Setup I-VI*) and one at CERN (*Merlin*). The experiments labelled as *Setup I-V* were built at first and refer to five copies of the same experimental structure that could be operated with different settings. *Setup VI* had a different layout and was built later. The *Merlin* experiment was carried out between the experiments with Setup I-V and Setup VI.

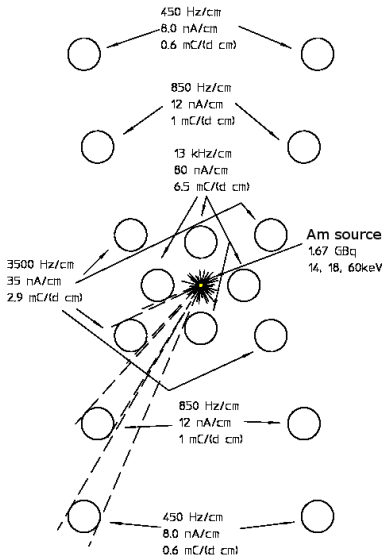

Figure 3.1: *Front view of Freiburg Setup I-V.*

3.1.1 Setup I-V

Each of the five *Setups I-V* consisted of up to 16 short (length 30 cm) drift tubes, mounted with varying distances from 4 to 24 cm to a radioactive ^{241}Am source. A schematic front view is shown in Fig. 3.1. An important feature of this setup was, that only 2.5 cm of each tube were irradiated by photons

[1] GIF: **G**amma **I**rradiation **F**acility

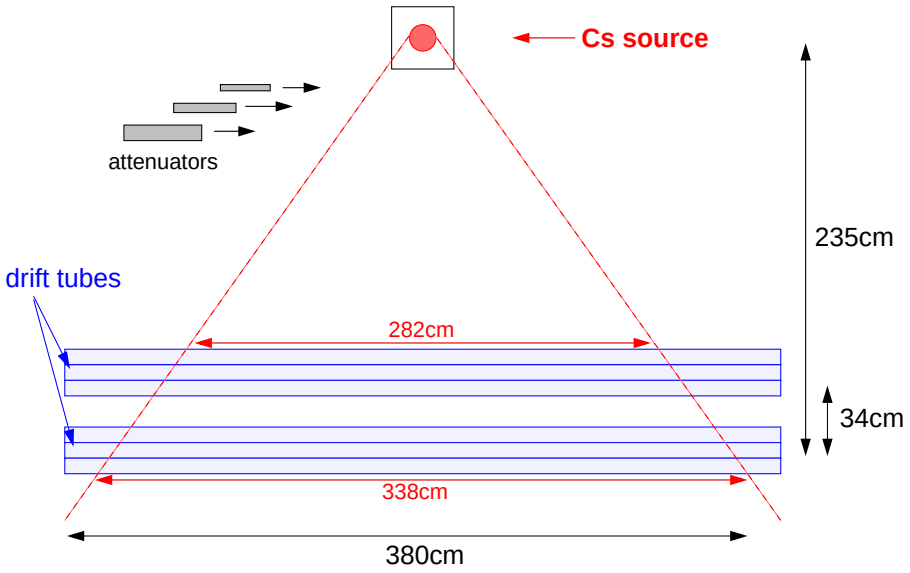

Figure 3.2: *The Merlin setup at GIF(CERN) in operation before 2002:* 96 *tubes with a length of* 3.80*m were irradiated by a* ^{137}*Cs source.*

with an energy of $E \approx 60$ keV from radioactive ^{241}Am sources. Almost all tubes were supplied with gas in parallel. These setups were intentionally built to find reliable materials and processes for the construction of drift tubes for the ATLAS MDT chambers: Different cathode surface coatings, end plugs for the drift tubes and cleaning processes were tested. Also drift tubes from different manufacturers were tried. A further important goal was to find an ageing-free gas mixture with good drift properties, such as linearity and high drift velocity (low maximum drift time → low occupancy). Therefore many gas mixtures and additives were tested with the various setups as well.
Another important task of this setup was to test how different parameters affect ageing. Therefore the operating conditions, such as the gas flow velocity, high voltage and irradiation rate of the different drift tubes were varied.

3.1.2 The Merlin experiment

A sketch of the Merlin setup can be found in Fig. 3.2. Photons with an energy of 662 keV from a 740 GBq ^{137}Cs source were used to irradiate drift tubes over a length of about 3 m. The Merlin chamber consisted of 96 drift tubes with a length of 3.80 m, grouped into four sectors with 24 tubes each. Each sector could be supplied with its own gas mixture and gas flow velocity. Two sectors were supplied with Ar-CH_4-N_2-CO_2 94-3-2-1 + 1200 ppm water. The other two sectors were operated with Ar-CO_2 90-10. For all sectors the gas was distributed in parallel to eight sets of three tubes (in series). The purpose of the Merlin experiment at CERN was to test a very promising gas mixture (Ar-CH_4-N_2-CO_2 94-3-2-1, successfully tested previously with *Setup I-V*) with optimized drift properties at high statistics. The mixture of Ar-CO_2 90-10 was also tested with high statistics as a fall back gas mixture in case

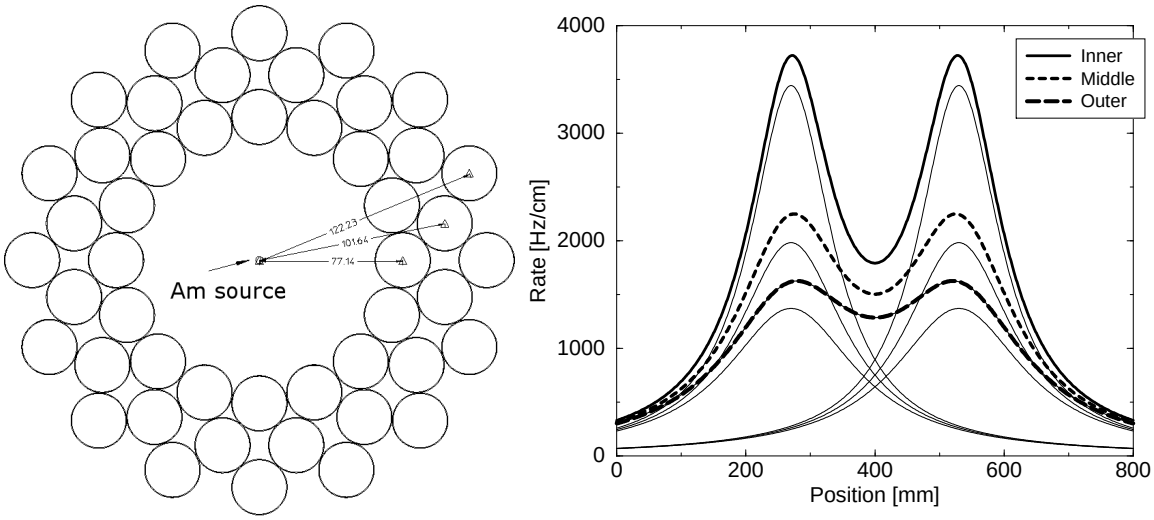

Figure 3.3: **Left:** *Front view of Setup VI. The tubes were* 80 *cm in length and were irradiated over their full length. The radiation distribution along the tubes is shown on the* **right** *picture.*

Name	Setup I-V	Setup VI	Merlin
Place	Freiburg		CERN
Length of used tubes	30 cm	80 cm	380 cm
Irradiated length	2.5 cm	80 cm	$\approx$ 300cm
Number of radioactive sources	1	2	1
Distance to source(s)	4 . . . 24cm	7.7 . . . 27cm	$\approx$ 200cm
Source type	^{241}Am (60 keV)		^{137}Cs (662 keV)
Voltage	3350 . . . 3680 V	3400 V	3400 V
Current density	9 . . . 85 nA/cm	$<$ 30 nA/cm	$\approx$ 50 nA/cm

Table 3.1: *Parameters of the ageing tests carried out in Freiburg and at CERN before 2002. Sketches of all setups can be found in Fig. 3.1, 3.2 and 3.3.*

of problems.

3.1.3 Setup VI

Surprisingly the *Merlin* experiment obtained results that were different from what was found with *Setup I-V*. Hence *Setup VI* was constructed in Freiburg to make further decisive tests. The main difference in the experimental conditions between Merlin and *Setup I-V* was the length of the irradiated region. For that reason *Setup VI* was conceived with longer tubes of 80 cm length, that were irradiated over their full length. For the irradiation two radioactive ^{241}Am sources were utilized to achieve a more "uniform" radiation distribution as with a single source. A sketch of *Setup VI* and a calculated radiation distribution are shown in Fig. 3.3. The main operation parameters of all three experiments are summarized in Tab. 3.1.

3.1.4 Results

Unfortunately the outcome of the experiments was such, that none of the gases with ideal drift properties could be used, because they all produced ageing effects. The important results are listed in Tab. 3.2 with the following additional remarks:

- Ar-CH_4-N_2-CO_2 94-3-2-1+1200ppm H_2O looked like the perfect gas for ATLAS with respect to its drift properties. In *Setup I-V* all tubes could stand far more than the required 0.6 C/cm of integrated charge. But in the Merlin setup at CERN (line 5, Tab. 3.2) a different result was obtained: Only some drift tubes operated at higher gas flow could sustain more than 0.6 C/cm. Others died[2] already after only 0.14 C/cm. This negative result was confirmed by *Setup VI* (line 6, Tab. 3.2), where the tubes could only stand about 0.08 C/cm in average.

- In Ar-CH_4-N_2-CO_2 94-2-2-2 ageing effects were also observed. In comparison with the gas above the drift tubes operated with only 2% of CH_4 could stand slightly more integrated charge, but still far below the desired value.

- In Ar-CF_4-N_2-CO_2 94.5-0.5-2-3 the methane is replaced by a low amount of CF_4. This gas is known to prevent ageing, but in the experiment ageing effects were found on the gas inlet side, away from the irradiated region. Using a microscope a black coating on the wire could be seen easily. Later it was found that CF_4 and water, that is always present on a low level, build up the aggressive hydrofluoric acid (HF).

- When adding ethanol to Ar-CH_4-N_2-CO_2 94-3-2-1 + 1200ppm H_2O a good ageing behaviour was found. But the plastic used for the end plug is affected negatively by alcohols, so that this gas mixture had to be rejected also.

- Drift tubes operated with the fall back gas Ar-CO_2 90-10 in the Merlin setup did not reveal signs of ageing.

- With a gas mixture of Ar-N_2-CO_2 90-5-5 ageing effects were observed. Still it is not clear whether these effects have to be attributed to the gas mixture or to the (imperfect) cleaning of the tubes.

One conclusion from the experiments described above was, that the observed ageing effects were due to the hydrocarbon content (CH_4) of the gas. In [28] the search for a optimal hydrocarbon free gas mixture for the ATLAS MDTs is described in detail. The important properties, such as after pulse rate, streamer rate, maximum drift time and linearity of several mixtures of Ar, CO_2, N_2 and water as additive were simulated with GARFIELD and measured partly. These experiments constrained the CO_2 content to 6-7%, whereas the fraction of N_2 had to be lower than 5%.

[2] tubes were classified as dead when the pulse height dropped below 70% of the pulse height at startup.

	Mixture/Additive	Setup	Ageing	References
1	Ar-CH_4-N_2 91-5-4	I-V	**failed**	[27]
2	Ar-CF_4-N_2-CO_2 94.5-0.5-2-3	I-V	promising	[27]
3	Ar-CH_4-N_2-CO_2 94-3-2-1	I-V	**failed**	[27]
4	Ar-CH_4-N_2-CO_2 94-3-2-1+1200ppm H_2O	I-V	promising	[27]
5	Ar-CH_4-N_2-CO_2 94-3-2-1+1200ppm H_2O	Merlin	**failed**	[29]
6	Ar-CH_4-N_2-CO_2 94-3-2-1+1200ppm H_2O	VI	**failed**	[27], [29]
7	Ar-CH_4-N_2-CO_2 94-3-2-1+water+ethanol	I-V	promising	[27]
8	Ar-CH_4-N_2-CO_2 94-2-2-2	VI	**failed**	[27], [26]
9	Ar-CO_2 90-10	Merlin	**selected**	[29]
10	Ar-N_2-CO_2 90-5-5	VI	→ **text**	[27], [26]

Table 3.2: *Summarized results of Freiburg Setup I-VI and Merlin. The details (gas flow velocity, high voltage, cleaning processes, cathode surface coatings ...) about all these measurements can be found in the references given in the last column.*

A remark on cleanliness

Further tests with the final gas mixture Ar-CO_2 93-7 + 600 ppm H_2O are also described in [28]. In particular two different end plugs were tested. By using one type of end plug, ageing effects were observed. In the manufacturing process of these end plugs araldite and a vacuum oil were used, while for the production of the other type of end plug none of the two materials was required.
As final conclusion one has to state that Ar-CO_2 93-7 + 600 ppm H_2O is a good drift gas for the ATLAS muonsystem drift tubes, if the gas system is free from impurities (like vacuum oils). There's no lower limit for the required level of cleanliness up to which ageing effects do not appear. In [32] ageing effects caused by an impurity level of less than 18 ppb are reported (for a different type of detector).

3.2 α-source test

Ageing studies performed within the framework of the HERA-B experiment showed, that different types of particles can lead to different ageing behaviour (see [30] and [31]) of the same detector type. In particular detectors that performed well in X-ray ageing tests can become inefficient very soon when exposed to a hadron beam, due to the different numbers of primarily created ions. Hence ageing experiments with six short (length $\approx$ 30 cm) ATLAS drift tubes, using weak α-sources for the irradiation, were carried out.

3.2.1 Setup

The range of α-particles in air is only a few millimetres; in aluminium they are already stopped after some microns. For this reason α-sources have to be installed within a drift tube. This was done by gluing the sources onto the inside tube wall with araldite. Additionally a thin movable shielding composed of stainless steel was

installed above the source (see Fig. 3.4). Thus the source could be switched "on" and "off" which was necessary to perform pulse height measurements outside of the irradiated region. The shielding had a big impact on the electrical field since it reduced the distance from the cathode to the anode. Consequently the pulse height in this region was intrinsically higher, so that only variations with time and along the shielding could be measured. The sources have an active length of ≈ 25 mm. Further details about the setup can be found in [28].

3.2.2 Results

Two of three tubes supplied with Ar-CH_4-N_2-CO_2 (94-3-2-1) showed strong deteriorations in the irradiated area; the third tube did not show any signs of ageing. Unfortunately also two of the three tubes supplied with Ar-CO_2 (93-7) showed little hints for ageing. But with this setup the situation was more complicated, since two tubes were mounted in series. The first tube seen in direction of the gas flow did not show hints for ageing, whereas the second did.

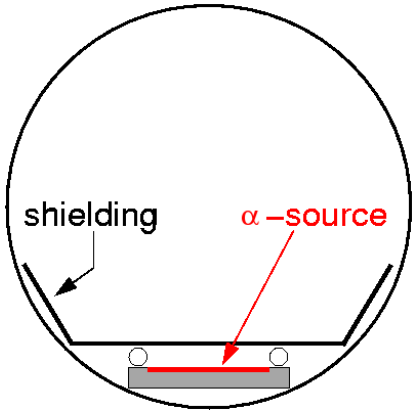

Figure 3.4: *Scheme of a drift tube equipped with an α-source.*

The interpretation of these results is difficult and ambiguous. Nevertheless it was assumed, that the gas mixture became slightly contaminated when passing the first tube. So the second tube received slightly polluted gas which led to the observed ageing effects. The contamination of the gas while passing the first tube was attributed to the araldite used to glue the α-sources into the tube. This assumption was not tested at that time, but now within the framework of this dissertation. Therefore a different α-setup was constructed (section 4.2).

3.3 Beatrice

The work described so far indicated a safe operation of the ATLAS muonsystem drift tubes with a gas mixture of Ar-CO_2 93-7. So another important experiment in the GIF (Gamma Irradiation Facility) at CERN was put into operation. With a prototype BIS[3] chamber - named Beatrice - the behaviour of a MDT in a high rate environment was examined. Furthermore components of the gas circulation loop should be tested.

3.3.1 Setup

Beatrice was a series-production ATLAS MDT chamber consisting of 240 drift tubes with a length of 1.70 m in total. The tubes were arranged in two multilayers with a

[3]BIS: **B**arrel **I**nner **S**mall

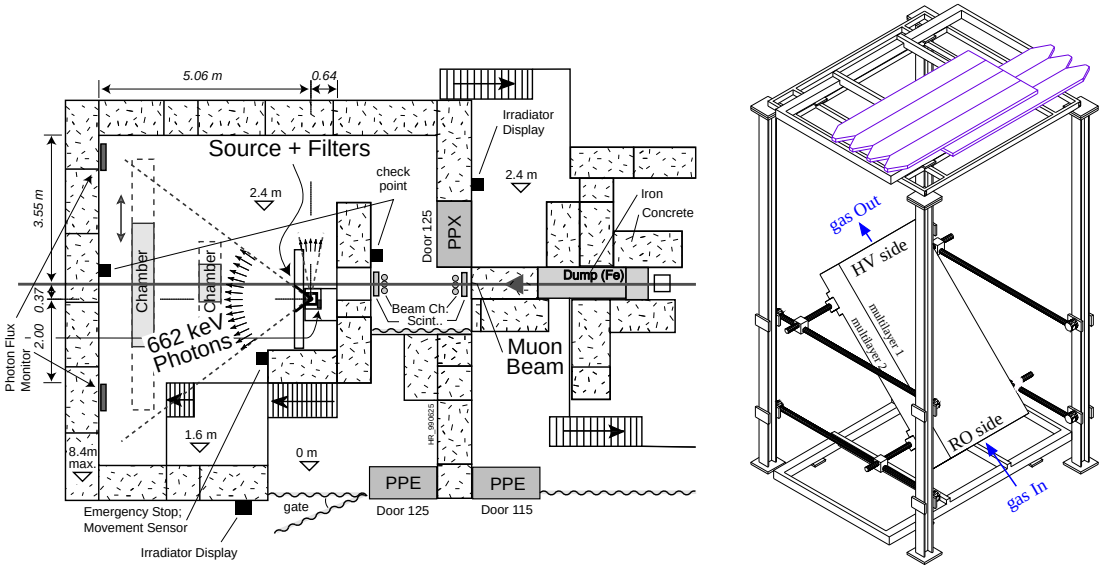

Figure 3.5: **Left:** *Layout of the GIF area at CERN. The approximate installation location of the BIS chamber is denoted by the outermost "Chamber" on the left side.* **Right:** *View of the BIS chamber and the trigger hodoscope.*

distance of 6 mm. Each multilayer consisted of four times 30 tubes per layer. The gas distribution to the tubes was done fully in parallel within the on-chamber gas system. The off-chamber gas system was different for the two multilayers:

- In order to test a gas recirculation system for ATLAS one multilayer was operated with a closed gas system.
- The other multilayer was operated in the flushing mode.

The whole chamber was mounted in the GIF at CERN. Besides the 740 GBq ^{137}Cs-source installed at GIF a weak muon beam was used to test the track reconstruction efficiency in a high photon background environment.
Additionally ageing studies were carried out with *Beatrice*. For this purpose a scintillator hodoscope, installed above and below the chamber, served as trigger for cosmic muons. A schematic view of GIF and the trigger hodoscope is shown in Fig. 3.5. The hodoscope provided a start time for the ADC measurement of the pulse charge generated by the cosmic muons in the drift tubes. By checking the measured pulse charge in regular time intervals ageing effects could be detected. The setup of the BIS chamber with the recirculation system and the trigger hodoscope is described very detailed in [24] and [25].

3.3.2 Results

The results of the ageing measurements were different for the two multilayers. For the multilayer operated in the flushing mode no ageing effects were observed

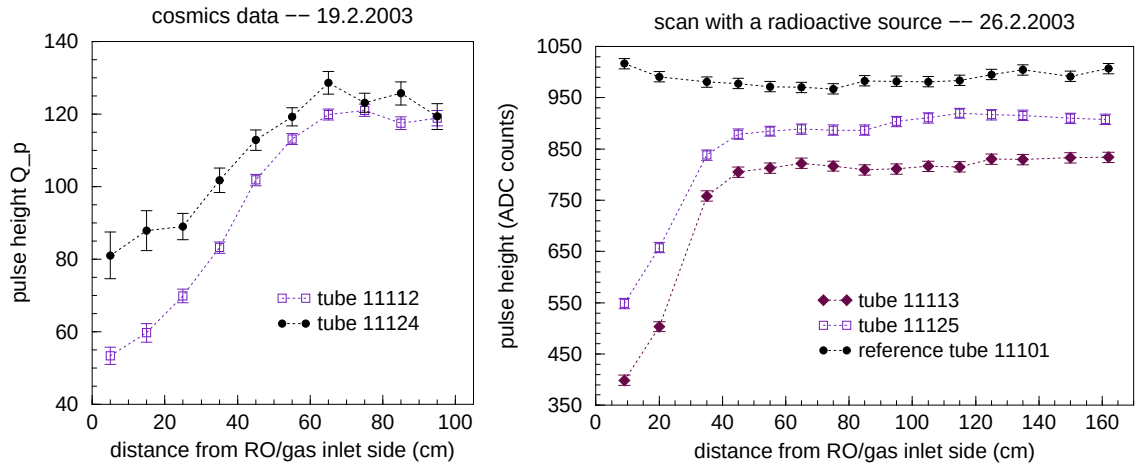

Figure 3.6: *Pulse height measured with the drift tubes in the BIS chamber versus the distance from the gas inlet. The measurements shown in the left plot were achieved with cosmics, for the right plot a small radioactive source was used.*

until the shutdown of the experiment after 5 month and an integrated charge of $Q_{int} \approx 170$ mC/cm (equivalent to about 3 years of ATLAS operation). In the drift tubes operated with the recirculation system severe ageing effects were observed. After accumulating only 20 mC/cm typical ageing effects became clearly visible (Fig. 3.6, left). As a cross-check the pulse height along the affected tubes was also measured with a small radioactive source, see Fig.3.6 (right). A characteristic feature of the observed effects was the fact, that only the first $20 - 30$ cm from the gas inlet were affected. After the irradiation of the BIS was terminated, some of the deteriorated drift tubes were opened. Samples from both, the anode and the cathode were removed and various chemical and surface analyses applied. In SEM[4] micrographs, as shown in Fig. 3.7, one can see needles (in the following called whiskers) with a length of several μm growing perpendicular to the wire surface. An EDX[5] analysis revealed that they were composed of silicon and oxygen.
By using IR-spectroscopy three large diameter valves of the bypass loop (which is part of the gas recirculation system) where identified as main source of silicon. These valves were taken from the TPC of the former LEP experiment ALEPH. Here they did not cause any problems during 10 years of operation. At LEP the accumulated charge was negligible in comparison to the conditions expected at LHC.

3.4 Conclusions

The important results of the earlier ageing experiment carried out in Freiburg and at CERN can be summarized as follows:

[4] **S**canning **E**lectron **M**icroscopy
[5] **E**nergy **D**ispersive **X**-ray

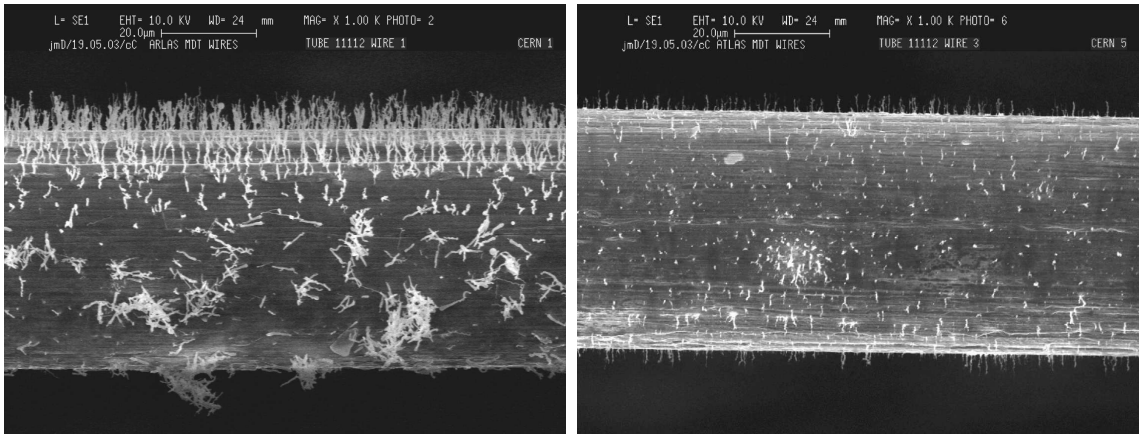

Figure 3.7: **Left:** *SEM picture of a wire* 15*cm away from the gas inlet. Needles with lengths of several µm are visible, whereas* 40 *cm away from the gas inlet there are only few of them and they are significantly smaller (***right***).*

- Ar-CO_2 93-7 is a safe operating gas for the ATLAS muon spectrometer drift tubes in terms of ageing.
- The obtained results are different for different irradiation lengths; in particular a short irradiation length can give a wrong impression.
- Impurities in the gas mixture, especially silicon compounds, can cause severe ageing effects.
- The level of pollution needed to deteriorate the tubes is not known; though the example with the valves taken from ALEPH shows, that the required level of cleanliness is much higher as for the LEP experiments.

The worry about traces of silicon compounds in commercially available components of the ATLAS MDT gas system made further ageing studies necessary. These are subject of this thesis and are described in detail in the following chapters.

3.5 Transferability of ageing results

The examples shown in this chapter already indicate, that there are difficulties to extrapolate ageing results from one setup to another. There are many more examples to show that ageing experiments are difficult in their interpretation. Often little changes of parameters have a big impact on the outcome of the experiment. Sometimes additives can prevent wire chambers from ageing, sometimes they cause the undesired effects. An excellent overview about ageing experiments in the past can be found in [22] and [33]. The plasma chemistry model outlined in section 2.4 can motivate the physical and chemical processes that happen in the highly active gas amplification region close to the wire. Anyhow there is no reason why the length of the irradiated range should play a role, as observed with the Setups I-V, Setup VI

and Merlin. Hence ageing experiments should always be carried out at conditions that are as close as possible to the final setup.

Chapter 4

Experimental setups

The alarming results, particularly from the *Beatrice* experiment described in 3.3.2, made further ageing studies with the ATLAS muon chamber drift tubes necessary. Consequently new ageing experiments were planned in Freiburg, where all the experience from previous experiments was used. The setup of the ageing experiment called the *component test* is described in Section 4.1. Section 4.2 describes the realisation of another ageing experiment with an α-source. Finally Section 4.3 introduces a very helpful auxiliary device, an adjustable silicone source.

4.1 The "Component test"

When reviewing all results described in the previous chapter, one of two possible conditions was fulfilled when ageing effects were observed:

- Hydro carbons were part of the gas mixture
- In a hydro carbon free gas mixture other impurities caused the deterioration of the drift tubes:
  - Araldite in the Freiburg end plug (section 3.1.4)
  - Araldite to glue the α sources into the drift tubes (section 3.2.2)
  - Silicone grease in Beatrice (section 3.3.2)

Although the former condition was excluded by using the hydro carbon free gas mixture Ar:CO_2 93 : 7, the latter remained as a serious concern for the ATLAS Muon collaboration. Many components used in the gas system for the muon chambers were supplied by industry. They could contain silicon compounds, although not listed in the product description. Hence these questionable components should be checked in ageing tests. The basic idea was to mount these components into the gas system of the newly planned ageing experiment and hereby use them as possible sources of impurities. The experiment is therefore called the *component test* in the following. For the setup of the component test the following aspects were considered:

- It was necessary to test many components. Consequently several individual test setups operated in parallel were needed.
- The test of a single component, in the following called a test station, should comprise several tubes to exclude random results with a high confidence level.
- The drift tubes should be irradiated over some length to avoid results as with *Setup I-V* (section 3.1.4)
- One end of each drift tube should remain unirradiated as a reference.
- Besides the components to be tested, only components already verified for the use in ATLAS should be used.
- The conditions had to be kept as close as possible to those in ATLAS, but the ageing process should proceed accelerated.
- One station in the experiment should run without any test component to check the gas quality of the main gas supply.

4.1.1 Mechanical setup

The mechanical setup of the *component test* can be separated in two functional elements. One element is the *irradiation box*, used for the irradiation of the drift tubes. Here the radioactive γ-sources were built in. The other element is the pulse height scanning system, required for the detection of local ageing effects along the tubes. Both were assembled close together in an air conditioned laboratory. They are described in the following sections.

Irradiation box

In Fig. 4.1 the setup is shown as a rendered image. The irradiation box is composed of brass with a wall thickness of 10 mm and outside dimensions of 100 cm $\times$ 48 cm $\times$ 34 cm (length $\times$ width $\times$ height). In total 38 drift tubes - grouped in 10 stations with 3 or 4 tubes - could be used to test components in parallel. They were arranged in 4 layers; two outer layers with a distance of 12 cm and two inner layers with a distance of 8 cm to the middle of the setup. By using short aluminium tubes (length 1.20 m) from Menziken which are also used for the BOG[1]-chambers in Freiburg, an unirradiated section with a length of $\approx$ 15 cm remains at one end of each drift tube. Recalling the results from *Beatrice*, where the measured deterioration appeared exclusively at the gas inlet side, it was decided to leave the gas outlet side unirradiated.
For the irradiation of the drift tubes nine ^{241}Am were installed in the middle of the setup. Seven sources have an activity of $1.7GBq$, the other two have an activity of 500 MBq. They emit mainly photons with an energy of $E \approx 59.5$ keV (for details

[1]BOG refers to specially designed T-shaped muon chambers in the feet of the ATLAS detector. They were designed and built in Freiburg

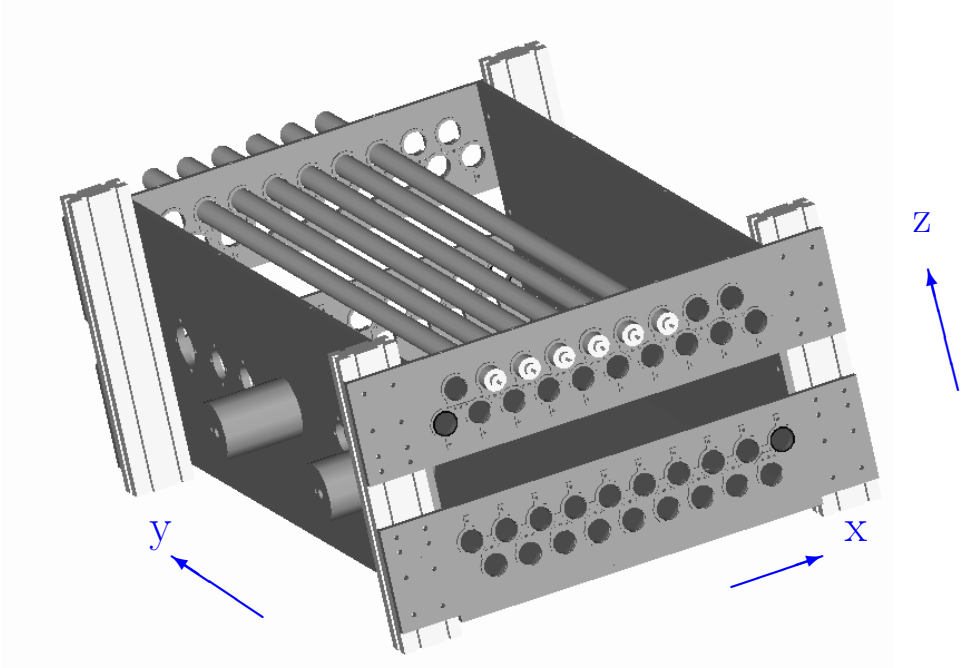

Figure 4.1: *Rendered image of the mechanical setup: The strong* ^{241}*Am sources could be inserted from the left. During pulse height measurements they were pulled out of the box; then they were completely covered by thick brass cylinders (two of them can be seen on the left side). The axes of the coordinate system, shown in blue, are used throughout the following chapters.*

see chapter 5). A conservative estimation yields that 10 mm of brass are sufficient to protect the environment from radioactivity. Only at the ends, where the drift tubes are fed into the irradiation box, photons can escape. Hence another box composed from 3 mm of lead was built around the ends (see Fig. 4.5). With a radiation dosimeter the whole setup was verified [35]. The positions of the radioactive sources within the *component test* were determined with a simple simulation. As input parameters previously measured counting rates (from [27]) of these sources at different distances were used. Various source arrangements were tried in a simulation with the intent to reach a high and a most uniform irradiation of all 38 drift tubes [34]. The "best" source positions were a compromise of both requirements and are shown in the scheme in Fig. 4.2. The sources were mounted on stainless steel rods to put them safely into and out of the irradiation box from the outside. In Fig. 4.3 the opened and empty brass box is shown from the top before the drift tubes were inserted. When pulse height scans were performed the sources were pulled back into brass cylinders with diameters of 65 and 80 mm. They were located on the outside of the box.

To monitor the temperature within the irradiation box, seven calibrated temperature sensors type PT 100 [36] were mounted at different positions in the box. Thus temperature gradients within the box could be detected. The calibration was performed simultaneously for all sensors in a temperature regulated oil bath with a calibrated precision temperature sensor.

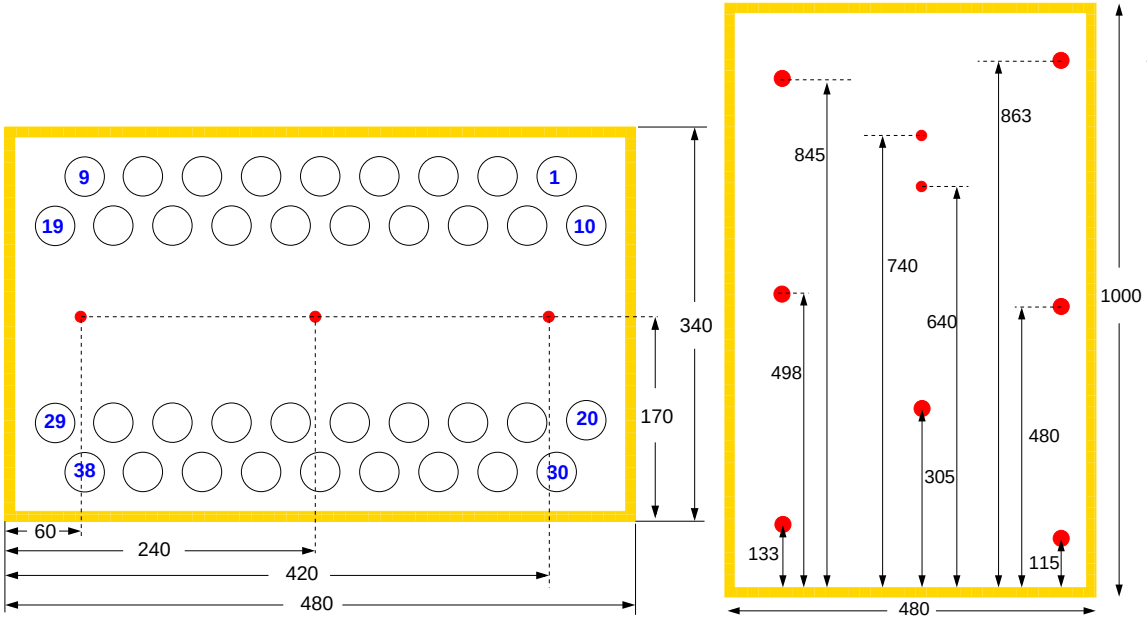

Figure 4.2: *Schematic layout showing the positions of the strong* ^{241}*Am sources used to irradiate the drift tubes. In the* **left** *scheme the setup is shown from the front, the* **right** *scheme provides a top view; both schemes are not to scale. The tube numbers in blue shown in the left scheme were used throughout the ageing experiment. The big red circles (right side) denote sources with an activity of* 1.7 *GBq, the smaller circles denote sources with activities of* 500 *MBq. All numbers are given in mm.*

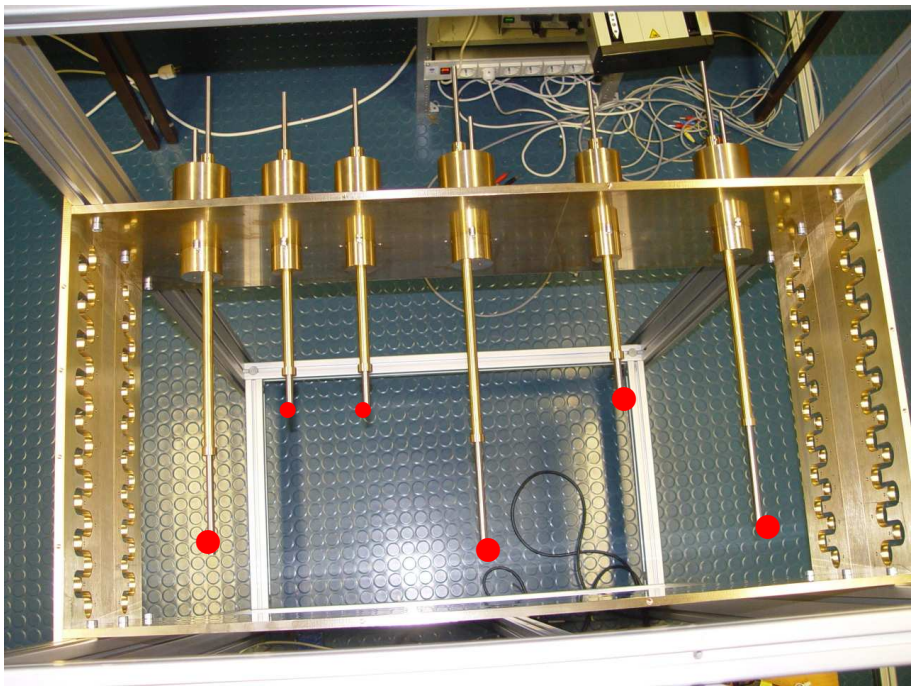

Figure 4.3: *Top view of the empty* component test. *When built in, the radioactive sources were on top of the stainless steel rods (indicated by the red circles for six of the nine sources). This picture corresponds to the scheme in Fig. 4.2 (right) rotated by* 90° *counter-clockwise. On the upper side one can see the big brass cylinders to park the irradiation sources during pulse height scans.*

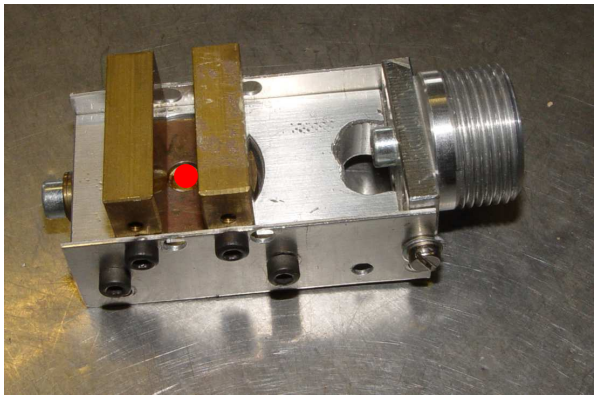

Figure 4.4: *A simple collimator, made of two rectangular pieces of brass, was used to restrict the range of the drift tubes irradiated at each position. The active region of the weak source is indicated by the red circle.*

Scanning system

Once a week the strong radioactive sources were removed and the irradiation box was opened to perform a pulse height scan along the tubes. For this a weaker ^{241}Am source with an activity of $A \approx 800$ kBq was used. This source is constructed differently from the strong sources so that also photons with energies around $E = 16$ keV are emitted. When these photons are stopped inside a drift tube, a clear photo peak can be observed (see chapter 5 for details).
The solid angle of photons emitted by the weak source was reduced with a simple brass collimator, see Fig. 4.4. Therefore only 30 mm in the inner layer and 50 mm in the outer layers were scanned at the same time. By moving the system of radioactive

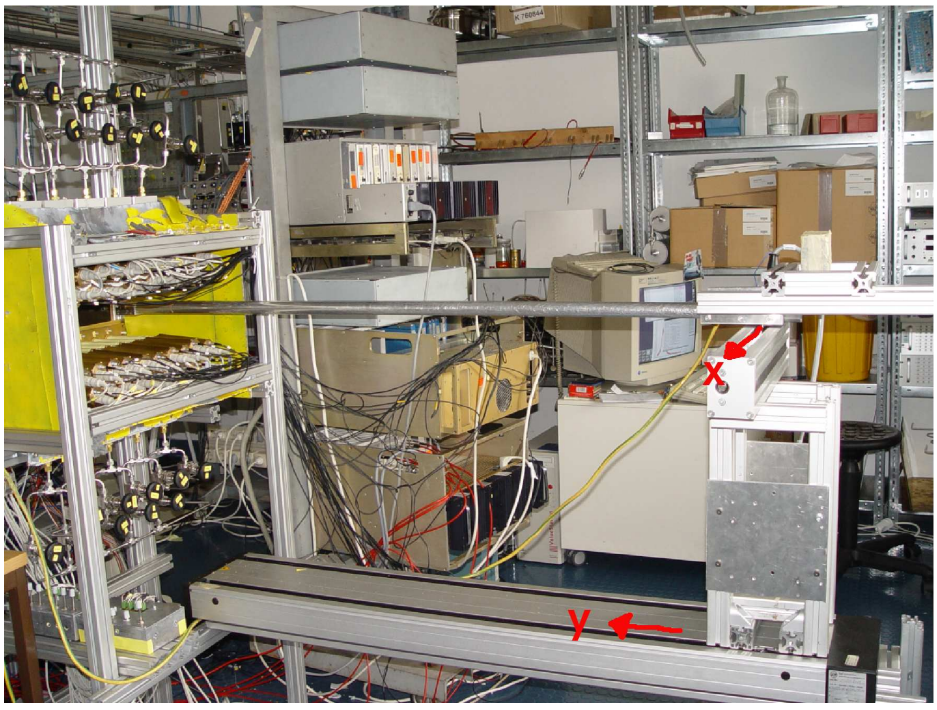

Figure 4.5: *The pulse height scanning system: The red arrows show the moving directions of the two slides. The lead box installed around the ends of the drift tubes is also visible.*

Figure 4.6: *Detail view of the fully assembled component test with the strong sources removed. The box is opened to allow for a pulse height scan along the tubes with the weak source.*

source and collimator with two stepping motors [41] and two slides along the x- and y-axis (as in Fig. 4.1), different tubes and different positions along the tubes could be reached. The reconstruction of the photo peak in the spectra, taken at different positions, allowed to inspect the drift tubes for local ageing effects. Pictures of the scanning system can be found in Fig. 4.5 and 4.6.

4.1.2 Gas system

A schematic overview of the whole gas system is given in Fig. 4.7. Each station of the *component test* was supplied with gas by electronic mass flow meters of type MKS 1179 [37] or MKS 1259 [38]. The gas mixture was taken from a buffer volume of 200 l, that was regularly filled up from gas bottles supplied by *SWF* (Sauerstoffwerke Friedrichhafen) and *Linde* with purities of 5.0 (Argon) and 4.5 (CO_2)[2]. The accuracy of the gas flow was hereby controlled by digital mass flow meters [39] operated by the *gasmix* software[3].

For the piping stainless steel gas tubes with an inner diameter of 4 mm were used. The connection between other gas system components and the pipes was completed with screwings supplied by Parker. The components of the ATLAS muon gas system, which had to be validated, were mounted into the gas line before the gas was split to the drift tubes on the gas inlet side. Thus volatile impurities (if present) were

[2]Format of the purity level: 5.0 refers to a purity of 99.999% whereas 4.5 refers to 99.995%.

[3]`C` program that controlled mass flow meters and pressure meters via the *FLOWBUS* (Bronkhorst) to adjust the right Ar:CO_2 ratio.

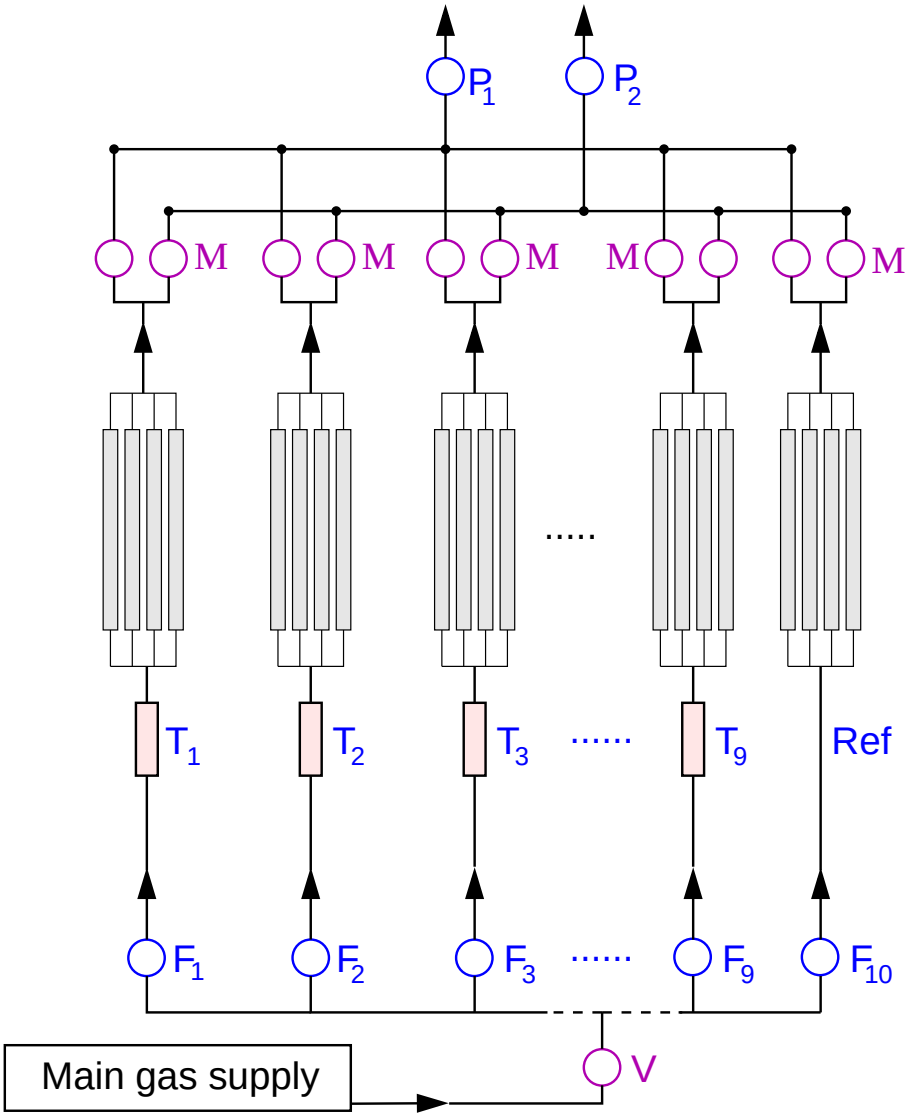

Figure 4.7: *Schematic layout of the gas distribution system. The gas flow to each station, testing the component T_n, was regulated by a flow meter F_n. One station (denoted by* Ref*) monitored the gas quality. At the end, the gas flow of all stations was collected and regulated by P_1 to a pressure of 3 bar. P_2 measured the regulated pressure or was used to exchange drift tubes of a single station (depending on the position of the manual valves M). V denotes a safety shut-off valve to separate the ageing experiment from the main gas supply in case of emergency.*

transported with the gas flow and distributed to all tubes of the corresponding station. The gas distribution system to the individual drift tubes used for the ATLAS muon chambers could not be used. Instead a simple gas distribution bar (*gas bar*, Fig. 4.8), made from aluminium, was designed to split the gas of each station to the single drift tubes. To cover the distance from the *gas bar* to the individual drift tubes, stainless steel tubelets as for the ATLAS muon chambers were used. Then the gas entered the drift tubes via the gas jumpers (see Fig. 2.1). On the outlet side the same system of gas jumper, tubelets and gas bar was used.

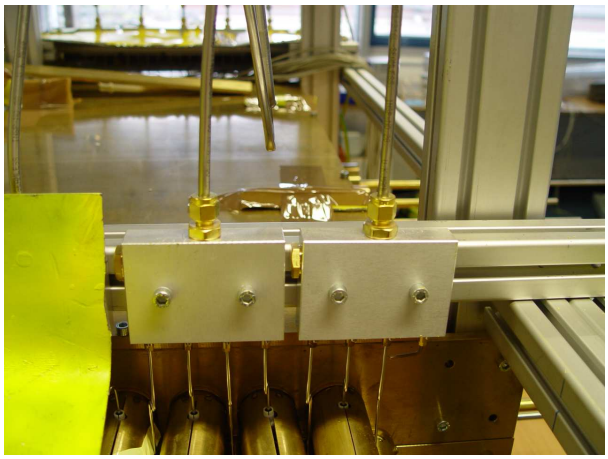

Figure 4.8: Gas bars *designed for the* component test. *The tubelets to the individual drift tubes were taken from the ATLAS muon gas system.*

Finally the gas of all stations was collected with manual valves in two independent gas lines and regulated to an absolute pressure of 3 bar. The usage of two gas lines offered two advantages: Primarily it was possible to exchange the tubes of one station while the tubes of the other stations still were operated at 3 bar. Further it was known from previous experiments [27] that a pressure regulator can either measure or regulate the pressure precisely, but not both at the same time. Thus the second pressure meter could also be used to monitor the regulated pressure more precisely. The different measurements of the two pressure meters can be seen in Fig. 4.9: While the regulated pressure had a variation of about 0.3 mbar, the pressure sensor in the regulating pressure meter reported no variation at all.

4.1.3 Electronics

Both sides of the drift tubes were connected to electronic circuits to supply them with high voltage and for signal readout. These circuits are described in the following. Further a slow control system to monitor important operation parameters is described.

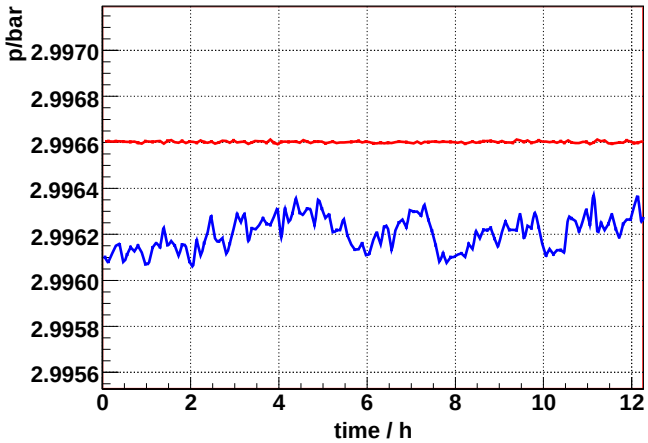

Figure 4.9: *Operating pressure of the drift tubes as measured with the pressure meters P_1 (red) and P_2 (blue) during $\approx$ 12 hours. The oscillation were measured to about* 0.3 *mbar by P_2, whereas P_1 (the pressure regulator) reports no oscillation.*

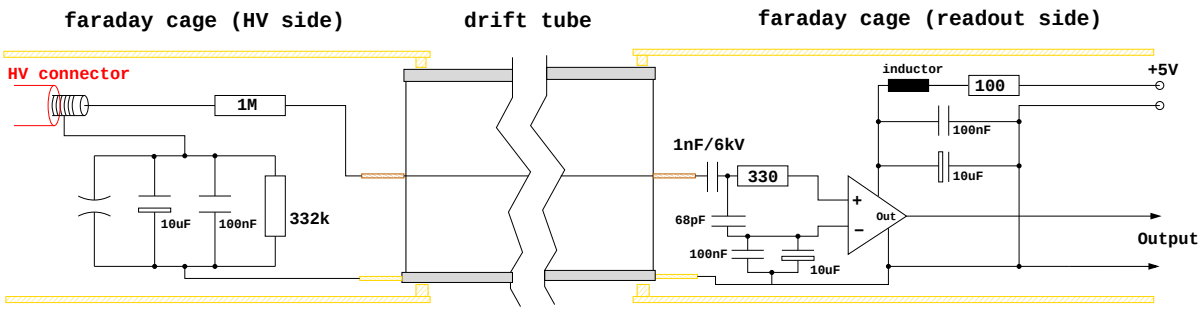

Figure 4.10: *Electronics on the high voltage side (***left***) and readout side (***right***) of a single drift tube. The circuits on both sides are surrounded by a Faraday cage made of brass.*

High voltage side

One side of the drift tubes was connected to high voltage as shown in Fig 4.10 (left): The actual connection of the high voltage to the anode wire is realized with a 1 MΩ resistor. The ground is connected indirectly with the tube via another resistor (332 kΩ), two capacitors and a spark gap in parallel. The drift tube itself can be seen as part of the circuit. When the drift tubes are irradiated the transport of separated charges inside the drift tube represents a current. This circuit is closed by the electrical components on the outside. Thus the current leads to a measurable voltage drop over the resistor[4] with 332 kΩ. The measurement of this voltage was done regularly with an automated slow control system (see below) to monitor the current in the drift tubes. For fast signal the capacitors parallel to the resistor mean a direct connection between the tube's ground and the ground of the high voltage power supply. The spark gap served as a safety feature in case the voltage drop increased above 50 V.
The high voltage was supplied by HV NIM-modules Model 5900 from Vern Kiebler, Illinois. They provide two adjustable voltages up to 10 kV with a current limiting of maximum 1 mA. In total three HV modules were used.

Readout side

On the readout side a pre-amplifier [40] developed for the muon detector of the L3 experiment was used. The adaptation of the amplifier to the drift tubes is described in [27]. The circuit layout is shown in Fig. 4.10 (right) with the following functions of the circuit elements:

- Noise reduction on the positive supply voltage line with the inductor, the 100 Ω resistor and the two capacitors (100 nF and 10 μF) to ground.

- Noise reduction by two capacitors with the same capacities as above between the tube's ground and the ground of the supply voltage.

[4] There is an even bigger voltage drop over the 1 MΩ resistor. But for safety reasons the voltage drop was not measured at the high voltage level.

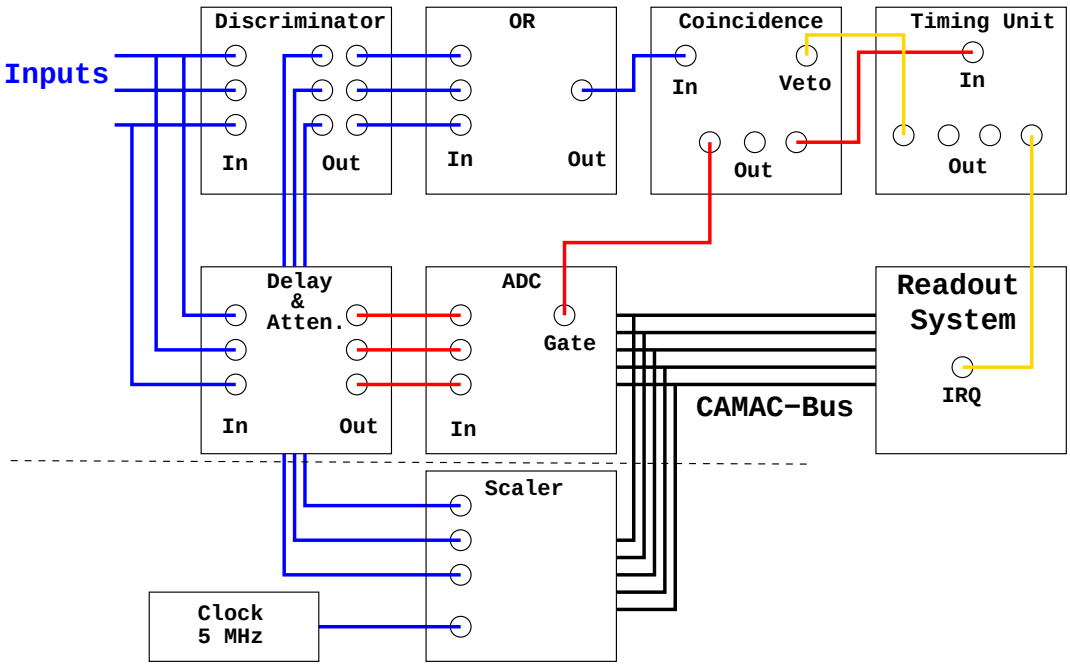

Figure 4.11: *Time-to-colour coded readout cycle for pulse height scans. The colour code has to be read in the following order: blue, red, orange, black. The readout system (realized with two computers, see Fig. 4.12 and section 4.1.4) on the lower right side of the scheme is the end of the cycle. The part below the dotted line belongs to the slow control system and is only shown for the sake of completeness.*

- Adaptation of the tube's impedance ($\approx$ 382 Ω) with the 330 Ω resistor and the input impedance of the amplifier ($<$ 50 Ω). Fast signals are bypassed to ground via the 68 pF capacitor.

The impact of the adaptation electronics to the signals originating from drifting ions was calculated with a transfer function and is described in the appendix B. The L3 pre-amplifier provides an output impedance of 50 Ω. Therefore signal processing with standard NIM-electronics could be performed. The signal was split into two parts: One part was delayed and attenuated by a factor of 4 to adapt to the input level of CAMAC[5] ADCs [42], which were used to measure the pulse height. The other part of the signal was processed in the following way with standard NIM[6] modules (see also Fig. 4.11):
A discriminator [43] with a threshold of $\approx$ 60 mV removed most of the noise. The logical output signal of the discriminator was fed into 16-fold OR-units [44] together with the logical signals from other discriminators. The output of the OR-unit was then connected to a coincidence unit [45] where only a single input was used. The coincidence unit provided two important features: An output signal with an adjustable width and a veto input. The output signal was used to open the gate of the ADCs for 500 ns. On the other hand a timing unit [46] was started which in

[5] **C**omputer **A**utomated **M**easurement **A**nd **C**ontrol
[6] **N**uclear **I**nstrumentation **M**odule

turn blocked the input of the coincidence for 2 μs. The timing unit further triggered an interrupt in the OS9 readout system, so that the ADCs were read out (see next section for details). During the read out cycle on the CAMAC bus noise could be transferred to the input signal lines. Due to the vetoed coincidence unit these signals were ignored. A scheme of the readout chain is shown in Fig. 4.11. Most of it was only used when performing pulse height scans along the drift tubes. From the discriminator outputs the logical signals were also fed into a scaler unit [47] to obtain a counting rate for the drift tubes. This was also done when the tubes were irradiated.

4.1.4 Slow control

In Fig. 4.12 an overview about the slow control system is shown. Two computers managed the whole data taking including slow control. One computer was running under `Linux`; here the `slow-control` software package described in [49] was installed. The other computer was realized as a VME[7] Crate Controller BAB60 [52], set up with the real time operating system `OS9`. Between the two computers a `TCP/IP` over Ethernet connection was established. Whenever the slow-control program asked for sensor data, the request was transmitted to a server-software running

[7] **V**ersa **M**odule **E**urocard

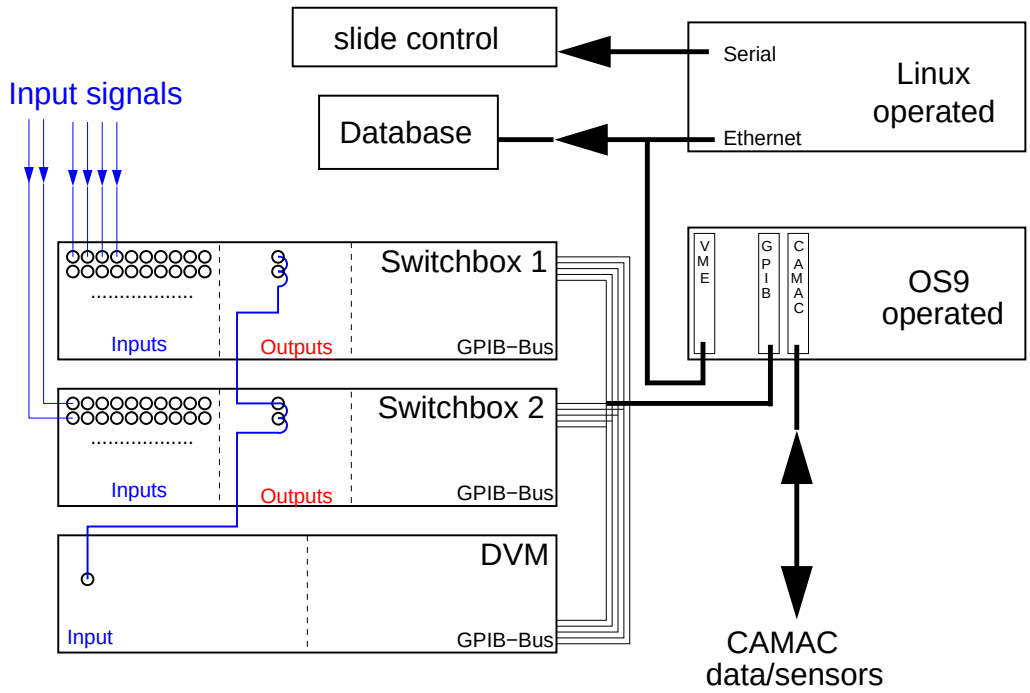

Figure 4.12: *Overview of the slow control system. The input signals were bipolar cables from sensors like pressure meter, flow meters, high voltage supplies .... They were switched to the DVM with relays in the two switch boxes. All three devices were connected to the GPIB-Bus for control and readout.*

on the VME controller board. Depending on the sensor type, the server software collected the required information with the help of a GPIB[8]- or a CAMAC-Controller. In total data from 75 sensors was collected regularly:

- 7 temperature sensors placed within the irradiation box (GPIB)
- The currents of 38 drift tubes (GPIB)
- Up to 3 pressures of the ageing setup (GPIB)
- Up to 11 counting rates of selected drift tubes (CAMAC)
- The 10 gas flow rates to the stations (GPIB)
- Up to 6 different high voltages applied to the drift tubes (GPIB)

A GPIB serviced sensor was read by connecting the sensor with a switching unit [53] to the inputs of a DVM[9][54]. Then the DVM was read several times, until the measured value was stable. This turned out to be necessary for tiny voltages. Otherwise a random value was returned due to internal capacities of the switching units and the DVM.
For the measurement of the counting rates the procedure was different: With an CAMAC outregister [48] a timing unit was triggered to open the gate of a CAMAC scaler for about 250 ms. The signals from the discriminator outputs of some tubes were connected to the input of the scaler (see Fig. 4.11). Thus the pulses in these tubes were counted during that time. By comparison with the number of counts from a 5 MHz clock, the counting rates could be calculated.
The measured values of the sensors were used for several purposes: The high voltage and flow sensor information was used together with the operating pressure of the tubes to control an emergency shutdown system. With the current measurements the integrated charge of the individual tubes was calculated. Finally the temperature, pressure and high voltage sensor information was used to estimate the change of the pulse height due to changes in the operating parameters during a pulse height scan (see section 6.2).

4.1.5 Software

The software package programmed for the component test can be subdivided into three major tasks: slow control, software for the control of the pulse height scans and data analysis software. In the following software used for the pulse height scans is described. The analysis tools are discussed in chapter 6. The slow control software has already been described above.

[8] **G**eneral **P**urpose **I**interface **B**us
[9] **D**igital **V**olt **M**eter

Scanning the local pulse height

For the pulse height scans along the drift tubes an advanced control and readout software was needed. On the one hand, the position of the weak source along the different tubes had to be controlled. On the other hand, data had to be read out from the ADC modules. A simple pre analysis was performed to decide whether to leave the weak source in its current position or whether to move on.
When started, the software read from a configuration file which tubes had to be scanned. Further the scan positions along the tubes (y-axis in Fig. 4.1) were listed in the configuration file. The weak source was moved with the help of slides under control of the readout software to the first position on the first drift tube. The pulse height was measured with the ADC and read out. The positions of the photo peak, as expected from previous measurement, were also stored in the configuration file that was read at start-up. The read out control left the weak source in its current position until a certain number of entries in the vicinity of the expected photo peak value were obtained. Then the source was moved to the following drift tubes (x-axis in Fig. 4.1). When all tubes were scanned in this particular y-position, the source was moved on to the next y-position along the first tube.
Ageing effects will result in a lower pulse height. Hence the range, where the photo peak was searched, was adjusted after each y-position to adapt for occasionally lower pulse heights. A standard pulse height scan comprised 23 positions[10] along each tube, two of them in the unirradiated reference zone. Depending on the number of tubes scanned together a complete scan lasted 2 hours at the maximum.
The readout software itself was realized in the two computers already mentioned above. The computer operated with `Linux` controlled the position of the weak source. The data from the ADCs was transferred over `TCP/IP` from the VME-Controller operated with `OS9`.

4.2 α-source ageing experiment *Clean-α*

The previous ageing experiments with an α-source carried out in Freiburg ended with ambiguous results (see 3.2.2). The observed ageing effects on some tubes were supposed to be caused by araldite used in the setup. Hence a new α-experiment was developed to clarify this assumption. In the new construction neither araldite nor any other component that can introduce volatile impurities to the gas system were used. Instead a different method was used to insert α-particles into a drift tube: Since α particles can not penetrate the tube wall, a hole was drilled into the wall of the drift tube. The α-source was mounted with a gas tight collar above the hole onto the outside of the drift tube. But the source was still movable within the collar (see Fig. 4.13). Thus the aluminium wall of the drift tube could be used to "switch" the source on and off, depending on the position of the α-source. A strong magnet, that acted on the iron support structure of the source holding, was used

[10] To scan at closer distances was not reasonable due to the length of the irradiated range.

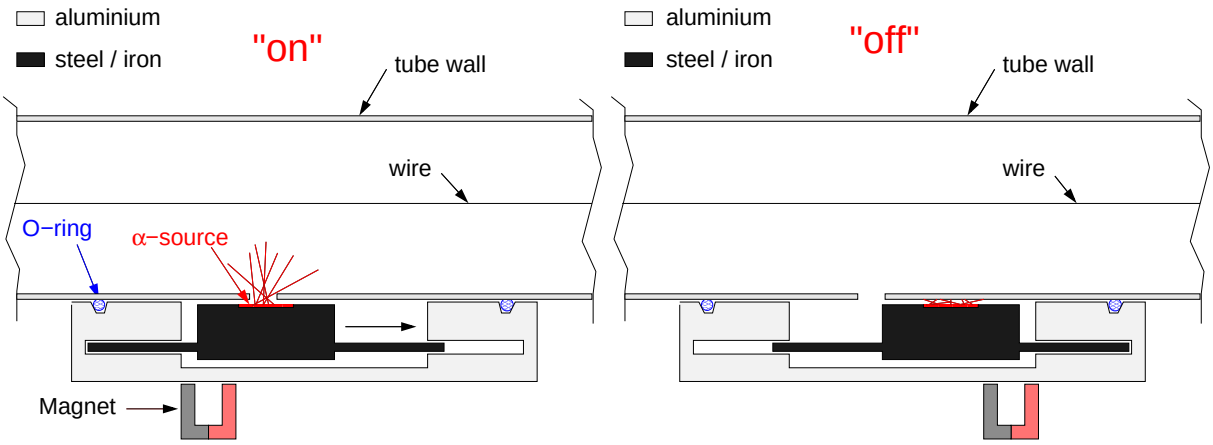

Figure 4.13: *Setup of the new ageing experiment using α-particles for the irradiation. In the left (right) picture the source is switched on (off). In order to switch the irradiation on and off a strong magnet was used.*

to move the radioactive α-source. A layout of the experimental setup is shown in Fig. 4.13, a picture of the collar can be found in Fig. 4.14.
The α-sources were bought from Amersham [50] and provide α-particles with energies of $E \approx 4$ MeV from a rectangular surface of 25×5 mm^2. The hole in the drift tube had a diameter of 7 mm and therefore reduced the numbers of α-particles that could reach the inside of the tube. A geometric simulation of the setup is described in section 5.5. With its help the irradiated range along the drift tube wire could be estimated to about 1 cm.

Services: The high voltage supply and read out electronics of the drift tube in the ageing experiment "Clean-α was identical to those used for the *component test*. Solely the gas distribution was changed because only a single tube had to be supplied with gas. Therefore a simple reduction from 6 mm stainless steel pipe to 2 mm brass tubelets was used on the gas inlet side and vice versa on the gas outlet side.

Figure 4.14: *Collar to mount the α-source onto a drift tube. The red arrow points to the rectangular area of* 25×5 *mm*^{2} *from where α-particles are emitted.*

4.3 Auxiliary Device: HMDS source

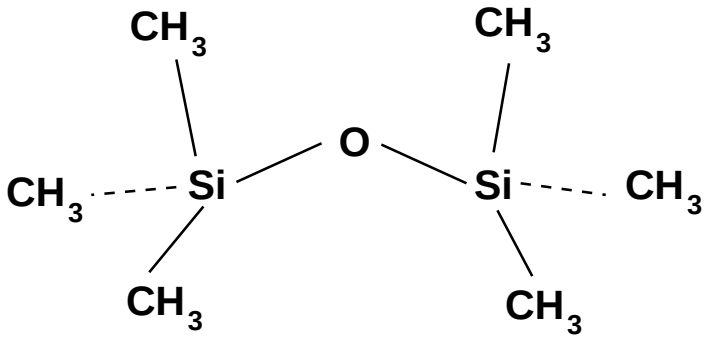

Figure 4.15: *Chemical structure of the silicon compound HMDS. It was used to simulate silicon contaminations in the drift tubes.*

After the first ageing measurements it turned out, that an adjustable silicone source would be a useful device to simulate silicone pollutions for the drift tubes. For this purpose the liquid silicon compound **H**exa-**M**ethyl-**D**i-**S**iloxan (HMDS) was used. HMDS is a silicone compound with a low molecular weight and a high vapour pressure. Its chemical structure is shown in Fig. 4.15.

4.3.1 Working principle

The estimation of silicone concentration in the gas flow is based on the vapour pressure of HMDS. The vapour pressure as a function of temperature can be calculated with the Antoine equation:

$$\log p_{HMDS}(T) = A - \frac{B}{T + C} \tag{4.1}$$

where A,B and C are the Antoine parameters and T the absolute temperature of the liquid. Note that the equation uses the logarithm to the basis 10. Taking the Antoine parameters from [51]

$$A = 6.901 \pm 0.002 \qquad B = 1203 \pm 1\text{K} \qquad C = -64.8 \pm 0.1\text{K} \tag{4.2}$$

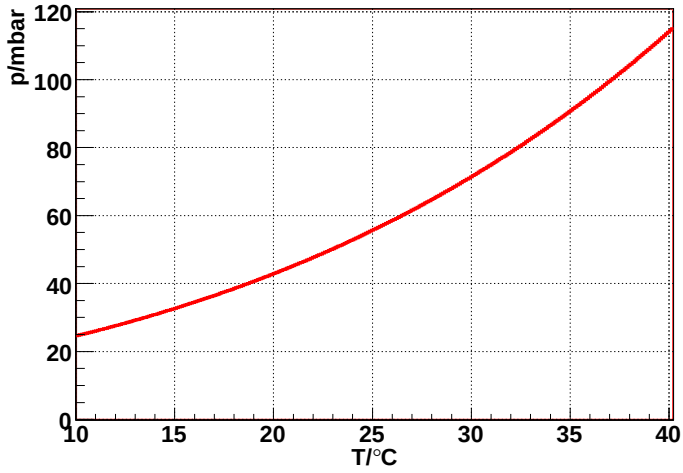

Figure 4.16: *Vapour pressure curve of HMDS fitted to data from [51]. For room temperature ($T = 22°C$) one can determine a vapour pressure of $p \approx 48$ mbar.*

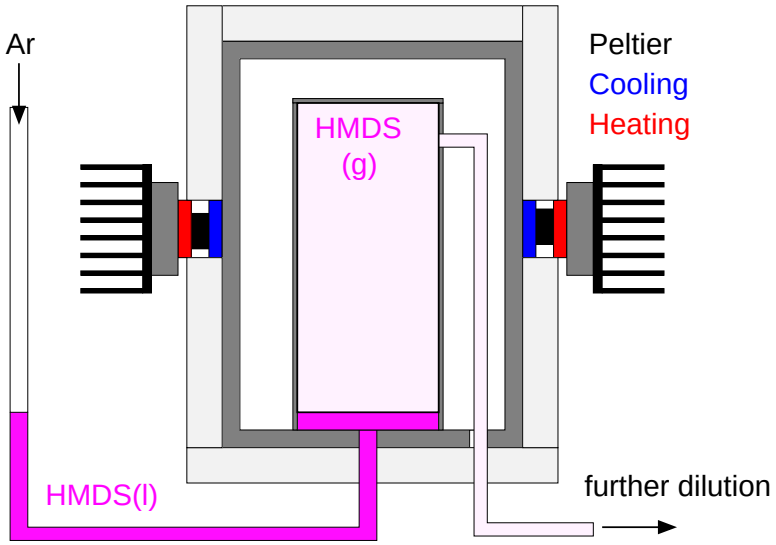

Figure 4.17: *Scheme of the silicone source. From below Argon was bubbled through the liquid HMDS at a low rate. With the peltier elements the temperature and thus the vapour pressure of HMDS could be adjusted.*

the vapour pressure curve shown in Fig. 4.16 is obtained. For room temperature a vapour pressure above 40 mbar can be expected, giving a HMDS concentration of more than 1% at 3 bar. This is way too much and would have deteriorated the drift tubes within a few hours (see Section 6.5). Hence the concentration of HMDS was further reduced by mixing with clean Ar:CO_2 93 : 7.

In Fig. 4.17 a schematic diagram of the silicone source is shown: Argon bubbles at a low flow rate of $F_1 \approx 1 \ldots 2$ ml/min through liquid HMDS into a vessel with a volume of $V \approx 0.6$ l. In the vessel a temperature dependent equilibrium of liquid and gaseous HMDS molecules is acquired. At the outlet a saturated gas mixture of argon and HMDS is provided at a low flow rate f_1. The temperature of the vessel was regulated with peltier elements. The whole setup was packed in Styrofoam for insulation (Fig. 4.19, page 54). With three more flow meters and a pressure meter the concentration of HMDS was further reduced (see Fig. 4.18). In the end the following concentration was reached:

$$c_{HMDS} = \frac{p_{HMDS}(T)}{p} \cdot \frac{F_1}{F_1 + F_2} \cdot \frac{F_3}{F_3 + F_4} \tag{4.3}$$

with the flow rates F_i $(i = 1, 2, 3, 4)$ and p as in Fig. 4.18. The overall flow rate is given by $F = F_3 + F_4$.

Problems and uncertainties: The concentration of HMDS could be changed by many different parameters: The temperature T of the HMDS, the pressure p in the vessel and the four flow rates F_i. Therefore also many systematic uncertainties added up and had to be considered. The manufacturer of the flow meters gives the systematic uncertainty of the actual flow rate with respect to the full scale. Hence the relative error can become quite large at low flow rates. To adjust a low HMDS concentration, the flow meters F_1 and F_3 have to be operated at a low flow rate. Then the uncertainty on the given concentration is about 20% at 10 ppm.
Besides the accuracy of the flow meters further uncertainties and systematic errors have to be considered:

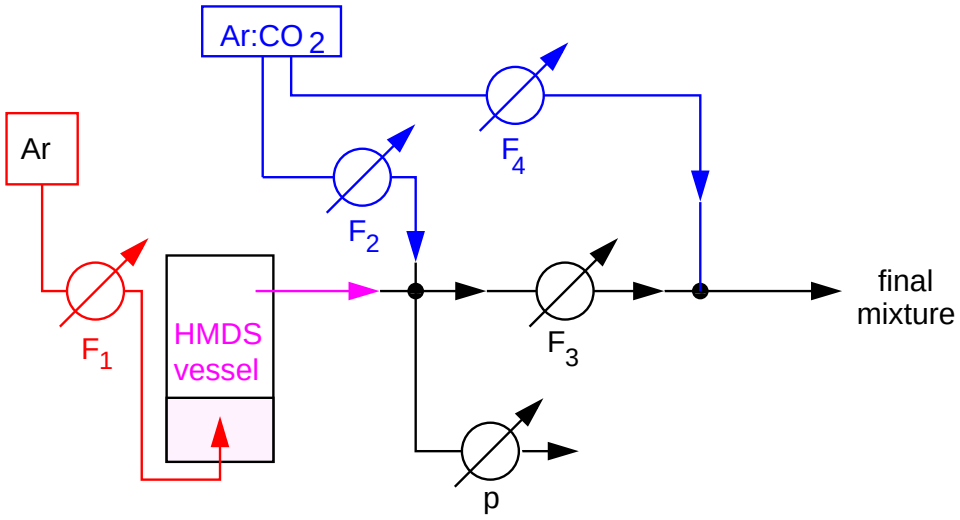

Figure 4.18: *With the help of four flow meters and a pressure meter the silicone concentration could be varied over three orders of magnitude.*

- The flow meters regulate the gas flow by measuring the heat flow between two sensors. HMDS will not only change the heat capacity of the flowing medium, but possibly deposit on the sensors and in between. Thus the calibration of the flow meters will be changed.
- When the concentration of HMDS was changed, the whole construction of pipes, vessel and flow meters has to be seen as a buffer that has to adapt to the new HMDS concentration. Fast changes were therefore not possible, in particular when changing to a lower concentration of HMDS.

These difficulties limited the possible applications of the silicone source as a precisely calibrated device. Nevertheless it turned out to be very useful.

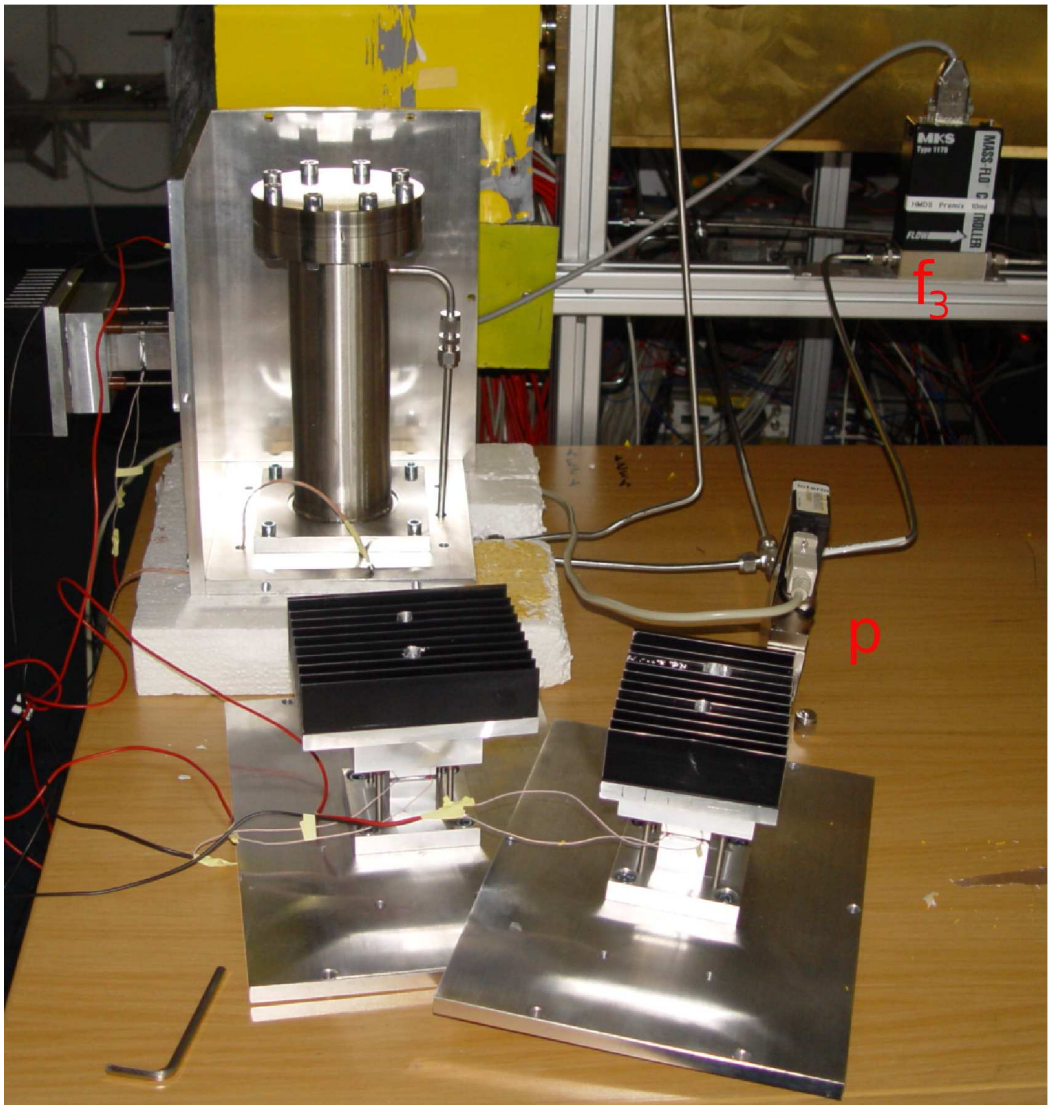

Figure 4.19: *Picture of the silicone source. In the background the vessel containing HMDS can be seen. In the foreground two peltier elements with radiators are shown. Two more are already attached to the vessel. Furthermore one flow meter (f_3) and the pressure regulator (p) for the vessel are visible. After attaching the remaining two peltier elements to the vessel the whole setup was packed in Styrofoam.*

Chapter 5

Monte Carlo Simulation

A Monte Carlo simulation was developed to estimate the irradiation distributions along the single drift tubes. Thus the local current densities can be calculated. In order to get reliable result the radioactive sources and their housings had to be simulated also very accurately. In Section 5.1 the requirements for the Monte Carlo simulation are defined. Section 5.2 describes the basic ideas of the simulation algorithm. The limits of the simulation are explained in Section 5.3. A comparison of data with Monte Carlo is performed in Section 5.4. Finally a simple simulation for the ageing experiment with the α-source is shown in Section 5.5.

5.1 Requirements

The Monte Carlo simulation should provide detailed answers for the following questions and problems:

- The measured spectra of the weak and the strong radioactive ^{241}Am sources look very different. Are the differences due to space charge effects?
- The weak source used for the pulse height scans is equipped with a collimator. Does the collimator change the spectrum? What is the length of the irradiated section along each tube in the different layers of the setup?
- 9 radioactive sources were used to irradiate the drift tubes in total. The slow control readout only allows to measure the total current and counting rate of a tube. How does the current density vary along each tube?
- The measurement of the counting rates turned out to be difficult due to heavy noise at the increased gas gain. Furthermore the counting rate could only be measured for some selected tubes. The Monte Carlo should provide information about the (local) irradiation rates of all tubes.

In ageing tests carried out later (started in summer 2007), individual drift tubes were partly shielded with thin lead jackets. Further the position of the radioactive sources was changed to enforce the irradiation of other parts of the drift tubes. That

way a highly non-uniform irradiation was achieved. The Monte Carlo should give an impression of the new radiation distribution resulting from the modified source arrangement. Thus the desired radiation distribution could be found rather quickly.

5.2 Setup of the Monte Carlo

The basic idea of the simulation is to track the path of photons leaving the radioactive ^{241}Am sources. All possible processes (photoelectric absorption and Compton/Thompson scattering, see also section 2.2.1) that can happen to the photon on its path should be included in the simulation. If a photon liberates an electron inside a drift tube it gives rise to a signal (section 2.2.2). In a Monte Carlo simulation the energies and positions of photons and electrons are well known. Therefore the amount of separated ions and electrons along the drift tube wire can be determined locally. Thus the local irradiation and current density can be estimated.
For reasons of simplicity the simulation was subdivided into three distinct steps:

- Emission of photons from the sources
- Conversion of photons into electrons (in the following called *basic algorithm*)
- Electron tracking and signal generation in the drift tubes

These steps are explained in the following subsections. But at first the different material used for the construction of the ageing experiment are discussed.

5.2.1 Materials in the ageing setup

There are basically 10 different materials used in the ageing setup (see Tab. 5.1). The probability for photoelectric absorption or scattering processes can be calculated

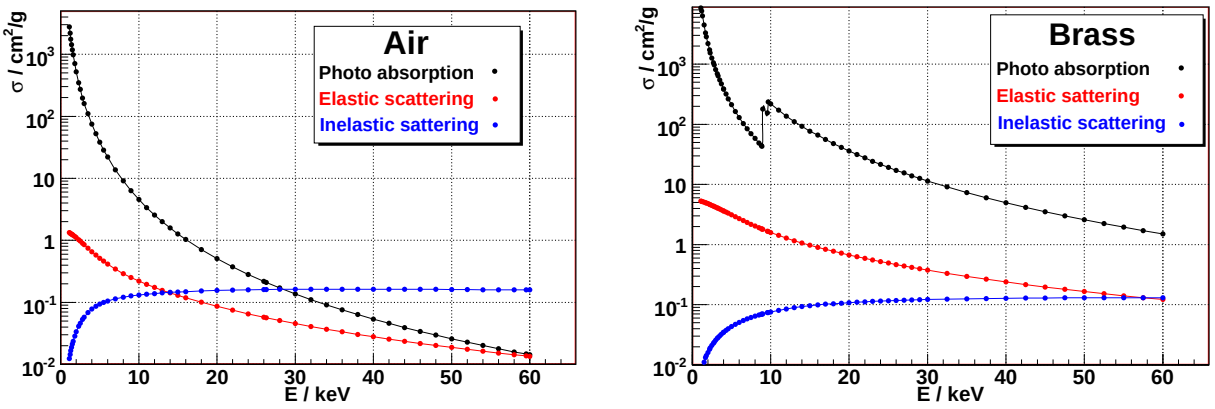

Figure 5.1: *Photon absorption coefficient σ in air (left) and brass (right) for different photon energies E. In the right plot the K-shell resonances of Cu and Zn can be seen. The data points are extracted from the XCOM database [61].*

Material	Step size	Location
Ar/CO_2 : 93/7	500 μm	inside tubes
Aluminium	20μm	tube wall
Brass	200 μm	shielding, rods
Lead	100 μm	shielding
Stainless steel	10 μm (sources) 50 μm (rods)	γ-sources, rods
Gold	50 nm	γ-sources
Silver	100 nm	γ-sources
Americium	50 nm (weak), 10 μm (strong)	γ-sources
Palladium	50 nm	γ-sources
Ceramic	10 μm	γ-sources
Air	5mm	Anywhere else

Table 5.1: *Materials used in the Monte Carlo simulation of the ageing setup. The step size given in the second column is used in the simulation for the interaction of photons. The third column describes where these materials are used.*

in principle with textbook formulae. But these formulae are approximations and do not contain resonance effects due to L-shell or K-shell absorption. Hence experimentally determined absorption coefficients were taken from a database (XCOM) [61]. This online database provides detailed information about all absorption processes for all elements of the periodic table. The properties of mixtures can also be calculated with the database by weighting the different elements in an appropriate ratio.
The materials not only differ in the absolute absorption coefficient. For a given photon energy the dominant interaction process can also be different. In air the photo- and Comptoneffect become equally probable at E$\approx$ 26 keV for instance (Fig. 5.1, left). Since the strong sources emit mainly photons with 60 keV Compton scattering plays an important role in air or gases in general. In brass the situation is completely different. In this material the photoeffect dominates over the whole simulated energy range up to 60 keV (Fig. 5.1 right).

5.2.2 Emission from the sources

There were nine identically constructed irradiation sources in total. Therefore the emission of photons from the sources is simulated in a first step. The output of this simulation consists of two sets (one for each source type of either 1.7 GBq or 500 MBq activity) of distributions for the photon intensities and photon energies in different directions. These distribution were used subsequently for the nine sources in the basic algorithm (section 5.2.3). An important advantage of this modular approach is the possibility to plug other radioactive sources into the Monte Carlo simulation. As an example the weak radioactive source, used for the pulse height scans, was also simulated.
For the simulation of the source emission most parts of the *basic algorithm* were reused. The *basic algorithm* tracks photons until they are converted into electrons

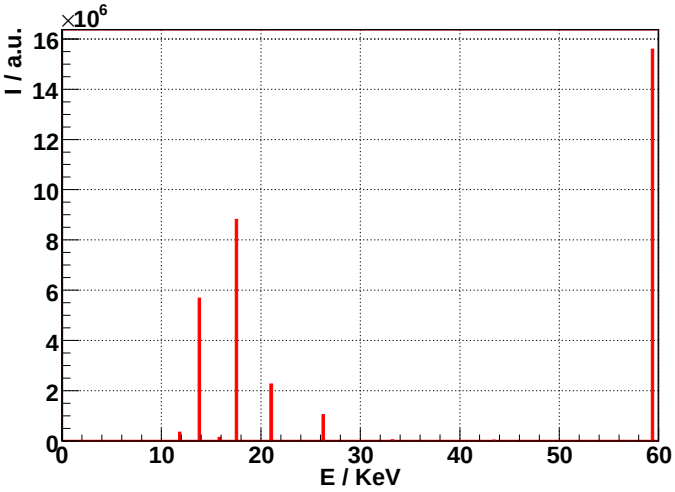

Energy	Intensity	Origin
11.87 keV	0.81%	X-ray
13.93 keV	13.0%	X-ray L_α
15.86 keV	0.33%	X-ray
17.61 keV	20.2%	X-ray L_β
21.0 keV	5.2%	X-ray L_γ
26.34 keV	2.4%	Np*
33.19 keV	0.12%	Np*
43.4 keV	0.07%	Np*
59.5 keV	35.7%	Np*

Figure 5.2: *Emission spectrum of ^{241}Am with energies and intensities of the different lines. The intensities in the table are given with respect to the number of disintegrating ^{241}Am nuclei. They were taken from [58].*

or until they escape. For the simulation of the source emission, photons were tracked from their emission by an americium nuclei in the radioactive compound until they were adsorbed within the stainless steel housing, or until they left the housing. In the latter case their final energy and direction was saved. In order to make this initial simulation step reliable the mechanical layout of the sources had to be known and simulated with high accuracy. Unfortunately this turned out to be the limiting factor in accuracy for the whole simulation (Section 5.3). Anyway many details of the source layout could be a obtained, thanks to [56].

Americium 241 is an isotope of americium with a lifetime of 432.2 years. It decays to almost 100% by emission of an α-particle into an excited state of ^{237}Np. In the de-excitation of the daughter nucleus, photons with distinct energies are emitted only in some cases. In other cases the energy is transferred to an inner electron of the atomic shell (conversion electron). The gap is filled by another electron from the outer shell. Hereupon the energy difference is emitted as an x-ray fluorescence photon denoted as L_α or L_β. The most important photon energies, emitted in succession to a disintegrating ^{241}Am nucleus, are shown in Fig. 5.2 and listed in the table aside. These energies were used in the simulation.

Strong sources: The construction of the strong sources used for the irradiation in the ageing experiments can be found in Fig. 5.3 together with the simulated emission probability for different directions θ and ϕ. The sources are constructed such, that americium nuclei are incorporated in a ceramic bead [56] with a diameter of 3 mm (sources with an activity of 1.7 GBq) or 2 mm (0.5 GBq activity). The parameters used for the simulation of the strong sources are shown in Tab. 5.2. The ceramic bead is covered by a cylindrical stainless steel housing (see Fig. 5.3 left). Hence the emission spectrum is not totally spherical symmetric. Moreover the

Content activity	1665 MBq	518 MBq
content m (AmO_2)	14.96 mg	4.65 mg
ρ (AmO_2)	11.68 gcm^{-3}	
ρ (ceramic)	2.6 gcm^{-3}	
thickness front window	225 μm	
diameter ceramic bead (housing)	3 (4) mm	2 (3) mm
A_{out} (4π)	168.1 MBq	63.1 MBq
A_{out} forward	17.4 (18) $\cdot 10^6/(s \cdot sr)$	6.69 (7) $\cdot 10^6/(s \cdot sr)$

Table 5.2: *Parameters used to simulate the strong sources. The activity per steradian given in the last line denotes the simulated output of photons with an energy of* 59.5 *keV in a* 30° *cone through the front window. The value in brackets is given by the manufacturer as typical output of pl*

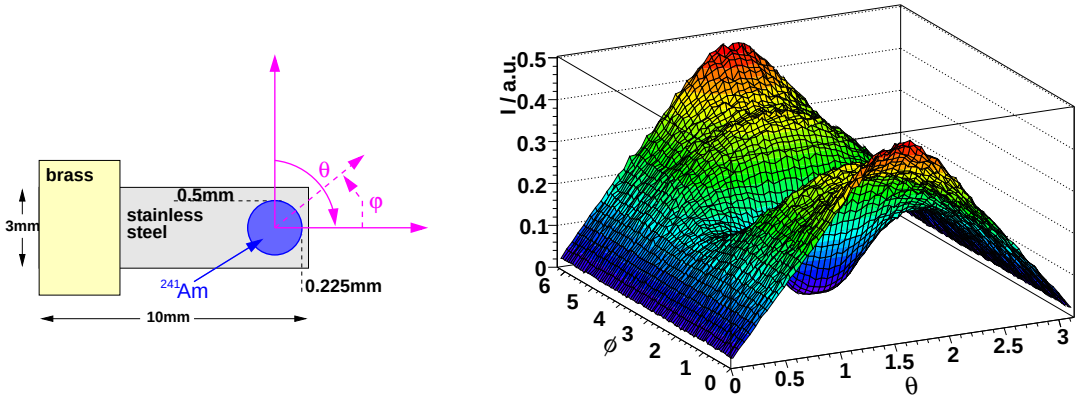

Figure 5.3: **Left:** *Layout of the strong* ^{241}*Am sources with its housing (from [57] and [56]) and definition of the angles* θ *and* ϕ *used throughout the MC.* **Right:** *Emission intensity* I *as a function of* θ *and* ϕ*. Photons with* $\phi \approx \pi$ *and* $\theta \approx \pi/2$ *fly in the direction of the brass holding. Hence their intensity is rather low there. Contrary for photons with* $\phi \approx 0(2\pi)$ *it is very probable to leave the source. The simulation was performed in intervals of* 3° *in* θ *and* 4° *in* ϕ *for* 10^8 *photons.*

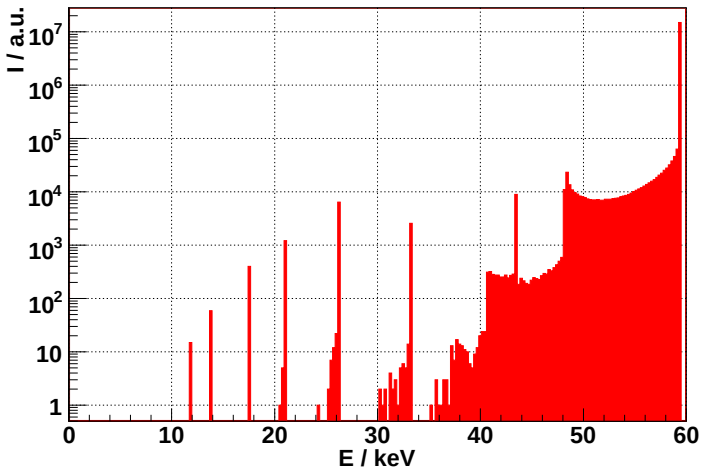

Figure 5.4: *Emission spectrum of a strong source after taking into account absorption and scattering processes within the ceramic bead and the source housing. Two facts are important: Photons with* $E \leq 30$ *keV are almost completely absorbed (logarithmic scale, compare with Fig. 5.2). Further each emission line from Fig. 5.2 has a tail to lower energies due to Compton scattering processes.*

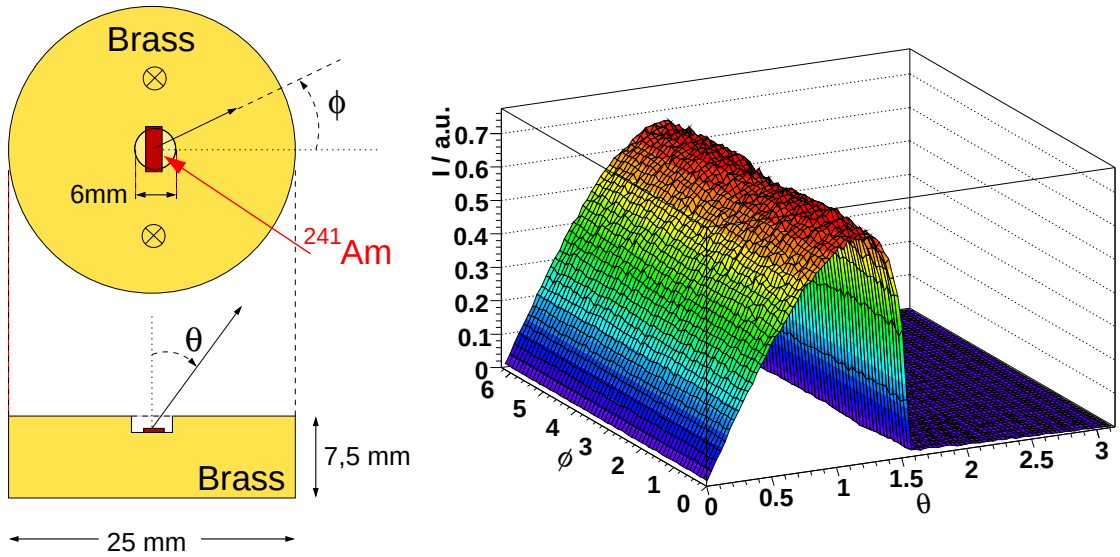

Figure 5.5: **Left:** *Layout of the housing for the weak* ^{241}Am *source. A picture (with the collimator on top) can be found in Fig. 4.4.* **Right:** *Resulting emission probability P for* θ *and* ϕ*. The symmetry in* ϕ *is due the radial shape of the source housing. This probability distribution was used as input for the basic algorithm of the simulation.*

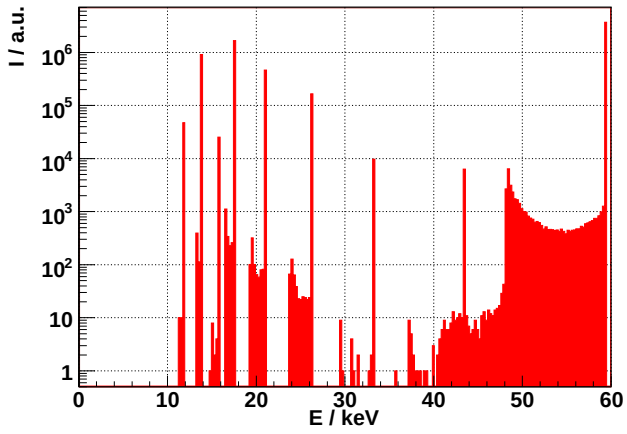

Figure 5.6: *Emission spectrum of the weak source: In contrast to the emission spectrum of the strong sources (Fig. 5.4) now also photons with lower energies can escape from the americium-gold matrix. The spectrum was simulated with a pure palladium layer as cover of the americium-gold matrix; this was the default setting.*

energies and directions of the emitted photons are changed by self adsorption and Compton scattering processes. All this has been included in the source simulation and leads to the emission energy spectrum shown in Fig. 5.4.

Weak source: The housing of the weak source is composed of brass and was manufactured in the mechanical workshop of the institute. The active part of the weak source is a gold matrix with embedded americium nuclei [56], covered by a thin layer of 2 μm thickness. This covering layer is made of palladium or an alloy of palladium and gold [57]; the exact composition could not be determined. To assure mechanical stability these layers are rolled on top of a silver foil with 175 to 200 μm thickness. The layout of the housing and the resulting emission probabilities as a

function of emission angles θ and ϕ are shown in Fig. 5.5. Since the layer on top of the americium-gold matrix is very thin, this source also emits photons with lower energies than 59.5 keV and α-particles[1]. The resulting emission spectrum is shown in Fig. 5.6.

5.2.3 *Basic algorithm* - Tracking photons

Given a photon with energy E_γ and direction of flight θ, ϕ (spherical coordinates), the simulation starts on a sphere with a radius R of the source housing (the scattering processes within the source housing are already simulated). The start coordinates are:

$$\vec{x}_i = R \cdot (\sin\theta\cos\phi, \sin\theta\sin\phi, \cos\theta) \tag{5.1}$$

At the beginning of a track the angles θ and ϕ are drawn randomly from the intensity distributions obtained with the simulation of the sources (Section 5.2.2). The energy E is drawn subsequently from the energy distribution corresponding to the emission angles θ and ϕ.

Simulation step: From a mechanical description of the experimental setup the material, surrounding the photon at its current position $\vec{x}_i$, is retrieved. According to the second column of table 5.1 the photon moves outwards in direction θ, ϕ by the step size s:

$$\vec{x}_{i+1} = \vec{x}_i + s \cdot (\sin\theta\cos\phi, \sin\theta\sin\phi, \cos\theta) \tag{5.2}$$

Absorption: The intensity of a photon beam after an absorber with thickness d, matter density ρ and photo absorption coefficient σ is

$$I(d) = I_0 \cdot e^{-\sigma\rho d} = I_0 \cdot P_{pass} \tag{5.3}$$

with the probability P_{pass} to pass the absorber. The absorption coefficient σ in Eq. 5.3 is taken from [61] and includes both, the photoelectric effect and Compton scattering. The probability for a photon to be absorbed during this simulation step (with length s) is given by:

$$P_{abs} = 1 - P_{pass} = 1 - e^{-\sigma\rho s} \tag{5.4}$$

A random number $t \in [0;1]$ is drawn and compared to P_{abs}. If $t \leq P_{abs}$ the photon is absorbed. If $t > P_{abs}$ the photon is not absorbed and consequently the simulation goes on with the next simulation step.

Type of absorption: With another random number it is decided whether the photo absorption effect or a scattering effect were the reason for the absorption. This is done according to their relative contribution to the total absorption cross-section.

[1] The α-particles can not enter the drift tubes. Hence they were ignored in the simulation.

- In case the photoelectric effect was selected, the photon track ends at this position. If the actual position of the photon is within a drift tube, the electron tracking procedure is started. The energy of the liberated electron is determined taking into account the relative contributions of K- and L-shell absorption. In the following the excited atom emits either an auger-electron or a x-ray fluorescence photon. The relative contribution of these two processes were taken from [62]. Auger electrons were tracked with the electron tracker, x-rays were followed with the basic algorithm.

- For low energies ($E < 15$ keV, see also Fig. 5.1 left) the elastic Thompson scattering plays an important role. Then the energy of the photon is left unchanged, but the direction of flight is modified such, that the photon is re-emitted isotropically from the place were it was absorbed.

- In case the Compton effect was selected with the random number, the photon gets a new direction of flight, calculated according to

$$P(\theta_2) = 1 + \cos(\theta_2)^2 \tag{5.5}$$

where θ_2 is counted from the actual direction of flight. In addition part of the photon energy Eγ is transferred to an electron in a scattering process.

$$E_e = E_\gamma \cdot \left(1 - \frac{1}{1 + \gamma \cdot (1 - \cos\theta_2)}\right) \tag{5.6}$$

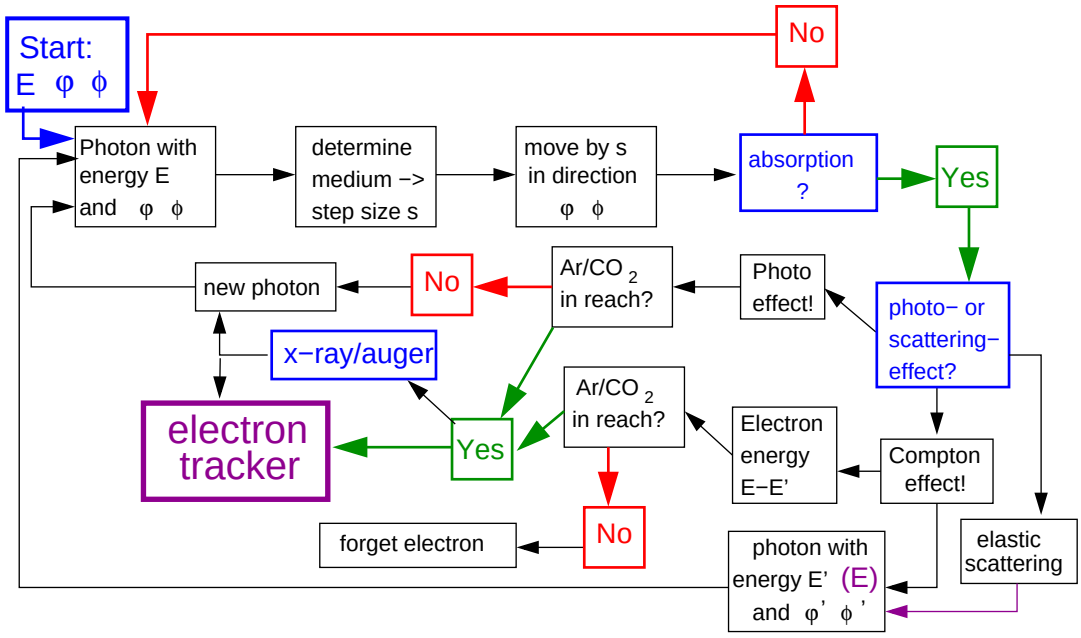

Figure 5.7: *Flowchart of the basic algorithm. The algorithm starts with the blue box in the upper left corner. All blue boxes denote decision where a random generator was used.*

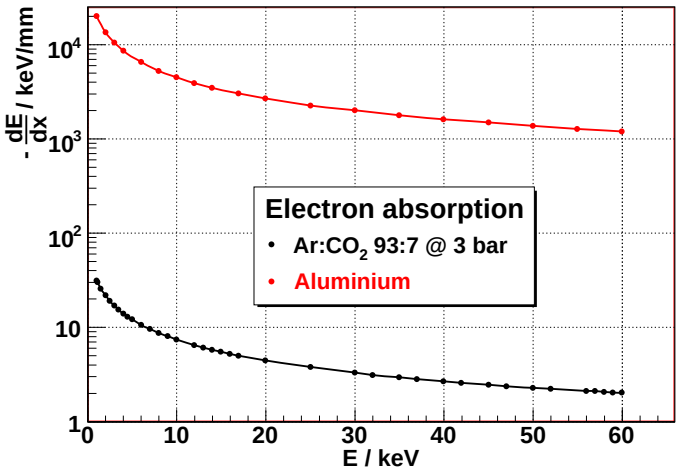

Figure 5.8: *Electron stopping power $-dE/dx$ in aluminium and Ar:CO_2 93 : 7 for different electron energies E_e. The data points are extracted from the ESTAR database [59].*

with $\gamma = E_\gamma / m_e c^2$ as in Eq. 2.6. The liberated electron with kinetic energy E_e is then passed to the electron tracking procedure if it was created within a drift tube. In case the scattering happened outside a drift tube, only the photon is tracked further.[2]

The whole algorithm is merged to the flowchart Fig. 5.7.

5.2.4 The electron tracking procedure

When the electron tracking procedure is called, a photon has liberated an electron with energy E_e in a photoabsorption or scattering process inside the drift tube or within the tube wall. To calculate the path of the electron the stopping power of the material (aluminium or Ar:CO_2) has to be known for different energies. These values were taken from another database [59]. An example is shown in Fig. 5.8. The electron is subsequently slowed down thereby ionizing the medium. Depending on the medium (aluminium or Ar:CO_2) a different method is applied:

Aluminium: If the electron is still in the tube wall, the step size s to calculate the energy loss is set in every step to half of the remaining distance to the inside of the tube (with a minimum of 1 μm). The energy loss along s is calculated with

$$\Delta E = \frac{dE(E_e)}{dx} \cdot s \tag{5.7}$$

and subtracted from the electron energy. In aluminium the liberated electrons recombine quickly with the ions, so that no separated charges are generated in this case. If the primary electron is created close enough to the inside, it can reach the gas in the drift tube with kinetic energy left.

[2] A photon with an energy of 60 keV can impart maximum 12 keV to an electron in a Compton scattering process. The mean free path for an electron with 12 keV is only about 5μm in aluminium (green line in Fig. 5.8). Thus the probability for an electron to reach the inside is vanishingly small.

Clustering in Ar:CO_2: If the primary electron is inside the drift tube it creates clusters of electrons and ions which are further separated by the electrical field. As an approximation of the differential energy loss $\delta E/l$, the energy loss δE of the electron along a path of length $l = 10$ μm is calculated with Eq. 5.7. Now the free path s is calculated to

$$s = l \cdot \bar{N}_c \cdot \frac{\bar{E}_{ion}}{\delta E} \tag{5.8}$$

where $\bar{E}_{ion}$ is the mean ionisation of argon and $\bar{N}_c$ is the mean cluster size. The energy loss $\Delta E = \bar{N}_c \cdot \bar{E}_{ion}$ along the free path s is subtracted from the electron energy[3] E_e. In this simulation step i a random cluster size n_i is taken from the cluster size distribution shown in Fig. 2.4.
With decreasing energy of the primary electron the stopping power rises and hence the cluster density of liberated electrons increases. In the end N clusters with a total number of $N_e = \sum_i^N n_i$ free electron have been created. In the vicinity of the wire $M_j \cdot \bar{G}$ $(j = 1 \ldots N_e)$ free electrons are created by gas amplification. $\bar{G}$ is the mean gas amplification factor; the numbers M_j follow a Polya-distribution. Thus a total charge of

$$Q = \sum_{j=1}^{N_e} M_j \cdot G \cdot 1.6 \times 10^{-19}\mathrm{C} \tag{5.9}$$

is deposited on the wire for this track. Since the clustering is done in steps, the charges of the single clusters are attributed to the correct positions along the tube. This is important for the calculation of local current and irradiation densities. The drift times t_i of each cluster to the wire is determined with a polynomial r(t) relation, as shown in Fig. 2.6. The drift times are then written to a file for later usage (Section 5.4.1).

5.3 Limitations

Before comparing the Monte Carlo to data, the limitations of the simulation have to be discussed. All information about the sources was retrieved from schematic drawings and [56], but still some uncertainties remained. They are explained separately for the strong and for the weak source.

Strong sources:

Fig. 5.9 shows the measured counting rates of all sources as a function of the x-coordinate of the radioactive source. These counting rates were measured at the same y-position of the component test to minimize uncertainties. Further, the measurements were performed with the same drift tube and readout electronics. As a comparison the predictions from the MC simulation are also shown in Fig. 5.9.

[3] Actually the real energy loss in every step i fluctuates according to a landau distribution. But if the total energy loss is in the same order as the energy of the particle, the landau distribution merges into a Gaussian. Since most electrons are stopped in the tube this condition is fulfilled.

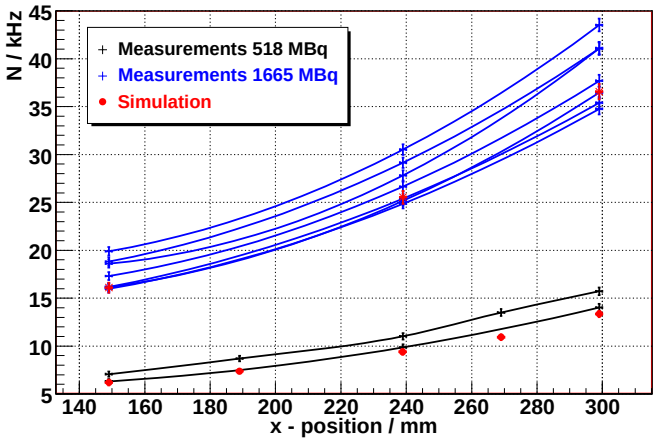

Figure 5.9: *Counting rates as measured with the* component test *(black:* 1.7 *GBq, blue:* 500 *MBq) in comparison with the predictions (in red) from the Monte Carlo simulation (without space charge effects) for different distances from the sources to a drift tube. The model reproduces the progression correctly.*

A huge variation of the counting rates initiated by individual sources is measured, although the sources were manufactured in the same way. One reason is given by different nominal content activities, which can vary by ±10% [50]. According to [56] these variations are due to inhomogeneities of the radioactive americium oxide compound within the ceramic bead. Further differences in the emitted radiation distribution of individual sources could be caused by small variations in the thickness of the stainless steel housing. In particular this results in a different progression of the counting rate with the distance to the source. This can be seen clearly in Fig. 5.9 for some of the stronger sources. The average progression of the counting rate is modelled really good by the Monte Carlo. Hence the absolute photon output of the individual sources was scaled in the MC to fit to the measured data. To simulate the output of each source with a higher precision is not possible. In order to do that, the inner dimensions and the exact composition of each source is required. In particular the inner diameter of the stainless steel housing and the outer diameter, shape and composition of the ceramic bead are needed. These information is not available.

Weak source:

The construction plans of the weak source are very detailed. The only uncertainty is the composition of the 2 μm layer, covering the americium-gold matrix. Hence the simulation was performed with two different settings. Besides a foil composed of 100% Pd an alloy of Pd:Au 75 : 25 was tried. By doing so the output activity of the weak source changes from 194 kBq (100% Pd) to 177 kBq (Pd:Au 75 : 25). However, the amount of 25% of gold in the alloy is an arbitrary number. It is merely thought as an example to illustrate the impact on the absolute counting rate. The manufacturer also gives an uncertainty of ±10% on the nominal content activity of the foil, which is of the same order.

5.4 Comparison to data and predictions

In this section the output of Monte Carlo simulation is compared to available data. Further some predictions are shown and explanations, which are only accessible on Monte Carlo level, are given.

5.4.1 Counting rate, trigger efficiency

To allow an estimation of the counting rate, the information about the drift times of the individual clusters is needed. These information was available in the electron tracking procedure (see Section 5.2.4) and was saved to files. Furthermore details about the readout electronics and the amplifier are required. In Appendix B the impact of these electronic circuits is described in terms of a transfer function $\Psi(\omega)$. For each signal generated by a photon track, a raw pulse shape $I(t)$ is calculated with Ramo's theorem (see Sections 2.2.2 and 2.2.3). The progression of the pulse shape is transformed into the frequency domain via Fourier transformation[4]

$$\tilde{I}(\omega) = \frac{1}{\sqrt{2\pi}} \cdot \int_0^T e^{-i\omega t} I(t) dt \tag{5.10}$$

Now the Fourier transformed current $\tilde{I}(\omega)$ is multiplied with the transfer function $\Psi(\omega)$:

$$\tilde{I}_2(\omega) = \tilde{I}(\omega) \cdot \Psi(\omega) \tag{5.11}$$

Finally the modified current in the frequency domain is inversely Fourier transformed to arrive at the correct progression of the induced current (the pulse shape):

$$I_2(t) = \frac{1}{\sqrt{2\pi}} \cdot \int_0^T e^{i\omega t} \tilde{I}_2(\omega) d\omega \tag{5.12}$$

With an amplifier gain of 50 mV per μA [40] the voltage after the amplifier can be calculated and compared with the trigger threshold of the discriminator (section 4.1.3). Thus the number of triggering signals N_{trig} (from a total number N_{tot} of interacting photons) can be estimated. To compare the simulation with measured counting rates, the activity A of the radioactive source is needed. If the Monte Carlo generated N_γ photons in total, the counting rate predicted by the simulation is:

$$R_{MC} = \frac{N_{trig}}{N_{tot}} \frac{A}{N_\gamma} = \epsilon \cdot \frac{A}{N_\gamma} \tag{5.13}$$

where ϵ is called the trigger efficiency. The value of ϵ is different for the two types of radioactive sources:
The strong sources emit mainly photons with $E = 60$ keV. These photons interact with gas molecules predominantly via Compton scattering processes (Fig. 5.1, left). The energy of the scattered electrons can be close to zero and thus the amount of separated charges in the tube. These signals do not reach the trigger threshold, thus

[4] For the simulation discrete Fourier transformation is used.

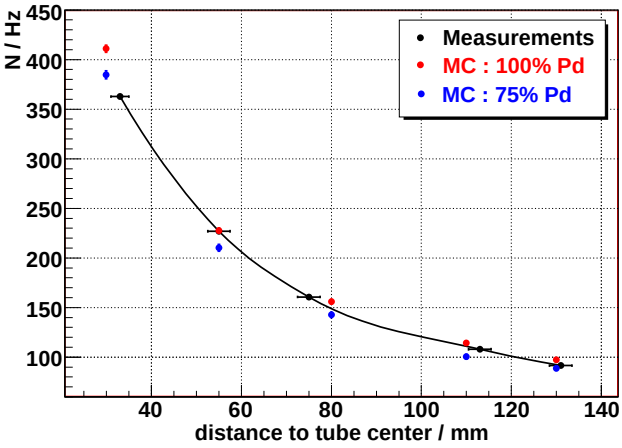

Figure 5.10: *Counting rates as measured with the component test (in black) in comparison with the predictions from the Monte Carlo simulation for different distances between source and drift tube. The simulated points in red correspond to a cover layer of* 100% *Pd, the points in blue to an alloy of* 75% *Pd and* 25% *Au.*

ϵ_{strong} is relatively small.
The weak source emits also photons with an energy around $E = 16$ keV. In gases the photo effect is dominant at these energies. Hence the energies of the liberated electrons are higher and thus the amount of separated charges. For the weak source the contributions from Compton scattering are low, so that almost all signals reach the voltage needed to trigger the read out. The following trigger efficiencies were determined:

$$\epsilon_{weak} = 96.4 \pm 0.2\% \qquad \text{and} \qquad \epsilon_{strong} = 83.5 \pm 0.5\% \tag{5.14}$$

The uncertainties in Eq. 5.14 were calculated from the simulation assuming Poisson statistics.
A comparison of the simulated and measured counting rate for the weak source is shown in Fig. 5.10 for two different setups of the cover layer. The simulation with a pure Pd foil describes the measured data more accurately and is therefore used in subsequent simulations.

Space charge effects: The comparison of the strong sources and the Monte Carlo is shown in Fig. 5.9. By looking closer at this plot it can be seen that the Monte Carlo fits better for higher counting rates, in particular for the sources with an activity of 1.7 GBq. The reason are space charge effects (see Section 2.2.3), which reduce the measured counting rate. Up to now the Monte Carlo does not include space charge effects. To account for these effects the trigger efficiency ϵ must be changed in the Monte Carlo, as a function of the local irradiation rate. Note that the irradiation rate, or the rate of photons interacting with a drift tubes, is not affected from space charge effects.
A similar correction procedure is also done for the current density in subsection 5.4.3; there the correction procedure for the trigger rate is also explained. The resulting counting rates, including space charge effects, are listed in the Appendix A.

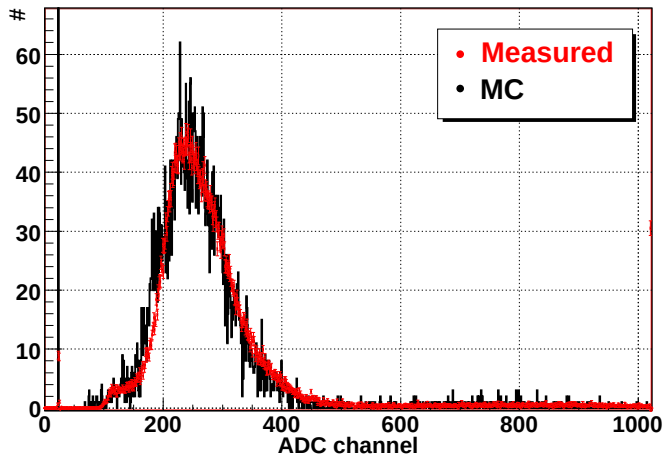

Figure 5.11: *Simulated (black) and measured (red) pulse height spectra for the weak source. For the comparison the two spectra were scaled to an equal number of entries in the histograms. The trigger level, the peak position and the rising and falling slopes of the peak are modelled very well by the Monte Carlo.*

5.4.2 Pulse height spectra

For the comparison of the measured energy spectrum with a simulated one, further knowledge about the progression and procession of the signals is needed:

- After the amplifier the signal is split (trigger logic and ADC, see section 4.1.3), delayed and attenuated to adapt for the ADC input.
- The delay between trigger and ADC signal is such, that the ADC gate opens 40 ns before the signal reaches the required trigger threshold.
- The gate of the ADC is open for 500 ns. During this time only part of the separated charges have been accumulated in the ADC.
- The ADC has a linear scale with a maximum of 12.8 nVs (equivalent to 1024 channels).

Taking all this into account, one can calculate the expected ADC channel number from the Monte Carlo simulation. This has been done for both types of radioactive sources. A comparison of a simulated spectrum with a measured spectrum from the weak source is shown in Fig. 5.11; for the comparison with the spectrum of the strong sources see Fig. 5.12.
In particular the consistency obtained for the weak source is remarkable. In case of the strong source the shape of the spectrum is predicted with minor flaws. But the mean pulse height of the measured spectrum (505 ADC channels) and the simulated spectrum (509 ADC channels) agree within 1%. Additionally the trigger level in ADC counts is predicted correctly. Thus the goals of the Monte Carlo, namely the prediction of irradiation densities, current densities and trigger rates was achieved.

5.4.3 Current

The current measured in a drift tube can also be compared to the Monte Carlo prediction. For a number N_γ of simulated photons in the Monte Carlo, the current

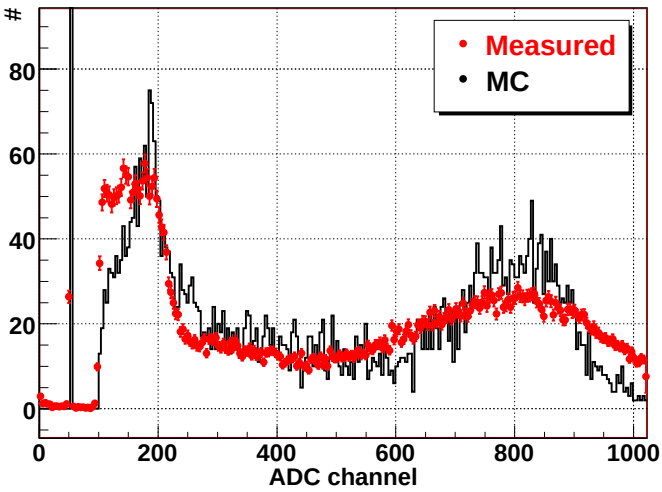

Figure 5.12: *Simulated (black) and measured (red) pulse height spectra for the strong source. For the comparison the two spectra were scaled to an equal number of entries in the histograms. The two distributions do not agree in detail. But the key features, such as mean pulse height and trigger level, are reproduced correctly.*

in a tube i is estimated to

$$I^{(i)} = \frac{A}{N_\gamma} \cdot \sum_{j=1}^{N} Q_j^{(i)} \tag{5.15}$$

where A is the activity of the simulated radioactive source and $Q_j^{(i)}$ all charges deposited on the wire, calculated according to Eq. 5.9. But equation Eq. 5.15 is only correct for rather low irradiation rates. At trigger rates above 500 Hz/cm the local gas gain drops by more than 5% due to space charge effects and with it the current in the drift tubes. Consequently the following procedure is performed to account for gas gain reductions due to space charge effects:

- From the simulation the overall irradiation rates N_i were determined for each tube i. They are independent from space charge effects.
- The raw current density distribution $I_i(y)$ (without space charge effects) along the tubes is used to calculate local irradiation densities $N_i(y)$ with the constraint $\int N_i(y)dy = N_i$. The raw current density is known from the electron tracking procedure (Section 5.2.4).
- The local gas gain reduction factor $\delta_i(y)$ is calculated according to the measurements shown in Fig. 2.10.
- Multiplying $I_i(y)$ with $\delta_i(y)$ yields an approximation of the real current density (and thus the real current).
- With the local factor $\delta_i(y)$ and the absolute trigger threshold C_{trig} an effective local trigger level $C_{eff}(y) = C_{trig}/\delta_i(y)$ is determined. The local trigger rate $N_{trig}(y)$ is the number of pulses with a pulse height $C > C_{eff}(y)$. The local counting rate integrated over the whole tube yields the real trigger rate $N_{real} = \int N_{trig}(y)dy$.

This procedure was checked for several source arrangements and with partly shielded tubes. The simulated currents at 3080 V agree with measured values of the current

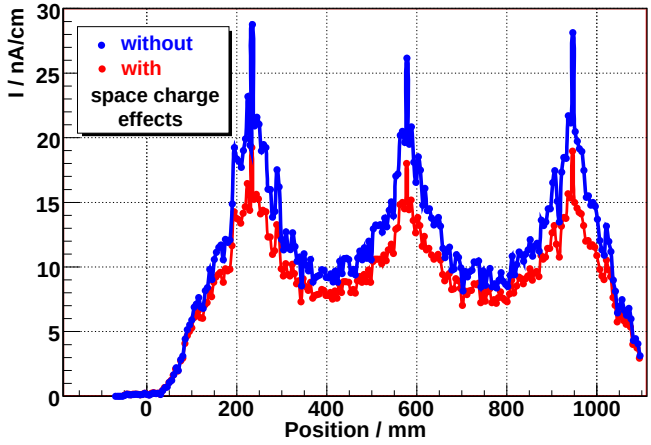

Figure 5.13: *Impact of space charge effects on the current density at $U = 3080$ V (mean gas gain $G = 2 \cdot 10^4$): The distribution along the tube becomes less pronounced. At higher operating voltages the impact of these effects will be even higher.*

within 5%. The results can be found in the Appendix A.
To illustrate the impact of space charges the current density distribution is shown with and without space charge effects in Fig. 5.13. For this drift tube the peak current density is reduced from 29 nA/cm to 20 nA/cm. The current density in the less irradiated regions changes only from 10 nA/cm to 8.5 nA/cm.

Remark: The simulation was performed for an operating voltage of 3080 V. Many important measurements were carried out with this operating voltage and could thus be used as input for the simulation. These were in particular the absolute value of the gas gain and the measurement of the gain loss due to space charge effects. The drift tubes in the ageing tests were operated at 3500 V most of the time. With this operating voltage space charge effects become even more important. The current density distribution along the tube is then even less pronounced.

5.4.4 Scanning width

For the pulse height scans a collimator was used to constrain the scanned section on a tube. From simple geometrical consideration one would expect a range of 2.9 ± 0.1

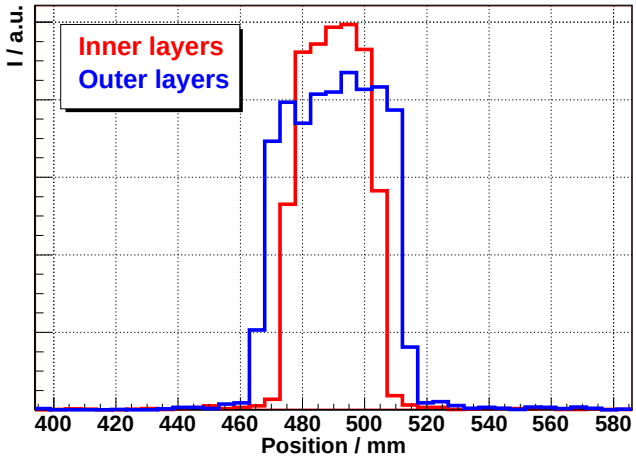

Figure 5.14: *Length of the scanned section along the tube in pulse heigh scans as result of the MC simulation. For the tubes in the inner (outer) two layers a length of ≈ 3 (4.5) cm is retrieved. This is in good agreement with a simple geometrical estimation.*

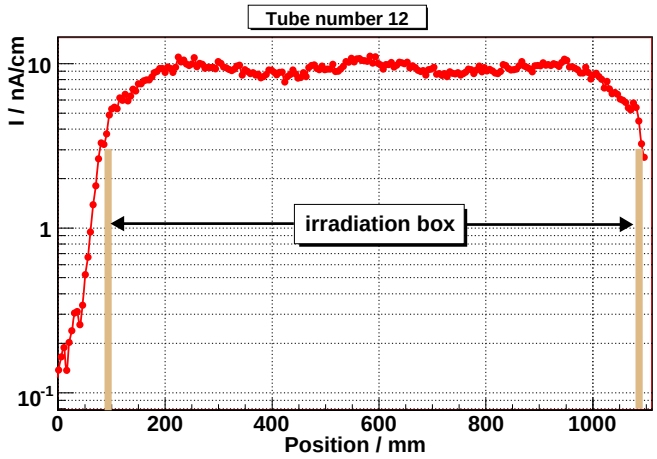

Figure 5.15: *Current densities along an arbitrary drift tube (here number 12). In the reference zone, where* $0 < x < 40$ *mm, still current densities of the order* $0.1 - 0.3$ *nA/cm were reached. The positions given on the x-axis are identical with those in the pulse height scans.*

cm for the tubes of the two inner layers, respectively 4.3 ± 0.2 cm for the tubes of the outer two layers. For this estimation the tubes were treated as if they were mounted at 8 (12) cm distance to the source without any extension in direction towards the source. Further it was not clear how scattering effects in the brass collimator affect the spread of the scanned range. The Monte Carlo simulation provided an answer to these questions as shown in Fig. 5.14: The geometrical estimation is sufficient.

5.4.5 Reference zone

On the outside of the irradiation box each tube has an unirradiated range that serves as a reference. Nevertheless photons can escape the irradiation box through the drift tubes[5]. Thus the ionisation of argon atoms in the reference zone is possible. In Fig. 5.15 the current density distribution in the reference zone, as predicted by the MC simulation, is shown: Current densities between 0.1 and 0.3 nA/cm are expected in the reference zone for an operating voltage of 3080 V. At higher voltages (for the component tests 3500 V were applied) the current densities is higher, in particular because the irradiation rate in the reference zone is well below 500 Hz/cm. Thus the impact of space charge effects is negligible.

5.5 α-source

For the ageing experiment with an α-source a rather simple Monte Carlo simulation was set up: As a starting point an isotropic emission of α-particles from the thin foil source is assumed. The kinetic energy of the α-particles is taken randomly from a Gaussian distribution with a mean of 4 MeV and a width of 0.3 MeV [57]. Then the α-particle is successively slowed down in Ar:CO_2 or aluminium, depending on its position. The stopping power is calculated with data taken from another database (ASTAR) [60]. If the medium surrounding the α-particle is Ar:CO_2 and the position is within the outer tube radius (as in Fig. 5.16 left), the electrons, liberated through

[5] Therefore the lead shieldings were mounted around the brass box, see 4.1.1

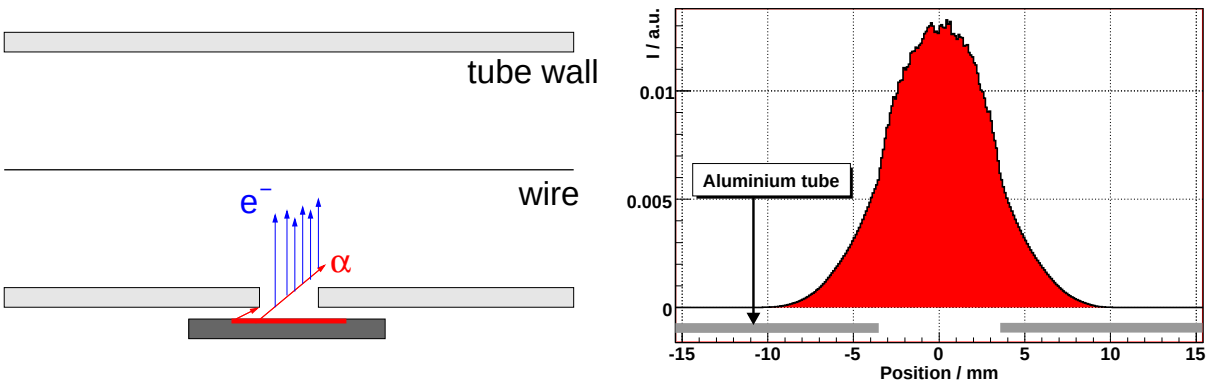

Figure 5.16: *Geometrical simulation of the drift tube irradiation with α-particles. Almost* 91% *of liberated electrons reach the wire on a length of* 1 *cm. All separated charges are accumulated within* 2 *cm.*

collisions with the α-particle, can reach the wire of the drift tube. These electrons were then attributed to a position along the wire perpendicular to the position where they had been liberated. With this procedure the number of electrons on the drift tube wire, as shown in Fig. 5.16 (right), could be retrieved: 90.7% of the electrons reach the wire within a length of 1 cm. All electrons are produced within 2 cm.

Chapter 6

Ageing results

In this chapter the results of the ageing tests carried out in Freiburg between July 2004 and November 2007 are presented. The first section 6.1 gives a short overview of the important observables used to classify ageing effects. In the next section 6.2 the analysis of the pulse height scans as the most sensitive method is illustrated. Section 6.3 defines ageing by means of well defined observables. In the sections 6.4 and 6.5 the results of the ageing studies performed with the component test are shown. Finally, the results obtained for the ageing experiment with an α-source are presented in section 6.6.

6.1 Observables

Pulse height: As pointed out in section 2.4 and measured in the previous experiments in Freiburg and at CERN (Chapter 3), ageing manifests itself in a reduction of the signal pulse height, caused by a reduction of the gas gain in the drift tube. If $Q_{ADC}(E, y)$ denotes the measured charge (in a pulse height scan) of a single particle with energy E at position y, the following relation holds:

$$Q_{ADC}(E, y) = N_{prim}(E) \cdot e^{-} \cdot G(y) \cdot \epsilon_{El}(E). \tag{6.1}$$

where $N_{prim}(E)$ is the number of primary electrons and ions, e^{-} the unit charge and $G(y)$ the gas gain at position y. The factor $\epsilon_{El}(E)$ characterizes the impact of the readout electronics, such as the duration of an ADC gate signal or the trigger level of a discriminator. The importance of Eq. 6.1 lies in the fact that the gas gain G is measured locally. Since G depends on the gas density ρ and thus on temperature T and pressure p, the pulse height is also the most sensitive observable with respect to impacts from these environmental conditions. Consequently it is described in more detail in section 6.2.

Current: The gas gain G is a local quantity in the sense that it can vary along the tube. The current measures merely:

$$I = \frac{d\Big(N_{prim}(t) \cdot e^{-} \cdot \bar{G} \cdot \Big)}{dt} = Z_{int} \cdot \bar{N}_{prim} \cdot e^{-} \cdot \bar{G} \tag{6.2}$$

with an average gas gain $\bar{G}$ of the whole tube. Z_{int} denotes the interaction rate[1] of photons and drift tube. Hence the current is also a good observable in an ageing experiment, albeit not as a local observable. But when the current in the drift tube is created locally, for instance with a collimated source or an α-source, it should become comparable with a pulse height scan.
Nevertheless, it can not be stated, that the value of a measured current always decreases, when ageing effects occur. For instance the *Malter effect* ([27], [28], [29]) causes a permanently higher current in the affected drift tube. Ageing effects are therefore merely detected when the value of the current changes unexpectedly.

Counting rate: For the counting rate it is not possible to give an analytical formula, because a trigger condition of a discriminator has to be included. Nevertheless, with a reduced pulse height also the number of counts above the trigger threshold decreases. As in the case of the current, there are other effects related to ageing that can increase the counting rate. Hence ageing effects are likely if the counting rate changes suddenly for no apparent reason.

6.2 Pulse height

In the following, the methods used to determine a measure for the pulse height are presented. Furthermore, required corrections and systematic errors are discussed.

6.2.1 Measures of the pulse height

When performing pulse height scans the photo peak of photons with an energy around 16 keV is clearly visible in the spectrum. First measurements showed that

[1] whereas the counting rate includes only pulses with a minimum voltage

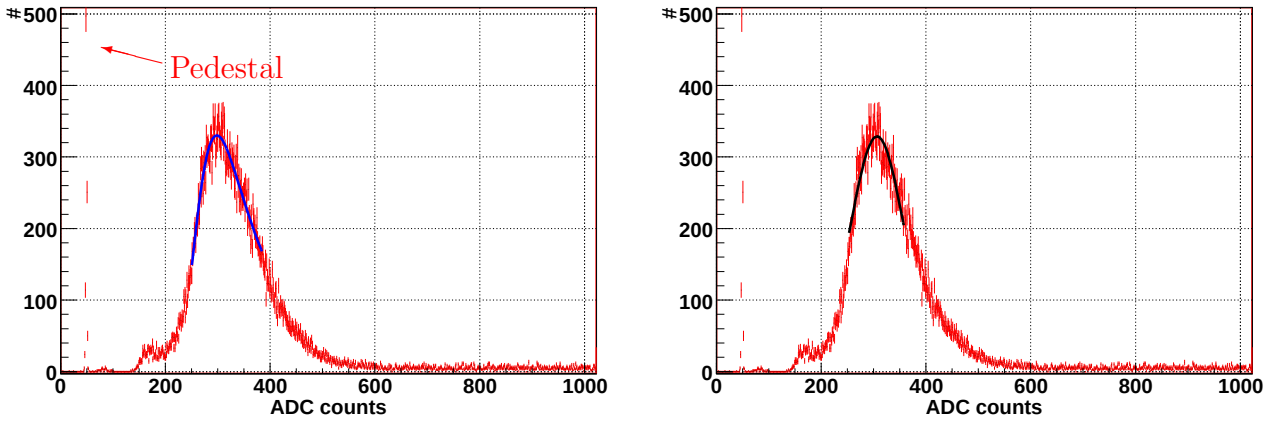

Figure 6.1: *Example of a measured pulse height distribution (red). In the left figure a landau distribution (blue) was fitted to data. In the right figure a fit with a Gaussian distribution (black) is shown.*

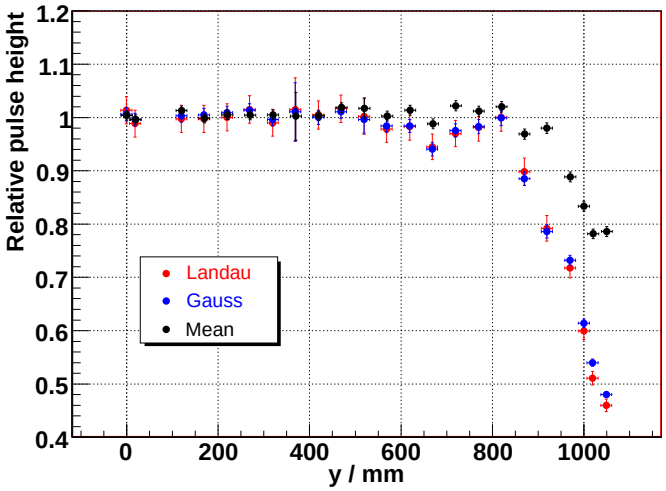

Figure 6.2: *Pulse heights along a single drift tube as determined with the different methods: The two fit methods (with a Landau or a Gaussian distribution) are the more sensitive approaches. In this plot relative pulse heights, as defined in Section 6.2.3, are shown.*

the peak has the shape of a Landau distribution, at least around the position of the maximum, see Fig. 6.1. Consequently the most probable value of the spectrum was fitted with a Landau distribution:

$$N(C) = A \cdot exp^{-0.5\cdot(\lambda(C)+e^{-\lambda(C)})} \quad \text{with} \quad \lambda(C) = \frac{C - C_{mp}}{\sigma}$$

where C_{mp} is the most probable value (in ADC counts) of a Landau distribution and σ the width. Together with the value of A they were free parameters in the fit. The Landau fit is a good method to measure the pulse height. To compare and contrast with other methods a fit with a Gaussian distribution, centred at C_c, was performed (Fig. 6.1, right). Additionally the mean pulse height C_{mean} in an interval $[C_{start} : C_{stop}]$ around the maximum of the pulse height distribution was calculated.

Definition of pulse height: For all three methods the pedestal of the spectrum was fitted separately with a Gaussian distribution. The mean value of the pedestal C_{ped} was subtracted from the values C_{mp}, C_c and C_{mean} to define an absolute value of the pulse height. In the following this absolute value is called C_i, where i represents a number for the position along a drift tube, where the pulse height scan was performed. For simplicity the three different methods to determine the absolute pulse heights C_i are not distinguished in the remainder of this chapter.

Benchmarks: While the fit methods rely on a correctly estimated fit range the mean value is robust and works even for badly measured spectra. In Fig. 6.2 the three methods are compared. They show compatible results with the fit methods being more sensitive to ageing. The sensitivity of the mean value can be increased when the range of $[C_{start} : C_{stop}]$ is restricted to a range around the peak of the pulse height distribution. Some of its robustness is lost this way, since the correct range around the maximum has to be found with the same procedures as for the fitting methods.
The fit with a Landau distribution was used as default procedure. Only in rare

cases, when the pulse height spectrum was totally degenerated, the mean value of the pulse height was taken.

6.2.2 Corrections

As can be seen in the Appendix B, the transfer function is independent from the position along the drift tube, where the signal was generated. Hence corrections to compensate for signal attenuation were not necessary.
Comparing the measured pulse heights in the irradiated region with the pulse heights measured outside the irradiation box (reference zone) all differences due to the electronic circuits cancel.
An important remaining source of errors is a change of the operation and environmental parameters (pressure, temperature and voltage) during the pulse height scan. A pulse height scan lasts 2 hours per drift tube at the maximum. The environmental parameters were monitored by the slow control system (Section 4.1.4) during the scan.

Temperature and pressure correction: The ageing experiment was set up in a laboratory equipped with an air conditioning system. The temperature variation as measured by the temperature sensors installed within the irradiation box is shown in Fig. 6.3. During the time of a pulse height scan the temperature never changed by more than 0.5 K. Over a day maximum variations of about 2 K were reached. The impact of temperature and pressure changes on the signal pulse height can be estimated by simplifying the Diethorn formula (Eq. 2.10) with two parameters A and B. The gas gain G as a function of the gas density ρ can be expressed as:

$$G(\rho) = \left(\frac{A}{\rho}\right)^B \tag{6.3}$$

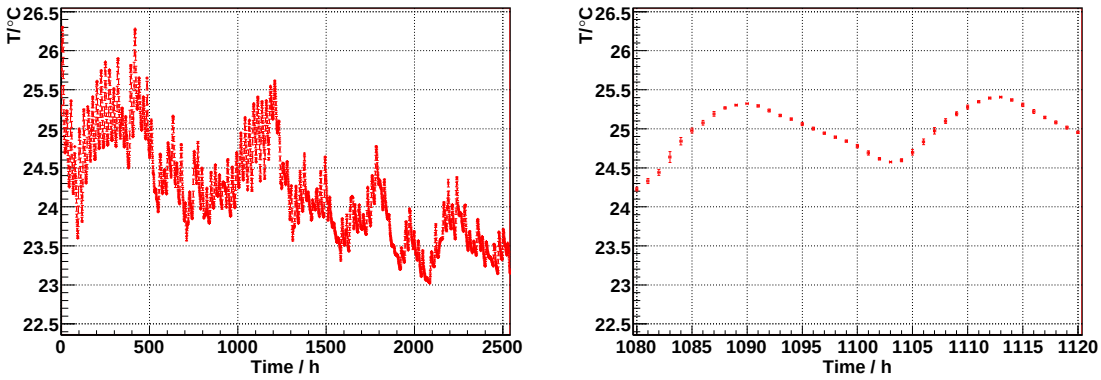

Figure 6.3: *Typical temperature variation during* 100 *days (left) and during* 40 *hours (right). The time* $t = 0$ *h marks the start of irradiation in the ageing experiment at* 23.7.2004, 9 *a.m. local time.*

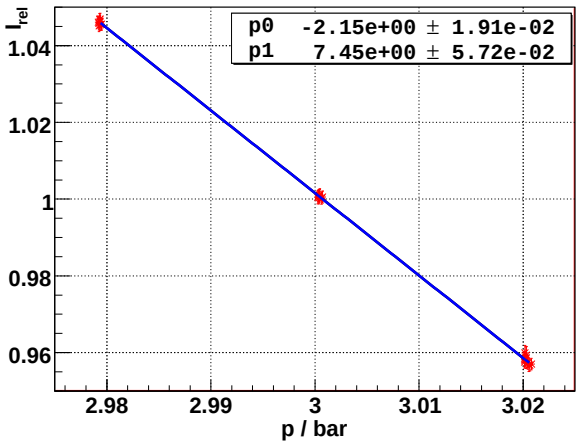

Figure 6.4: *Dependence of the relative drift tube current $\Delta I/I_0$ measured at $U = 3080$ V for different pressures and temperatures (small variations for given p). The parameter p0 denotes the gradient of the linear fit. It corresponds to a correction factor of 0.215%/mbar or 2.19%/K at $T_0 = 22°C$.*

and thus

$$\frac{dG(\rho)}{d\rho} = B \cdot \left(\frac{A}{\rho}\right)^{B-1} \cdot \left(-\frac{A}{\rho^2}\right) = G \cdot \frac{-B}{\rho} \tag{6.4}$$

A Taylor expansion of G for small density variations $\Delta\rho$ yields:

$$G(\rho_0 + \Delta\rho) = G(\rho_0) \cdot (1 - B \cdot \frac{\Delta\rho}{\rho_0}) \tag{6.5}$$

In the experiment, the gas density changes due to temperature and pressure variations. These quantities are related to the gas density ρ by the ideal gas law:

$$\rho = \frac{n}{V} \qquad p \cdot V = n \cdot R \cdot T \quad \Rightarrow \qquad \rho = \frac{p}{R \cdot T} \tag{6.6}$$

Thus the difference between temperature and pressure changes is the sign of the correction factor B: When the temperature rises at constant pressure, the gas density decreases. For a rising pressure at constant temperature the gas density increases. Hence Eq. 6.5 is correct for pressure corrections (replace ρ, ρ_0 by p, p_0), but for temperature corrections the formula changes to

$$G(T_0 + \Delta T) = G(T_0) \cdot (1 + B \cdot \frac{\Delta T}{T_0}) \tag{6.7}$$

With Eq. 2.10 and the Diethorn parameters from Eq. 2.11 one finds $B = 9.86$ for $U = 3080$ V, corresponding to a change of $3.4 \pm 0.34\%$ / K around $T_0 = 22°$C.
In [25] and in measurements of the current (see Fig. 6.4) with the component test significantly lower correction factors were obtained. They are listed in Tab.6.1. Finally a factor of 2.19%/K, measured with the component test, was used to correct the measured pulse heights for changes in temperature and pressure during the pulse height scan.

Voltage correction: With the Diethorn parameters, too large correction factors to compensate for temperature and pressure changes were obtained. Therefore it was decided to rely on values measured with the component test for the voltage

Origin	GIF [25]	Eq. 2.11	Fig. 6.4	Fig. 6.5
Voltage U_0	3080	3080	3080	$3070 - 3100$
Temperature T_0	20°C	20°C	$21.9 - 22.1$°C	$22.0 - 22.1$°C
Pressure p_0	3 bar	3 bar	$2.98 - 3.02$ bar	3 bar
factor	2.2%/K	3.36%/K	2.19%/K	0.465%/V
fit error	±0.3%/K	-	±0.02%/K	±0.003%/V

Table 6.1: *Factors for the pulse height correction due to changes of temperature, pressure and high voltage. The correction factor determined with the Diethorn parameters from Eq. 2.11 is much too high. Consequently measured values were taken for the correction.*

correction. These measurements are shown in Fig. 6.5 (right) together with a typical variation of the high voltage (left). From theoretical considerations a value of 0.5%/V can be deduced [34] for $\Delta G/G_0$. In the measurements with the component test 0.465 ± 0.003%/V were obtained.

Conclusion: From Fig. 6.3 (right) it is concluded, that the correction due to temperature changes is at most 1%. In Fig. 4.9 a typical pressure variation of 0.3 mbar in 12 hours is shown; pressure corrections are therefore negligible. The high voltage supply was also very stable as can be seen in Fig. 6.5 (left): A variation of 0.2 V during 48 hours can be identified as maximum fluctuation. This changes the gas gain by less than 0.1%.
Due to the stable conditions in the laboratory pulse height corrections were not performed. Instead, the changes of these parameters during the pulse height scans are given for some plots in the sections 6.4 and 6.5 to illustrate the constant environmental conditions.

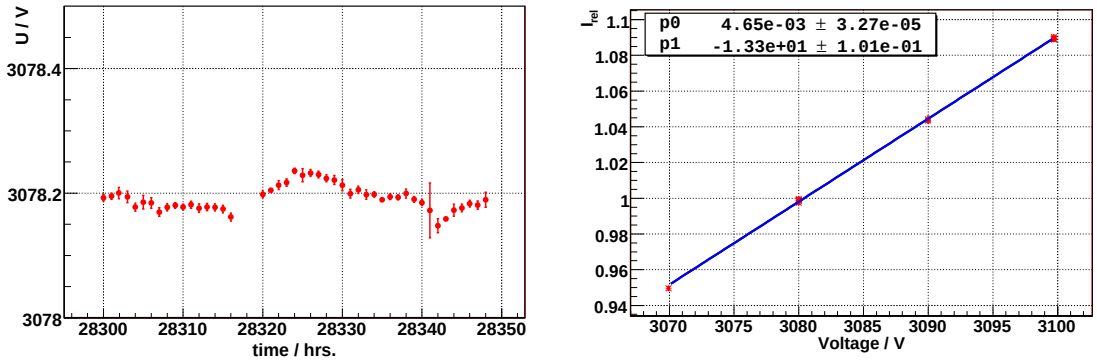

Figure 6.5: **Left:** *Typical variation of the voltage applied to a drift tube during* 48 *hours as measured by the slow control system.* **Right:** *Voltage dependence of the drift tube current measured around* U= 3080 *V.*

6.2.3 Relative pulse heights and uncertainties

The pulse height values C_i can be determined with a precision of $\sigma_i/C_i \approx 1\%$ with the methods described in section 6.2. To suppress differences of individual drift tubes, amplifiers and readout electronics, all pulse height values measured along the drift tubes were expressed in relation to the average pulse height C_{ref} obtained in the reference zone. Thus the uncertainty σ_{ref} of the absolute reference pulse height C_{ref} has an impact on the error σ_i^{rel} of all relative pulse heights C_i^{rel}:

$$C_i^{rel} = \frac{C_i}{C_{ref}} \quad \text{and} \quad \sigma_i^{rel} = C_i^{rel} \cdot \sqrt{\frac{\sigma_i^2}{C_i^2} + \frac{\sigma_{ref}^2}{C_{ref}^2}} \tag{6.8}$$

The absolute value of the pulse height in the reference zone is calculated as the average of two independent measurements (each with an error of $\approx 1\%$) at different positions in the reference zone. Depending on the absolute difference of the two measurements the uncertainty of C_{ref} spreads from $\sigma_{ref} = 0.7\% \ldots 3\%$. An example for a large uncertainty of the reference pulse height is shown in Fig. 6.18 (page 93) for drift tube number 31 (black and red data points).
Together with the small uncertainties due to uncorrected temperature and high voltage changes a relative error of about 2% for each pulse height C_i can be expected in average. The uncertainty of a pulse height value can increase if ageing effects occur. Then a pulse height spectrum does not look Landau shaped any more. Thus the uncertainty of the fitted values of the Landau distribution increases.

6.3 Definition of Ageing

With an estimated error of 0.02 for an ageing-free pulse height spectrum, 16% of all[2] reconstructed pulse height will be below 0.98. With measurements in 23 position this will happen 4 times in average. The situation becomes even more complicated if one (or both) of the reference pulse heights are measured too high (or too low). Consequently the following definition were made to classify ageing effects with a minimized risk of measuring merely statistical fluctuations:

- A drift tube shows (local) ageing effects, if the pulse height drops (locally) below 95%.

- A drift tube shows significant ageing effects, if the pulse height drops below 90%. This must occur in either two successive positions or the deterioration must progress in time.

- A drift tube is called inefficient in a particular region, if the pulse height drops below 70%. In former ageing experiments these tubes were classified as *dead*.

[2] 68% of all measured pulse heights are within $[-\sigma : \sigma]$, 16% are above and 16% below this interval.

- Component test: A component was classified as positive, when all drift tubes connected to this component showed significant ageing effects in several successive pulse height measurements.

To get an impression of the defined levels one may look at Fig. 6.6. It shows the relative pulse heights for two tubes of a station considered as clean.

Remarks:

- Throughout the following two sections the integrated charge is used as measure for the age of a tube. An integrated charge of 600 mC/cm corresponds to the projected ATLAS lifetime of 10 years.

- In the component test tubes of the same station never showed contradictory results. Either all drift tubes showed at least significant ageing effects or all of them were unaffected.

6.4 Results of component tests

The measurements and results shown in this section were carried out between July 2004 and October 2006. In the beginning, systematic studies with the sealant Molykote 111 were performed, to understand the ageing setup. Later, components of the ATLAS MDT gas system tests were tested, in particular a fully assembled ATLAS MDT gas distribution rack.

6.4.1 Clean gas system

One of the most important results obtained with the component test is the confirmation of Ar:CO_2 93 : 7 as a safe operating gas for the ATLAS muon system drift tubes. Without a single exception all drift tubes operated with a clean gas system did not show ageing effects, even after more than the required 600 mC/cm of integrated charge. Fig. 6.6 shows a prominent example for this statement: The result of a pulse height scan for two reference tubes after $\approx$ 3150 mC/cm of integrated charge on the wire. This corresponds to $\approx$ 52 years of ATLAS operation. No effects with respect to the definitions made in section 6.3 can be observed.
An important remark has to be made about the last position (at $x = 1050$ mm) in **most** pulse height scans. This position is often located close to one of the end plugs of a drift tube. Hence the electric field is influenced by the end plug such that the pulse height spectra reveal pulse heights intrinsically too low. Consequently ageing effects observed in the very last position are only real ageing effects if they fulfil one of the further two conditions: Either they progress with time or they are accompanied by ageing effects in the second to last position (at $x = 1020$ mm).

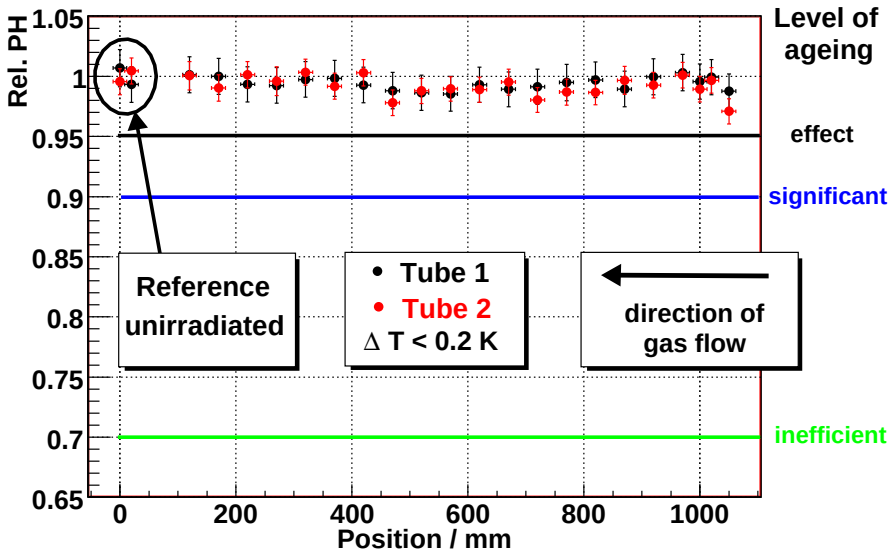

Figure 6.6: *Clean station: Result of a pulse height scan for two drift tubes after* 615 *days of irradiation. The definitions made in section 6.3 are shown as well as the temperature variation during the scanning procedure:* 0.2 *K corresponds to a negligible correction of about* 0.5%. *For all subsequent plots showing results of pulse height scans the gas enters from the right side. The reference zone is defined by the first two measurements on the left side. Please note the remark on the measurement at* $x = 1050$ *mm in the text.*

6.4.2 Studies with the sealant *Molykote 111*

The verification of the ageing test setup comprised two proofs of principle. On the one hand clean components should not be wrongly classified as positive. Therefore all test stations were set up with high cleanliness requirements[3]. The result described in the previous section demonstrates clearly that this condition is fulfilled. On the other hand silicon compounds, if present, should be detected quickly. This was tested with a rotameter that contained impurities (see next subsection). As another

[3]These were the same requirements as for the production of the MDT chambers

Station	No. 1	No. 3	No. 4
Tube No.	1,2,10,11	5,6,14,15	7,8,16,17
Flow rate / ml/min (Vol./day)	65 (9.2)	39 (5.5)	10 (1.4)
High voltage / V	3500	3420	3420
Average current density nA/cm	65 . . . 80	40 . . . 47	37 . . . 43

Table 6.2: *Operation parameters for the three stations testing Molykote 111 as source of contamination. The tube numbers are as defined in Fig. 4.2 (left). The average current density is calculated as* I/l *where* I *is the measured current and* $l = 0.98$ *m (the part of the drift tubes within the irradiation box).*

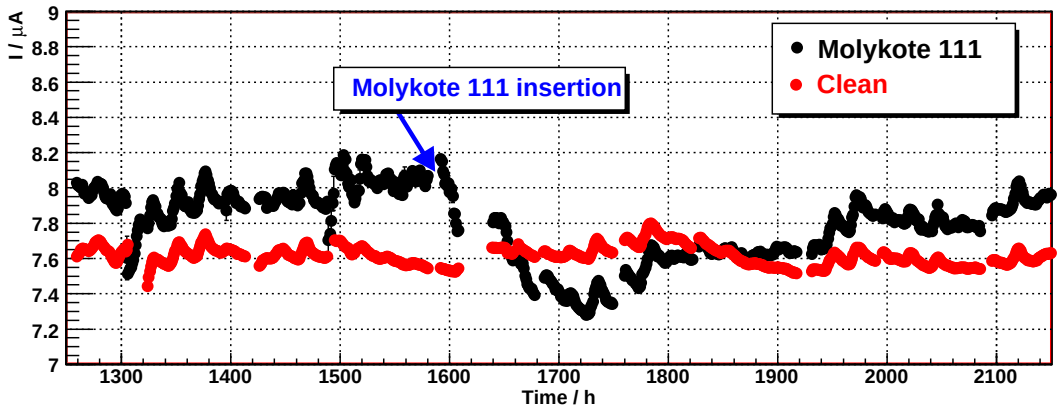

Figure 6.7: *The current of the tubes connected to the Molykote 111 sample (black) decreased immediately after high voltage was applied, while the current of a clean tube (red) remained almost constant.*

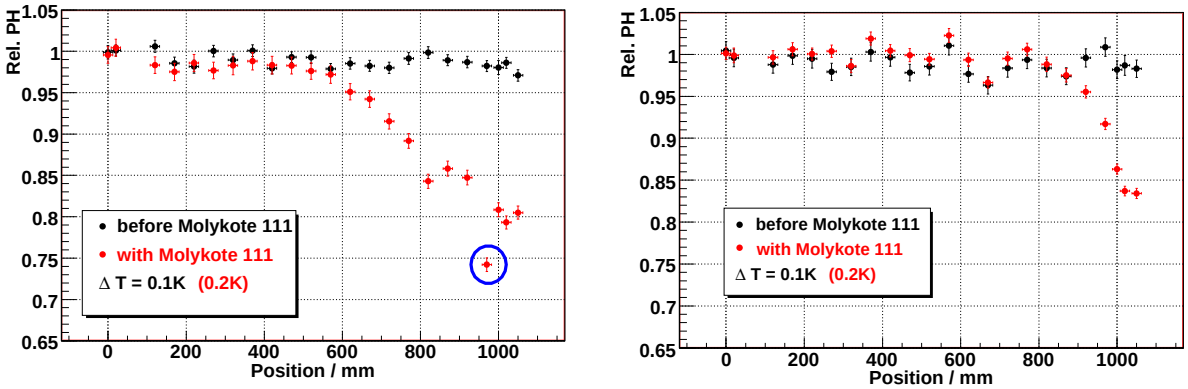

Figure 6.8: *Sensitivity test: These result were obtained in pulse height scans before (black) and after (red) inserting Molykote 111 in front of the station. The tubes were irradiated for only* 5 *days with the parameters listed in Tab. 6.2. The two plots show the results for tube* 11 *in station* 1 *(***left***) and tube* 14 *in station* 3 *(***right***). The blue circle in the left plot denotes that a radioactive source is close to this position (see also the current density distribution for tube* 11 *in the Appendix A).*

test silicon compounds were inserted to some stations to test the response of the drift tubes in the ageing setup. For this experiments the sealant *Molykote 111* was used as source of silicon compounds. It consists predominantly of hydroxy-terminated dimethylsiloxanes [68] and is offered as a sealant with a vapour pressure of almost zero. Products like this are often used to ease installation, because they are thought to be innocuous. But the opposite was impressively shown with the component test.

Sensitivity to silicon compounds: For the first tests, 0.9 g of Molykote 111 were inserted in front of three stations; the operation parameters for these three stations are summarized in Tab. 6.2. Immediately after applying high voltage to the drift

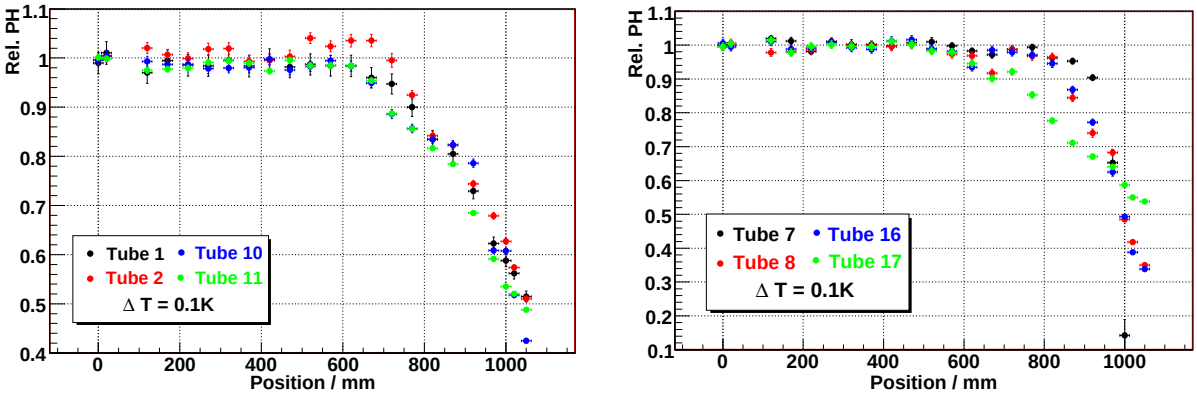

Figure 6.9: *Final results obtained with all tubes of two stations contaminated with Molykote 111. In station* 4 *(***right***) where the gas flow rate was lower as in station* 1 *(***left***), the extent of deterioration is bigger (note the different y-axis scale), while the range is shorter.*

tubes, the current of the drift tubes contaminated with Molykote 111 behaved different in comparison to the current of tubes operated without contaminations (Fig. 6.7). A pulse height scan, performed after only five days of irradiation (equivalent to 13 . . . 26 mC/cm), revealed severe ageing effects close to the gas inlet (Fig. 6.8) in all tubes connected to Molykote 111 samples. At this early stage the following effects were observed:

- The length of the deteriorated range along the drift tubes depends on the flow rate.
- The extent of deterioration after a certain time scales with the current density in the drift tubes
- Locally higher irradiation rates lead to locally higher deterioration (blue circle in Fig.6.8, left)

After these measurements the irradiation of the tubes was continued for two months to study further effects. At first the deteriorations of the drift tubes increased in their extent, while the length of the affected section remained constant. But then the degradation of the drift tubes stalled, at first for station 1, later also for the other two stations. The final results (after 330 . . . 390 mC/cm acquired in 2.5 months) are shown in Fig. 6.9 for the tubes of stations 1 and 4:

- The impact of the flow rate on the length of the damaged section of the drift tubes can be seen clearly. The different results observed for tube 17 with respect to the other tubes of station 4 might be due to unbalanced flow rates to the individual drift tubes. However there is no possibility to verify this assumption.
- The absolute extent of the observed deterioration is bigger at lower flow rates and does not depend on the current density.

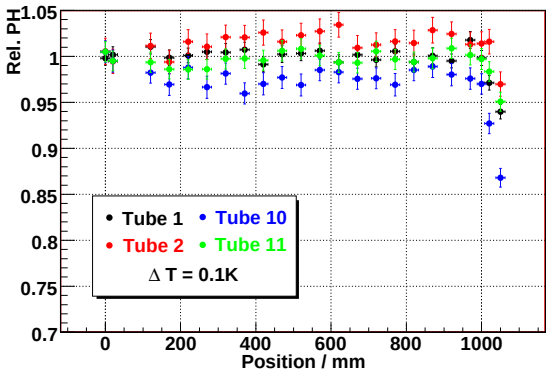

Figure 6.10: *A minimum concentration of silicon compounds in the gas flow is needed to cause damage to the drift tubes. The deterioration shown here was reached after* 1.2 *C/cm with a Molykote 111 sample almost completely dried out before the tubes were inserted.*

It was assumed that the progression of ageing effects stalled because the Molykote 111 samples were depleted. In the following the drift tubes in station 1 were replaced with new drift tubes to verify this assumption. After almost 10 month of irradiation, equivalent to 1.2 C/cm or 20 years of ATLAS operation, only one tube showed significant ageing effects. The others were merely affected as can be seen in Fig. 6.10, thus proving the assumption correct.
Furthermore these results indicated that a certain concentration of volatile silicon compounds in the gas flow is needed to cause damage to the drift tubes. This was examined in the following.

Minimum concentration The amount of 0.9 g Molykote 111 is too much for the ATLAS muon system drift tubes to withstand, although only a tiny fraction of the Molykote is volatile. Hence another test was set up where only 50 mg of Molykote 111 was inserted into a stainless steel tube that was connected indirectly with the gas distribution line (see Fig. 6.11). This way only diffusion processes determined the concentration of silicon compounds in the gas flow. The total flow rate of clean gas was 27 ml/min which is equivalent to 4 volume exchanges per day. In Fig. 6.12 the progression of the observed deterioration with time is shown: In the beginning the ageing effects progressed rather slowly, so that it was decided to heat the Molykote sample. By doing so, the ageing effects could be accelerated significantly. But once

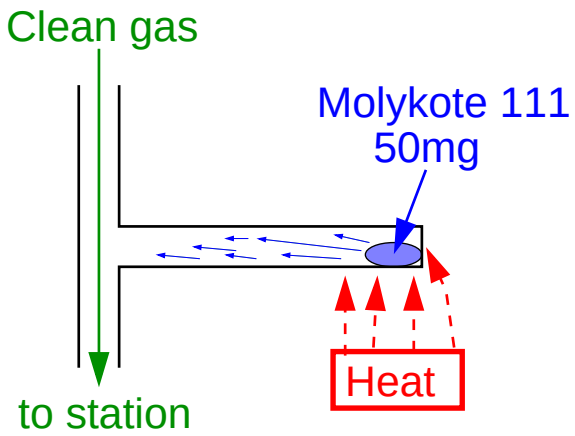

Figure 6.11: *Molykote 111 was inserted into a dead end tube. Hence only diffusion processes determined the concentration of volatile silicon compounds in the gas flow to the test station. Later the Molykote sample was heated to a temperature of* $T \approx 45°$ *C.*

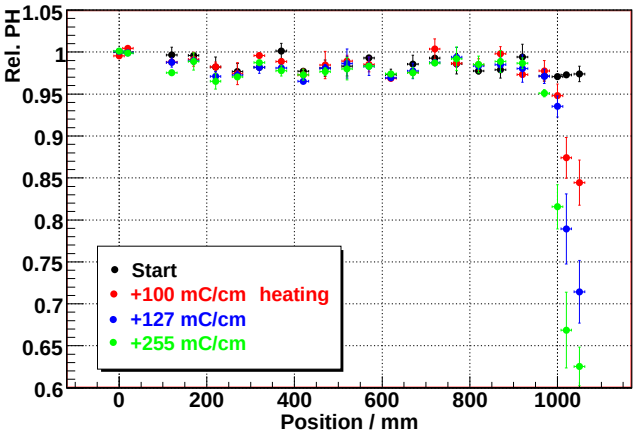

Figure 6.12: *Results obtained with only* 50 *mg of Molykote 111 as pollutant, mounted as shown in Fig. 6.11. Each measurement corresponds to the average pulse height of the drift tubes* 12 *and* 13 *in station number* 2*. By heating the sample the progression of ageing effects could be accelerated.*

again the progression of the observed effects came to an end after some time (green data points in Fig. 6.12).

Conclusions: Ageing effects can be triggered with the sealant Molykote 111 within a short time. However it is not possible to estimate the concentration of the contaminant in the gas mixture. Moreover the concentration was not constant in time. Therefore, a silicone source with a constant contamination level was required for further tests. This was achieved with HMDS (see Section 4.3) as contaminant for systematic studies carried out subsequently. The results of these studies are shown in Section 6.5.
Nevertheless, the results obtained with Molykote 111 can be explained if some assumptions about the non accessible parameters are made:

- Due to the low vapour pressure of Molykote 111 at room temperature, the saturation level of volatile contaminants in the gas mixture was reached in the beginning of the tests where 0.9 g Molykote were inserted to three stations. Thus the flow rate determined the absolute amount of impurities transported to the drift tubes. This explains two effects, observed for the tubes of station 1, which was operated at a higher flow rate:
  - Ageing effects proceeded faster
  - The progression of ageing effects stalled earlier
- When the absolute amount of impurities in the gas mixture decreased, the effects were more and more limited to shorter distances away from the gas inlet. This explains why the prominent peak of deterioration at position $y = 950$ mm, seen for tube 11 in the beginning (Fig. 6.8), vanished with time.
- The absolute amount of volatile impurities released to the drift tubes was the same for all three stations. Because of the lower flow rate to the drift tubes of the stations 3 and 4, these impurities were deposited within a shorter range. Hence the deterioration observed in the end, when the Molykote samples were depleted, was bigger for these drift tubes.

Detector	Component test (Freiburg)	TRT straw tubes (CERN)
Gas mixture Ar:CO_2	93 : 7	70 : 30
Current density	50 nA/cm	100 nA/cm
Flow rate	4 × nominal	10 × nominal
Irradiated range	98 cm	1 cm

Table 6.3: *Comparison of the operation parameters when testing the rotameter for the ageing setups at CERN (with TRT straw tubes) and in Freiburg (using ATLAS muon system drift tubes).*

The level of silicone contamination, simulated with the sealant Molykote 111, decreased with time. The interpretation of the results obtained with this setup therefore provided difficulties. Silicone contaminations caused by grease-lubricated gas system components will behave similar to Molykote 111.

6.4.3 Comparison with TRT results

During the planning of the new ageing experiment it was already clear, that there was insufficient time to check all components of the MDT gas system. It was therefore decided to verify some of these components with the ageing setup for the TRT straw tubes, already in operation at that time. The most important operation parameters of the TRT ageing setup are shown in Tab. 6.3 together with the corresponding parameters of the component test. More detailed information about the TRT ageing tests can be found in [68].
For a comparison of the two ageing setups a Voegtlin rotameter was used. This component was previously tested in the TRT ageing setup. When connected to the straw tubes, severe ageing effects were observed. After 327 hours (corresponding to ≈ 120 mC/cm) the pulse height in the irradiated region had dropped to 70%. In the MDT ageing setup at Freiburg the outcome was different. A comprehensive overview of the different stages of observed ageing effects with the rotameter as test sample in the component test is shown in Fig. 6.13: At first no ageing effects could

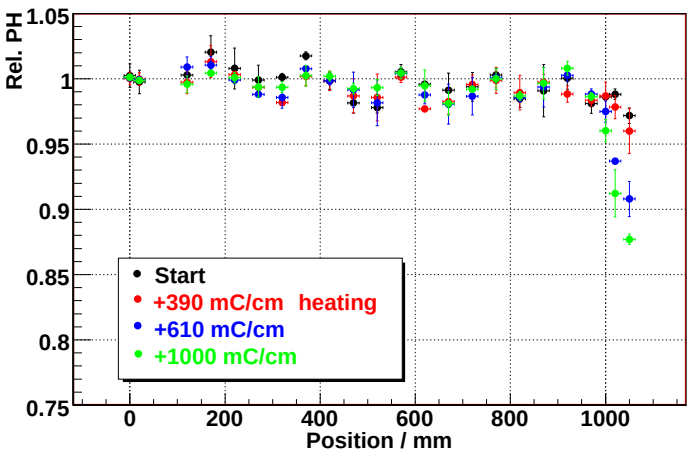

Figure 6.13: *Ageing effects observed with a Voegtlin Rotameter. As in Fig. 6.12 each measurement corresponds to the average of the tubes* 24 *and* 25*. After heating the rotameter, ageing effects could be observed rather quickly.*

be observed (red), so that the rotameter was heated to accelerate the process. This led to detectable ageing effects, but the extent of deterioration was significantly lower as obtained with the TRT ageing test. As described in the previous section, it is likely that most of the volatile part of the inherent silicone contamination in the rotameter was already gone. Nevertheless it looked as if the TRT setup is more sensitive than the component test. Therefore it was decided that components which tested negative with the TRT setup can be used for the MDT gas system. All ageing tests carried out by the TRT group can be found in [70].

6.4.4 ATLAS MDT Gasrack

The most important ageing test performed with the component test in Freiburg was the test of an ATLAS gas distribution rack (in the following called a *gas rack*). For this purpose, a completely assembled gas rack was shipped from CERN to Freiburg. To accelerate the test procedure the gas rack was heated moderately. This was achieved by three light bulbs as heaters within the gas rack (Fig. 6.14 left). The heated air was circulated with a fan which was also installed in the gas rack. The gas rack was packed in Styrofoam, so that a temperature of $T \approx 39°C$ could be reached inside.
In ATLAS the gas racks distribute the gas via independently operated channels to several chambers. Therefore a gas rack is built from the components shown in Fig. 6.14 (right): After passing several valves the gas is distributed by manifolds to the individual gas channels. The gas flow rate in each channel is measured with flow

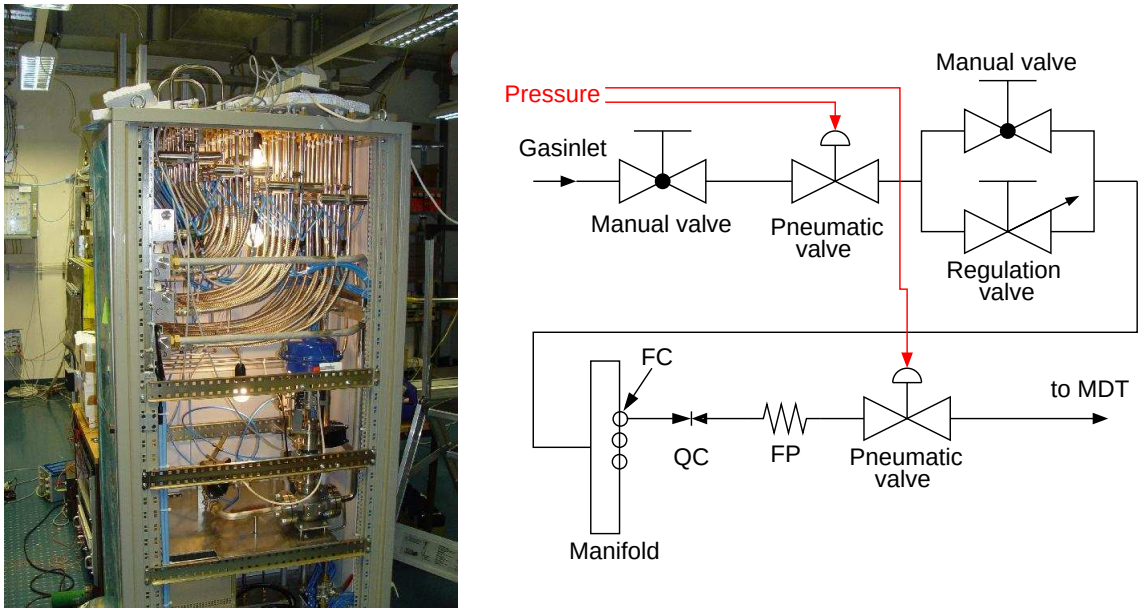

Figure 6.14: **Left :** *Gasrack heated with three light bulbs. For the test the rack was closed and packed in Styrofoam.* **Right :** *Gas distribution and regulation scheme within a gas rack. For the test the two pneumatic valves had to be opened with compressed air.*

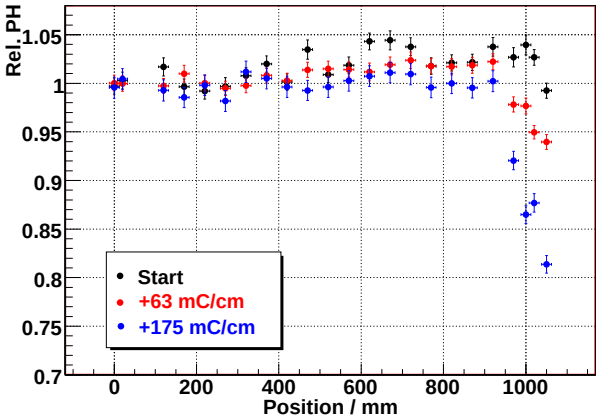

Figure 6.15: *Ageing effects in drift tube number* 17*, measured when an ATLAS gas distribution rack was tested. After an irradiation time equivalent to one year of ATLAS operation the effects were already clearly visible. With time the effects became significant in all tubes connected to the gas rack.*

cells (FC). Each outlet channel to the MDT chambers, mounted on on top of a gas rack, is connected with the manifolds via quick connectors (QC), flexible pipes (FP) and a pneumatic valve. After usage, the gas from all channels is returned to the gas distribution rack, where it is collected with a similar scheme.
For the ageing test, the whole gas rack was operated with the components described above being open, but passive. The outlets, which supply the MDTs in ATLAS with gas, were directly connected to the return inlets. After a complete cycle in the rack the gas was fed into drift tubes built into the component test. That way all components in the gas rack were tested at once. A detailed description of the ATLAS MDT gas distribution racks can be found in [71].

Result: Unfortunately the outcome of this test was positive, e.g. all drift tubes connected to the gas rack showed significant ageing effects within a time equivalent to 3 years of ATLAS operation (Fig. 6.15). In comparison to the results obtained with the heated sample of 50 mg Molykote or with the rotameter, the effects measured

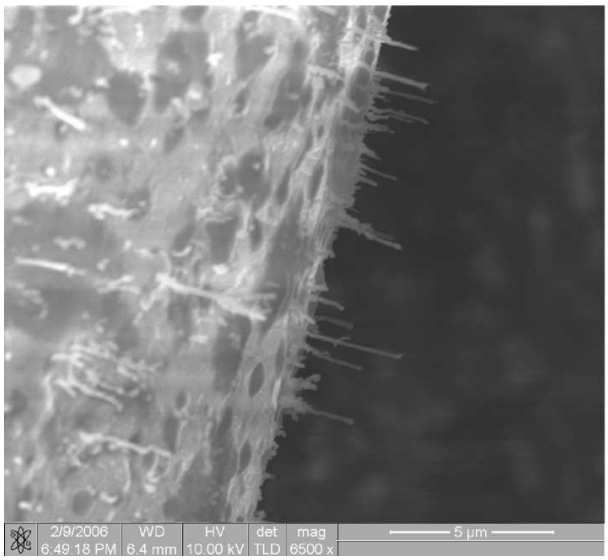

Figure 6.16: *SEM picture of the wire taken from one of the drift tubes connected with the gas rack. Whiskers with a length of* 5 *µm, perpendicular to the wire surface, are clearly visible. The piece of wire was taken* 5 *centimetres away from the gas inlet.*

with the gas rack were clearly bigger. In the following, the origin of these ageing effects was investigated (see next section).
After the test with the gas rack was completed, one of the affected tubes was opened and a piece of the wire from close to the gas inlet was removed for an SEM analysis. The result can be found in Fig. 6.16. Similar whiskers as already found with Beatrice at GIF (see section 3.3, particularly Fig. 3.7) were found on the wire. An EDX analysis of one of the whiskers revealed them as consisting of silicon and oxygen [72].

6.4.5 Component tests

In order to find the origin of the silicone contamination in the gas rack, several components built into the gas rack were tested separately. All tests are listed in Table 6.4: Only o-rings, used in the manifolds of the gas rack, lead to ageing effects in the drift tubes connected to them. Any other component, tested separately, did not lead to ageing effects in the drift tubes. The result obtained for the o-rings was confirmed by an ageing test of the TRT group [70] (Sample number 2065) and complemented by a chemical analysis carried out at CERN by order of F. Hahn [73].
In addition to the tests described so far only two other components were tested: A set of o-rings and a long aluminium tube, used for a different type of MDT chamber. These components were tested in the ageing setup because of preceding chemical analyses carried out by ACL[4] in order of the MPI Munich. In these analyses traces of silicone were found on the components. For the ageing test the o-rings were heated to 45°C. The long aluminium tube was only flushed with Ar:CO_2, without applying heat. Both tests were terminated with a negative outcome after an integrated charge of more than 1 C/cm.

6.4.6 Conclusions

The results obtained with the ATLAS MDT gas distribution rack were alarming. Although being ordered silicone-free, o-rings with traces of silicone were delivered.

[4] Analytisches Chemisches Labor, 72108 Rottenburg-Hailfingen: A company that often performs chemical analyses for Freiburg and MPI.

Component	Flexible pipe	Manifold	O-rings
Heated	$40 - 45°$ C		
Flow rate	$5 - 6 \times$ nominal		
High Voltage	3500 V		
Current density	60 . . . 75 nA/cm	55 . . . 70 nA/cm	50 . . . 60 nA/cm
Result	negative	negative	positive
Integrated charge	$\approx$ 1.9 C/cm	$\approx$ 1.9 C/cm	effects after 100 mC/cm

Table 6.4: *Operation parameters for the ageing tests with components from the gas rack. In Fig. 6.14 (right) one can see where these components are used.*

As a consequence they were replaced by a different type of o-ring. Nevertheless the ageing problem for the MDT chambers could not be seen as solved. Although the single tests of components used in the gas distribution racks were all negative, this does not mean that they are free from silicone. They all could be slightly contaminated, but all of them below a critical threshold. When used in the gas rack the overall concentration of volatile silicon compounds equals the sum of all individual concentrations. The critical value can then be exceeded easily. Furthermore it is possible that only some components in some gas racks are contaminated. This can happen when the production procedures for a component are changed by the manufacturer; that happened for example in case of the positively tested o-rings.
It was concluded that the risk of ageing in the ATLAS muon system drift tubes due to volatile silicon compounds in the gas mixture could not be excluded due to the numerous commercially available products used in the gas system. Hence a different solution was wanted: A gas filter to remove these volatile silicon compounds from the gas efficiently. The development of this gas filter is described in chapter 7 in detail.

6.5 Results with HMDS

The results summarized in the present section refer to systematic ageing studies with the help of a silicone source which is constant in time. The measurements were carried out between June 2005 and November 2007.

6.5.1 Systematic studies with HMDS

To estimate the impact of different levels of silicon contaminations on the performance of the MDT chambers, a constant silicone source with HMDS (see Section 4.3) was used. Drift tubes were contaminated with a well defined concentration of HMDS and the progression of ageing effects was studied. The parameters of these tests are listed in Tab. 6.5. In Fig. 6.17 (left) the ageing effects achieved with a contamination level of 10 ppm are shown. Within a short time the drift tubes became inefficient at the gas inlet side. The following additional observations were made:

- During the pulse height scan ($\approx$ 6 hours) the drift tubes were not irradiated. Therefore the HMDS in the gas mixture could not be deposited on the wire; it remained in the gas mixture. When the irradiation of the drift tubes was continued after the pulse height scan, the tubes were completely filled with a HMDS containing gas mixture. Thus the affected region grew longer (blue data points in Fig. 6.17).

- In the measurement after 94 mC/cm (blue data points in Fig. 6.17 ,left) the positions in the reference zone show also ageing effects (see Sec. 5.4.5): The absolute pulse height has dropped here by $\approx$ 5%. Thus the relative scale for the other data points is wrong.

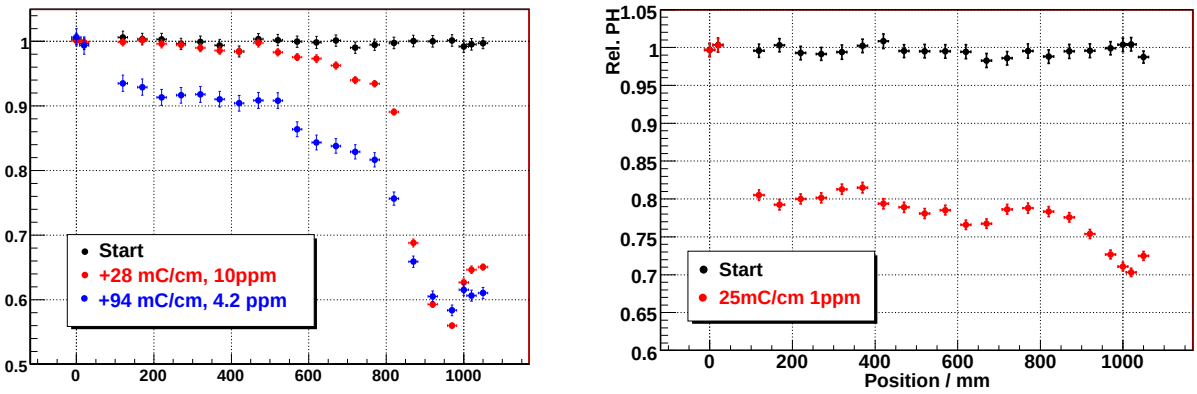

Figure 6.17: *Operating the drift tubes with a contamination level of* 10 *ppm HMDS leads to an enormous degradation of the drift tubes (here number* 23*) within a short time (***left***). The same is true for drift tubes contaminated with only* 1 *ppm HMDS, supplied with a higher gas flow rate (***right***), here shown for tube* 22*.*

Plot	Contamination level	Voltage	Flow rate
Fig.6.17 left	10 (4.2) ppm	3500 V	4.5 Vol./day
Fig.6.17 right	$\approx$ 1 ppm	3500 V	$\approx$ 10 Vol./day

Table 6.5: *Operation parameters for the systematic ageing tests with HMDS.*

- When the local gas gain in a drift tube decreased as a consequence of ageing, the local current density decreased also. Thus the local progression of the deterioration slowed down.

After this test a contamination level of only 1 ppm was tried with a higher gas flow rate (Tab. 6.5). The results are shown in Fig. 6.17 (right). In comparison to the measurement at 10 ppm with a lower flow rate the deterioration now affects drift tube completely, but the absolute extend is smaller.

Conclusion The concentration of silicon compounds in the gas mixture, needed to deteriorate the drift tubes, is well below 1 ppm. Unfortunately it was not possible to test with a lower HMDS concentrations, because then the systematic uncertainties of the HMDS source are of the same order as the concentration level (see section 4.3).

6.5.2 Partly shielded drift tubes:

In the following some tubes were shielded partly with lead to learn about the relation between irradiation intensity and extend of deterioration. In a first test three tubes were contaminated with HMDS and irradiated with a modified source arrangement. Two of them were shielded partly. A fourth drift tube remained without any contamination and shielding as a reference. All operation parameters can be found in

Number	Impurity	Voltage	flow rate	Shielding
11	-	3080 V		(reference)
20	$7-8$ ppm	3080 V	4.6 Vol/day	20 cm
21	$7-8$ ppm	3080 V	4.6 Vol/day	10-(2.4 unshielded)-10 cm
31	$7-8$ ppm	3080 V	4.6 Vol/day	-

Table 6.6: *Operation parameters for the systematic studies with partly shielded tubes. The shieldings started at the gas inlet side.*

Tab. 6.6. As a further improvement the drift tubes were flushed with clean gas before the pulse height scan was performed. Thus impurities could not spread in the drift tubes during this time, as it was the case for the measurements described previously.
From the Monte Carlo simulation (appendix A.2) an irradiation density around 1.5 kHz/can be retrieved. This corresponds to the maximum irradiation rate expected at ATLAS including the safety factor of 5. The voltage applied during irradiation was set to the default operating voltage of 3080 V. Thus the measurements show real-time ageing of the drift tubes if contaminated with $7-8$ ppm HMDS. The results are shown in Fig. 6.18 and Fig. 6.19:

During the first 14 days the HMDS source was switched on. Consequently the drift tubes showed a steadily decreasing pulse height in the affected area. In drift tube number 20, that was shielded on the first 20 cm, the maximum decrease after 14 days was slightly higher than in drift tube number 21. The reason is, that part of the HMDS in drift tube 21 was already deposited in the 2.4 cm gap at position 960 mm. In drift tube number 31, where the current density was lower, the HMDS was deposited more uniformly and less pronounced along the whole tube. A comparison of the local deterioration with the current densities, shown in Appendix A, reveals a clear correlation. During the following 5 days, when the HMDS source was switched off, the drift tubes did not deteriorate significantly, although being irradiated. This confirms, that a minimum concentration of impurities is required. After 19 days in total, the contamination was switched on again. Additionally one of the sources (at position 580 mm) was moved further towards the drift tubes, so that a highly non-uniform irradiation was reached (Fig. A.3 in the Appendix A, page 126). The progression of deterioration along the drift tubes (Fig. 6.19) again reflected the new current density distribution.

6.5.3 Conclusions

With the help of the HMDS source it was possible to cause ageing effects in the ATLAS muon system drift tubes within a short time for different impurity levels. Thus it was possible to estimate the impurity level, needed to deteriorate the drift tubes, to be significantly less than 1 ppm. Moreover, it was possible to get an impression about the impact of different experimental parameters (such as current density, flow rate, contamination level) on the extend of the observed drift tube deterioration. In contrast to the results obtained with Molykote 111, the effects

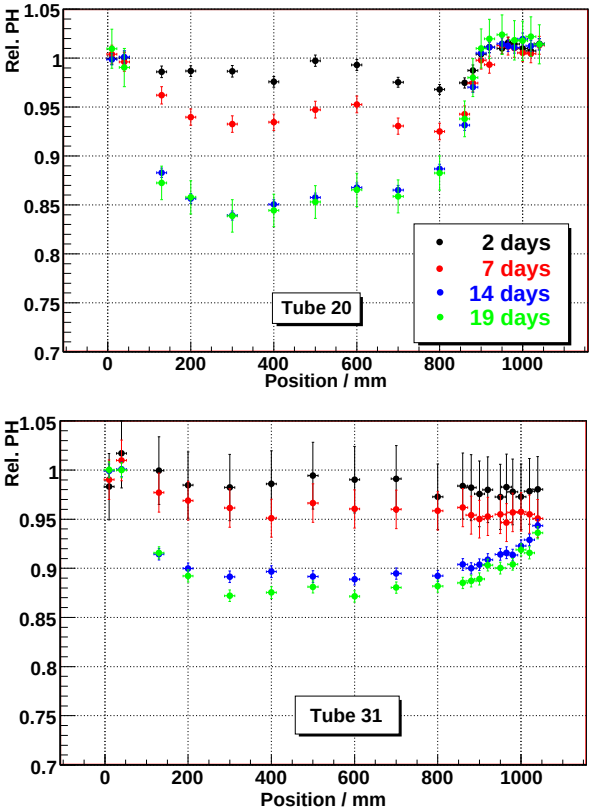

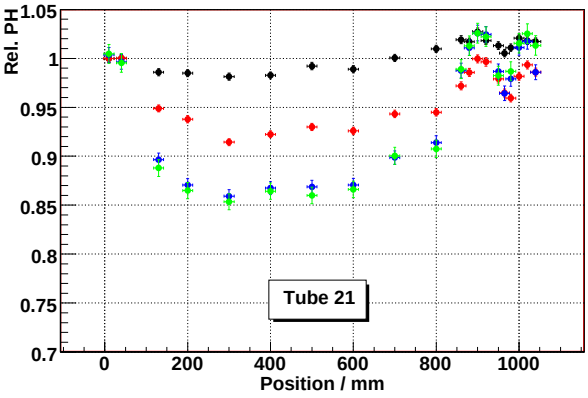

Figure 6.18: *Real-time ageing as expected for the ATLAS MDT muon chambers if contaminated with* $7-8$ *ppm of HMDS. The key is the same for all three tubes; the days given correspond to the run time after switching on the contamination. After* 14 *days the HMDS source was switched off.*

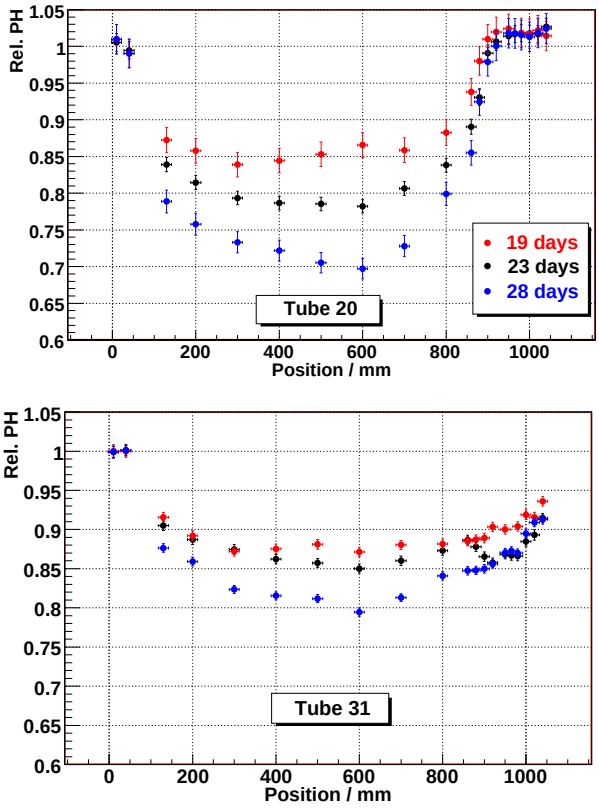

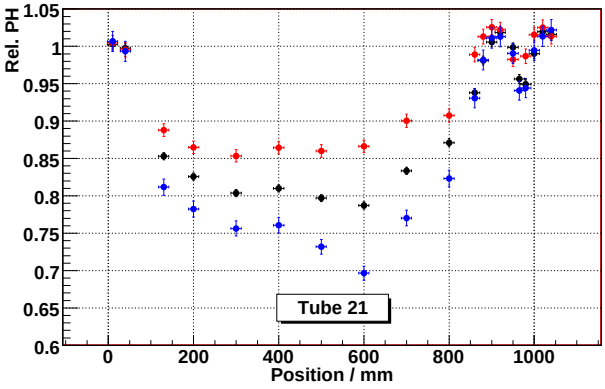

Figure 6.19: *After* 19 *days the contamination was switched on again. Now the arrangement of the radioactive sources was changed such that one source was located close to the drift tubes at position* 600 *mm, see also Appendix A.2*

were now not biased by a constantly decreasing impurity level due to a drying out contamination sample. Therefore the HMDS source was used subsequently to develop the gas filter for the ATLAS MDT gas system (next chapter).

6.6 Results of the ageing experiment Clean-α

In order to test the ageing properties of the drift tubes with a different type of radiation, an α-source ageing experiment was performed (see also section 4.2). This experiment was carried out between June 2007 and November 2007. The setup with an α-source required a minor modification in the analysis of pulse height scans. Therefore the implementation and analysis of the experiment is described before the result is shown and conclusions are made.

6.6.1 Implementation / Analysis

For this experiment no impurities were added to the gas mixture. The operation parameters for the drift tube are listed in Tab. 6.7: After 61 days of irradiation at an increased operating voltage of 3400 V no effects were visible. Hence the voltage was further increased to 3500 V in two steps.
To measure the local pulse height, the weak source already used in the other ageing experiments was moved manually along the drift tube. The distance of the source to the tube wall was $25 - 30$ mm which is equivalent to a scan range of 1.5 cm. The pulse height was measured on a fine grid of about 2 cm around the position of the α-source. Additionally, pulse height scans close to the end of the stainless steel collar (which was used to mount the α-source onto the drift tube) and far away from the source, close to the tube ends, were made. In order to calculate relative pulse heights, two reference pulse height values were needed. One of them was taken from the gas outlet side (as in the previous ageing experiments) of the drift tube. The other reference pulse height was taken from close to the collar for the following reason: The collar had an impact on the measured spectra such that the pulse height values were about 2% higher. By taking these two pulse heights as reference, the impact of the collar was as well respected in the reference pulse height as the undistorted spectrum.

Table 6.7: *Operation parameters for the ageing test with an α-source. The irradiated range along the tube was about 1 cm (see section 5.5).*

Time	Voltage	Current	flow rate
61 days	3400 V	50 nA	7.8 Vol/day
34 days	3450 V	59 nA	14 Vol/day
51 days	3500 V	69 nA	14 Vol/day

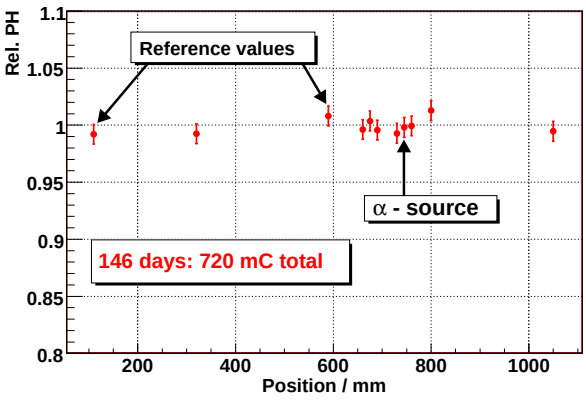

Figure 6.20: *No ageing effects were measured when an α source was used to irradiate a drift tube. The position of the α-source is indicated by the black arrow. After an integrated charge of* 720 *mC for the whole tube, the test was terminated.*

6.6.2 Result and conclusion

The measurement of the final pulse heights after 146 days of irradiation is shown in Fig. 6.20: No ageing effects were observed after an integrated charge of 720 mC. In Section 5.5 it was shown that more than 90% of the current was generated within 1 cm. Hence an integrated charge of more than the ATLAS life time of 600 mC/cm has been accumulated without any evidence for ageing.
This result agrees very well with the negative ageing results obtained for the HERA-B outer tracker with Ar:CO_2 as operating gas [31]. The previous positive ageing results with drift tubes under α irradiation (Section 3.2.2) are thus attributed to araldite used for the construction of the α-experiment.
Recently the LHCb collaboration reported about ageing problems in the outer tracker [55]. It is assumed, that araldite which was not completely cured is the reason for these problems.

Chapter 7

The ATLAS MDT gas filter

The results obtained with the component test, in particular for the MDT gas rack, strongly recommended the application of a filter into the ATLAS MDT gas distribution system. In the first section (7.1) background information about adsorption processes and filter construction is given. The requirements for the ATLAS MDT gas filter are defined in section 7.2. In section 7.3 the features of the designed filter are explained. In order to guarantee a safe operation in the MDT gas system many tests and measurements were necessary. The setups for these tests and their results are shown in section 7.4. Finally the production of the filters and their usage in the ATLAS experiment is described in the section 7.5.

7.1 Theoretical background

Before the filter design can be explained, some theoretical background about adsorption processes has to be given. Additionally, important parameters that determine the properties of a filter are briefly explained.

7.1.1 Adsorption theory

The adsorption model of Langmuir is used to describe the interaction processes between an adsorber surface and an impurity (or any other constituent of the gas mixture). Therefore three conditions have to be fulfilled:

- The adsorption probability is equal for all free binding sites of the adsorber.
- The probability to adsorb a molecule on a given binding site is independent from the coverage on neighbouring binding sites.
- The adsorption of gas constituents can not proceed beyond single layer coverage.

The Langmuir equation is derived from an equilibrium condition between adsorption and desorption processes. For the adsorption rate v_{ad} of an arbitrary gas constituent

the following relation holds:

$$v_{ad} = c_{ad} \cdot p_{ad} \cdot N \cdot (1 - \theta) \tag{7.1}$$

with the adsorption velocity c_{ad}, the partial pressure of the constituent p_{ad}, the number of total adsorption sites N in the adsorber and the percentage coverage θ. For the desorption rate of already adsorbed molecules a similar equation is found:

$$v_{des} = c_{des} \cdot N \cdot \theta \tag{7.2}$$

In the equilibrium the adsorption and desorption rates are equal and thus

$$\theta = \frac{K \cdot p}{1 + K \cdot p} \qquad \text{with} \qquad K = \frac{c_{ad}}{c_{des}} \tag{7.3}$$

The percentage coverage therefore depends on the partial pressure and thus on the concentration of the constituent in the incoming gas mixture. A total depletion of the adsorber can only be reached in the limit $K \to \infty$. This can be obtained by $c_{des} = 0$ and only then the purity after the outlet of a filter is equal to zero.

Remark: The value of K depends on several factors like the gas temperature and the gas pressure. This is important when filter properties with respect to temperature changes are discussed (Section 7.4.6).

7.1.2 Filter construction

A filter has to be constructed such, that the following requirements are fulfilled:

- For a complete depletion of the whole adsorber material, a uniform gas flow through the filter is required.
- A low flow resistance is wanted to allow an easy filter operation (no pumps are needed to compensate for the pressure drop).

With a few parameters it can be calculated, whether a filter can fulfil these requirements or not. They are introduced in the following. For a more detailed description of these parameters, see [64].
In the ATLAS MDT gas filter, the active adsorber component consists of spherically shaped beads. They are packed in a cylindrical filter case. Thus part of the volume, in particular close to the walls, will remain empty. This empty volume is generally called the void fraction Ψ

$$\Psi = 1 - \frac{V_{beads}}{V_{tot}} \tag{7.4}$$

To minimize the impact of processes happening close to the wall, the diameter D of the filter case should be sufficiently larger then the diameter of the beads:

$$\frac{D}{d_{beads}} > 10 \tag{7.5}$$

To calculate the expected pressure drop over a filter, the hydraulic diameter of the beads has to be introduced. When gas molecules pass the adsorber they have to follow small channels with mutable diameters. The hydraulic diameter expresses this mutable diameter in terms of an effective diameter of a cylindrical tube:

$$d_{hydr} = \frac{2}{3} \cdot \frac{\Psi}{1-\Psi} \cdot d_{beads} \tag{7.6}$$

Another important quantity for liquids and gases is the Reynolds number. For a gas with the velocity v_0 in the empty filter case, the Reynolds number is:

$$Re = \frac{v_0}{\Psi} \cdot \frac{d_{hydr}}{\nu_{gas}} \tag{7.7}$$

where ν_{gas} is the dynamic viscosity of the gas mixture. High Reynolds numbers ($Re > 3000$) refer to turbulent flows. Below $Re < 1160$ any real flow behaves like a laminar flow [65]. For Reynold numbers too low the axial dispersion of the gas entering the filter is only driven by molecular diffusion. Hence the adsorber will not be completely depleted. To minimize this effect, a ratio between the height H and the diameter D of the filter of 5 is often recommended [64].
The beads in the filter case are flushed by the operating gas. Thus molecular friction will occur that causes an undesired pressure drop. The friction factor ζ depends on the Reynolds number. For spherical beads one finds [64]:

$$\zeta = 2.2 \cdot \left(\frac{64}{Re} + \frac{1.8}{Re^{0.1}}\right) \tag{7.8}$$

With Eq. 7.4 to Eq. 7.8 the pressure drop over a filter can be calculated as follows:

$$\Delta p = \zeta \cdot \frac{H}{d_{hydr}} \cdot \frac{\rho_{gas}}{2} \cdot \left(\frac{v_0}{\Psi}\right)^2 \tag{7.9}$$

With this knowledge and these formulae the design of the ATLAS filter can be managed.

7.2 Requirements for the filter

The total volume of the ATLAS MDT gas system is 800 m^3 [6]. When the MDT chambers will be in operation, an exchange rate of one gas volume per day is foreseen. At an operating pressure of 3 bar this corresponds to a flow rate of approximately 1670 l/min. The gas is supplied to the individual MDT chambers with gas distribution racks, as tested with the component test in Freiburg (section 6.4.4). Each gas rack has several gas channels to supply gas to groups of a few MDT chambers. Here the filters are mounted - one filter per gas channel - just after the outlet-channels of the gas racks. The following requirements were defined for a filter:

- The gas flow of 1670 l/min is distributed by 272 such channels, so that each filter has to purify an flow rate of 6.2 l/min in average. For some of the barrel MDTs almost 10 l/min must be filtered [63]. At these flow rate the pressure drop over a filter must not exceed 20 mbar [69].

- The clearance above the gas racks is about 35 cm in the worst case. A filter has to fit within this space including all connectors.
- The level of contamination is a priori not known. Hence it must be possible to exchange filters quickly if needed.
- A filter must not introduce impurities itself, as for example dust (this is often a problem with charcoal filters).
- Fig. 2.7 shows the impact of the water and argon content on the maximum drift time. Since the accuracy of the drift tubes depends on the correct gas mixture, the filter must not change the gas mixture significantly.
- The possibility to determine the amount of adsorbed impurities after a filter exchange is wanted. With this knowledge the exchange intervals can be adapted. Furthermore one would learn about the actual impurity level in the gas system.

In summary a small and clean filter with a high adsorption capacity, exclusively for impurities, was looked for.

7.3 The ATLAS MDT gas filter

The filter, designed for the gas system of the ATLAS MDT chambers, comprises zeolite beads as active filter component, and mechanical components, like the filter case. Both are described in the following.

7.3.1 Zeolites

Zeolites[1] are alumino-silicate minerals with a micro porous structure. On molecular level they are built from SiO_4 and AlO_4^- tetrahedras, that are further linked to rings. The smallest ring consists of four tetrahedras and is therefore called a 4T-ring. The so-called sodalite cage (or β-cage) is a combination of 4T-rings and 6T-rings, as can be seen in Fig. 7.1 (left). The faujasite zeolite, which is used for the gas filter, consists of several sodalite cages interconnected by 6T-rings as shown in Fig. 7.1 (right). The crystal lattice of zeolites includes small holes, the micro porous structure. In the application as a filter for the MDT gas system, these holes will accommodate impurities.
Because of their huge specific surface of more than 1000 m^2g^{-1}, zeolites have a high adsorption capacity. Many zeolites are hygroscopic and can contain water up to 55% of their own empty weight. For the MDT gas filter a hydrophobic zeolite was looked for[2]. In addition the adsorption of CO_2 should also be low. In the end the

[1] Greek: Zein "to boil", lithos "stone". The name allows for the fact that some zeolites can adsorb large quantities of water. When heated, the water is released as steam. Then the zeolite stones look as if they were boiling.

[2] Water in needed in the MDT gas system on a low level. A high affinity to water could change the gas mixture significantly.

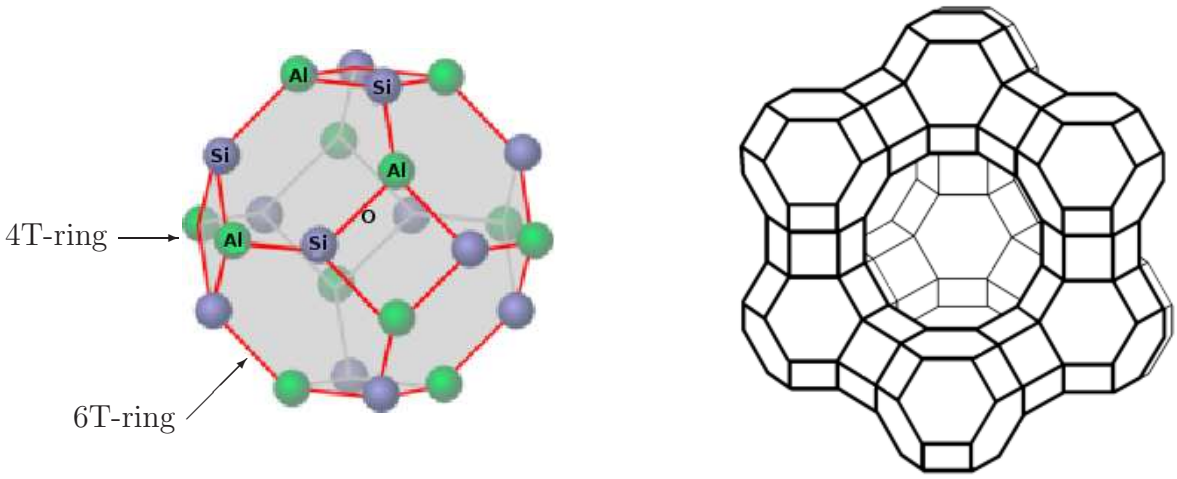

Figure 7.1: *Structure of a zeolite: In the* **left** *picture a sodalite-cage is shown. It is made of connected rings of Si- (blue) and Al-tetrahedra (green). The red lines denote oxygen atoms which are shared by silicon and aluminium atoms. These sodalite cages are further linked among each other by 6T-rings. This way bigger structures, like the faujasite zeolite shown on the* **right** *side, are built.*

zeolite type *UK*8 from *Chemiewerke Bad Köstritz* was selected. The application for this type of zeolite is the selective removal of organic compounds from polar substances containing gases [67]. The zeolite was delivered granulated to beads with a diameter between 1.6 and 2.5 mm. Many measurements and tests had to be performed to assure, that this zeolite fulfils the requirements defined in section 7.2. These measurements are described in section 7.4.

ATLAS TRT system: To purify the gas system of the ATLAS TRT straw tubes, several different filter techniques and materials come into operation. Among others, zeolites are used also. In [68] tests with several types of zeolites are described. In the end, the zeolite type *UK8*, which had the highest adsorption capacity to impurities in these tests, was selected.

7.3.2 Mechanical filter parts

The mechanical part of the filter comprises several parts that serve different purposes. They are described in the following.

Zeolite case: The filter case, that houses the zeolite beads, consists of a stainless steel tube with an outer diameter of 40 mm and a wall thickness of 1 mm. The length of this tube is 190 mm, so that the filter includes a volume of $V \approx 215$ cm^3. With these dimensions the recommended ratio of filter height to filter diameter could be exactly fulfilled. The ratio of bead diameter to tube diameter defined in

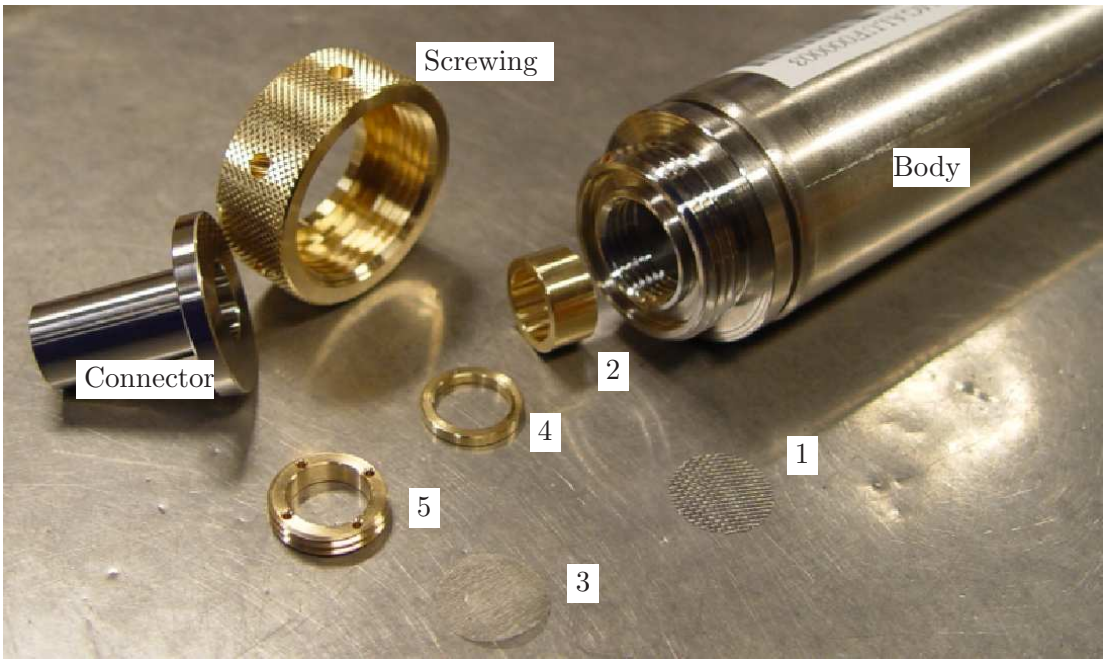

Figure 7.2: *Filter case with the flange welded on. The other components needed for the filter connection to the gas rack are also shown. The parts labelled with* 1 *to* 5 *are inserted in this order into the hole in the centre of the flange. The meshes to hold the zeolite beads in their place (*1*) and remove dust (*1 *and* 3*). The connector is forced with the screwing against an o-ring (not visible), that is put into the flute in the flange.*

Eq. 7.5 is also preserved. Thus a void fraction of $\Psi \approx 0.4$ can be assumed [64].

Connection to the gas system: To both ends of the zeolite case specially designed flanges are welded. They are made of stainless steel and incorporate further components. The upsides of the flanges have a flute to incorporate an o-ring. Thus a gas-proof connection to the gas system can be achieved. For this purpose two different types of connectors were developed as counterpieces to the flange. One of them connects to the gas rack, the other one is connected to the copper pipes which supply the MDT chambers with gas. They are manufactured with a smooth surface. This surface is pressed against the o-ring when the flange and the connector are contracted with a brass screwing. In Fig. 7.2 the filter body and all ingredients for the connection to the gas rack can be seen. The connector to the gas pipes comprises a self-blocking valve. It is shown in Fig. 7.3.

Ingredients and mounting: To remove dust, possibly arising from rubbing zeolite beads, two wire meshes are incorporated into both flanges (see Fig. 7.2, meshes labelled with 1 and 3). At first, a raw mesh with an aperture of 600 μm and a

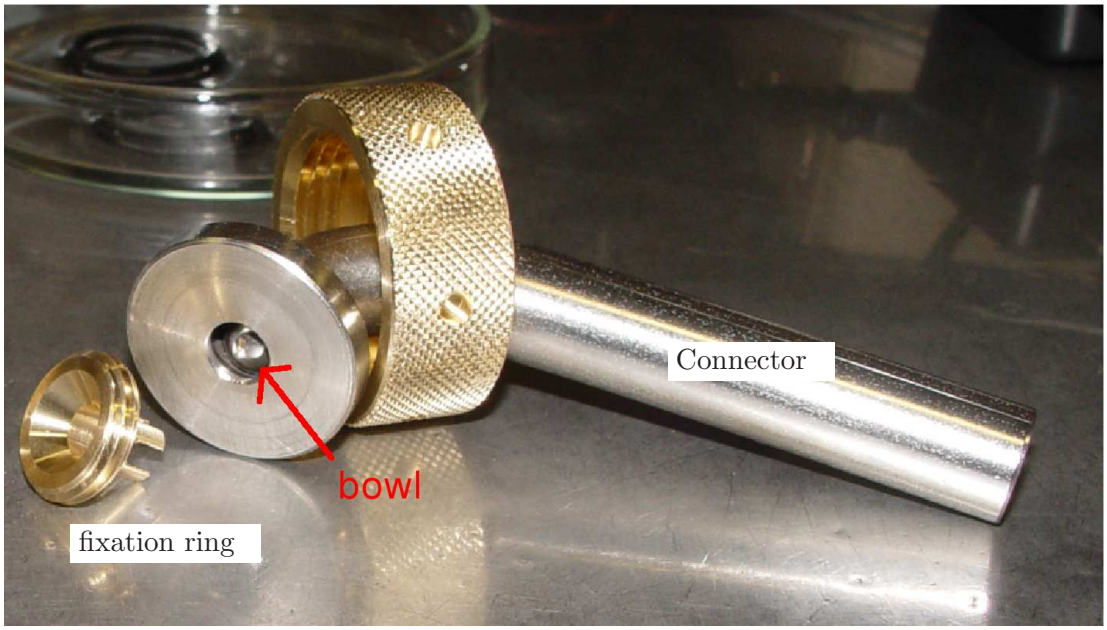

Figure 7.3: *Connector and fixation ring of the filter used for the connection with the gas pipes. Within the connector the bowl used for the self-blocking mechanism can be seen.*

wire thickness of 150 μm is used. This mesh holds the zeolite beads in their place and is separated by a distance ring (2 in Fig. 7.2) from a second mesh. With an aperture of 60 μm, fabricated with wires of 28 μm thickness, this fine mesh removes dust grains if present. A second thin separation ring (4) avoids friction on the fine mesh when the fixation ring (5) is screwed into the flange. Finally the *connector* is pressed with the *screwing* against the o-ring (not shown) in the flute of the flange.

Self-blocking valve: On the gas outlet side the components put into the flange are the same. But the *fixation ring* and the *connector* are slightly modified (Fig. 7.3). On this side a self-blocking mechanism in the connector is needed to exchange the filters from time to time. This is achieved with a bowl and a special connector plate with a conically shaped inner surface. The fixation ring looks like a crown which fits into the connector plate. When the filter is attached to the connector with the brass screwing, the crown lifts the bowl and the gas can flow through the filter into the connector and thus into the copper gas pipes.

Filter exchange procedure: When a filter is removed, the gas valve of the corresponding gas channel in the gas rack has to be closed at first. Now the gas flow from the gas rack to the MDT chamber(s) stops. In the next step the connection to the copper gas pipes is opened by releasing the brass screwing on the gas outlet side of the filter. When the screwing is opened completely, the connector must be lifted a little bit. This is possible due to the flexibility of the copper pipes. The

bowl is then pressed in its designated position on the cone by the over pressure in the MDT chambers. Hereby a satisfying gas tightness is reached. Now the filter can be unmounted on the gas rack side. Further details about the exchange procedure can be found in section 7.5.

7.4 Measurements and results

In the ATLAS MDT gas system, the filter should bind volatile silicon compounds permanently. This has to be achieved without causing a too large pressure drop. Further the filter should not change the gas mixture due to the adsorption of CO_2 and water. These properties of the filter were measured intensively and are described in this section.

7.4.1 Pressure drop

One of the most important properties of the filter is its flow resistance for different gas flow velocities. The flow resistance causes a pressure drop. Since the gas system at ATLAS will be operated with a circulation pump, this pressure drop must not exceed a certain limit. Otherwise the pump would not manage to maintain the gas circulation. As a limit $\Delta p < 20$ mbar at a gas flow velocity of 8 Nl/min was set [69]. For the measurement of the pressure drop, a filter, filled with zeolite, was mounted as shown in Fig. 7.4 and flushed with nitrogen. A differential pressure meter *dp* measured the pressure difference Δp between filter in- and outlet for different flow rates at the nominal pressure of 3 bar. The value of Δp is determined by measuring the displacement of a membrane between the two inlets; hence no gas was bypassed from the filter. Subsequently the measurements were repeated without a zeolite filling. This way the fraction of the pressure drop that is not caused by the zeolite beads was measured. The results are shown in Fig. 7.5 (left) for different adjustments of the flow rate. In Fig. 7.5 (right) the difference of the two measurements is compared to calculations performed with Eq. 7.9 for three different combinations of the bead size d and the void fraction Ψ. The comparison reveals a good agreement with a bead size of 2 mm (the zeolite is delivered as granulate with a bead size between 1.6

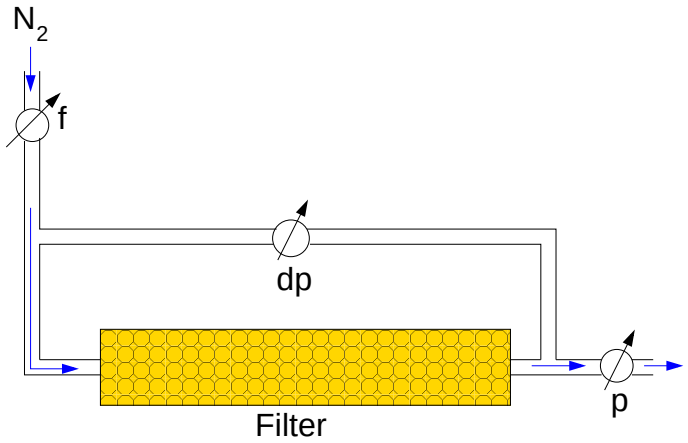

Figure 7.4: *Schematic setup to measure the pressure drop over the filter. The differential pressure meter* dp *measures the pressure drop for different flow rates* f *at* $p = 3$ *bar. The measurements were carried out with and without a zeolite filling. For the flushing nitrogen was used.*

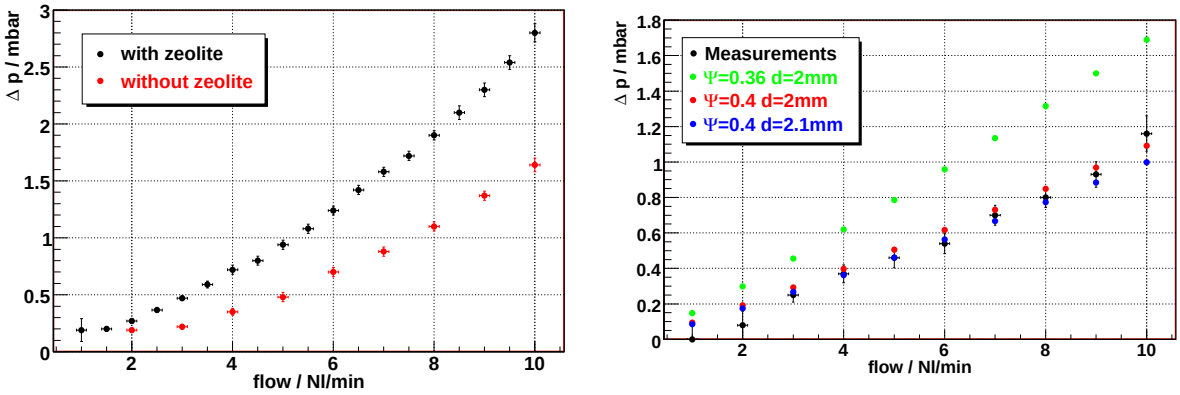

Figure 7.5: **Left:** *Absolute pressure drop over the filter measured with the setup shown in Fig. 7.4 with (black) and without (red) a zeolite filling.* **Right:** *The difference of the two measurements is compared to calculations with Eq. 7.9. The model with* $\Psi = 0.4$ *and* $d_{bead} = 2mm$ *fits best to the measurements.*

and 2.5 mm) and a void fraction of $\Psi = 0.4$. With these numbers the pressure drop was calculated for Ar:CO_2 93 : 7 and added to the pressure drop measured with the empty zeolite case. At a flow rate of 10 l/min the expected pressure drop over the MDT gas filter is

$$\Delta p < 5\text{mbar} \tag{7.10}$$

This is managed easily by the circulation pump.

7.4.2 Proof of principle

A first test should provide information whether the zeolite UK8 is capable to inhibit drift tube ageing. This was checked with a simple prototype filter[3] at a low flow rate of ≈ 70 ml/min. Drift tubes were supplied via the prototype filter with Ar:CO_2 that was highly contaminated with HMDS. The impurity content was steadily increased from 25 ppm in the beginning up to 175 ppm after 8 days. In total, the filter was flushed for 30 days with an average contamination level of ≈ 140 ppm. During this time pulse height scans were performed regularly. They all turned out negative with respect to ageing effects; the last one is shown in Fig. 7.6. The test was terminated after this pulse height scan and the filter weight was determined. In comparison to the weight at start-up the filter has gained a weight of 3.44 g.
A simple calculation of the absolute amount of HMDS transported with the gas flow yields:

$$V_{HMDS} \approx \frac{0.07\text{l}}{\text{min}} \cdot \frac{1440\text{min}}{\text{day}} \cdot 30\text{days} \cdot 140\text{ppm} = 0.42\text{l}$$

With a molecular weight of 162.38 g/mol of HMDS, a mass increase of 3.07 g can be expected. This value has an relative uncertainty of ±15% since the estimated

[3]The prototype filter contained only ≈ 65 g of zeolite, whereas the final ATLAS filters contains 120 g of zeolite.

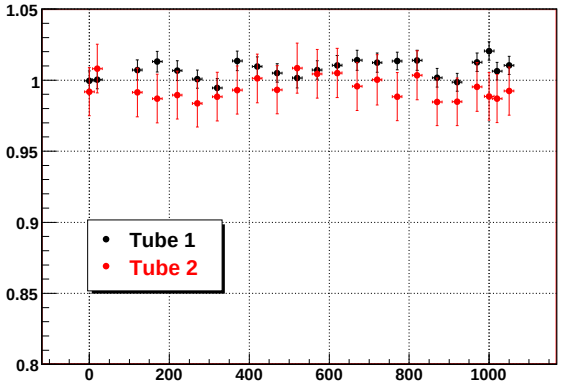

Figure 7.6: *Proof of principle for the zeolite UK8: After one month still no ageing effects were observed in all tubes (two of them are shown here) supplied with a highly contaminated gas mixture via a prototype filter. In Fig. 6.17 the pulse height along drift tubes connected to the HMDS source without a zeolite filter are shown after a similar amount of time.*

contamination level is deduced from sensor data of the HMDS source (see section 4.3). Additionally little amounts of water and CO_2 were adsorbed too.
Nevertheless it was found that the zeolite UK8 removes silicon compounds efficiently from the gas mixture at a flow rate of $\frac{1}{100}$ of the desired flow rate at ATLAS. Ageing effects could not be observed, even after ≈ 3 g of HMDS in the filter. This corresponds to $\approx 4.6\%$ of the zeolite's empty weight.

7.4.3 Absolute adsorption capacity

In the following an advanced prototype filter, containing already 108.7 g of zeolite, was connected to a gas line and flushed at 65 ml/min to atmospheric pressure. Hereby the HMDS concentration was varied between 45 ppm in the beginning and up to 500 ppm in the end. The weight of the filter was determined regularly and compared with the expected mass gain Δm calculated with sensor data from the HMDS source. The result is shown in Fig. 7.7: At a contamination level of 500 ppm the zeolite beads adsorb HMDS up to 12% of their empty weight.
From the Langmuir equation Eq. 7.3 it is known, that the percentage coverage depends on the partial pressure of the incoming impurity. Hence the filter was flushed in the following with higher flow rates and with a lower contamination level of 180 ppm to learn about this dependency. Later the HMDS source was switched off

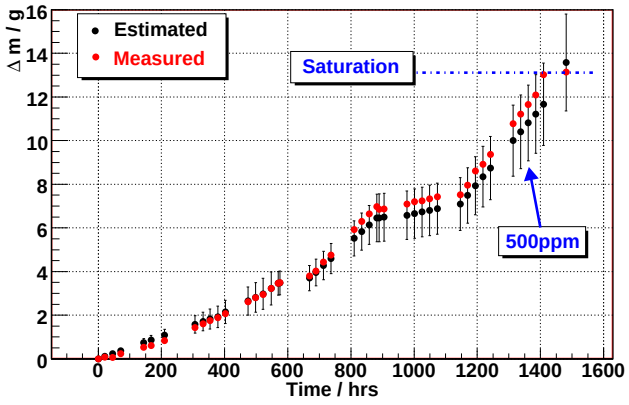

Figure 7.7: *Up to a mass gain of $\Delta m \approx 13$ g the determined filter weight (red) followed the expected increase (black). Then the saturation point of the filter was reached. For this test the filter was filled with* 108.7 *g of zeolite and operated with a flow rate of* 65 *ml/min.*

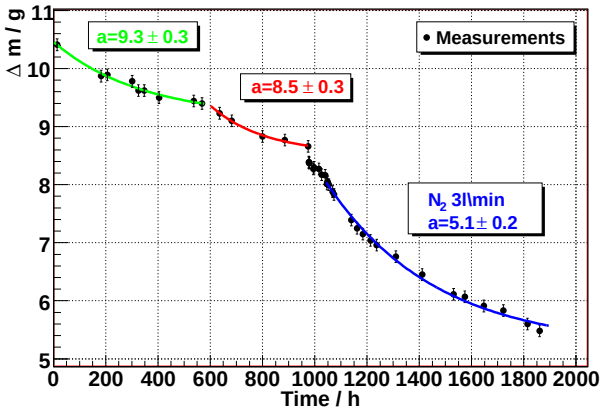

Flow rate	Impurity level	Δm / g
0.065 l/min	500 ppm	13.0 ± 0.2
0.13 l/min	180 ppm	12.3 ± 0.3
0.13 l/min	remnants	9.2 ± 0.3
0.26 l/min	remnants	8.5 ± 0.3
3.0 l/min	0 ppm	5.2 ± 0.2

Figure 7.8: *Adsorption of HMDS at different flow rates through the filter. For the measurement at a flow rate of* 3 *l/min nitrogen was used, in all other cases Ar:CO_2. The data was fitted with the exponential relation given in Eq. 7.11. The last column of the table on the right side refers to the fit parameter a.*

completely. Now HMDS remnants within the gas pipes remained as only impurity. With an even higher flow rate their concentration could be further reduced. Finally the filter was removed and flushed with dry nitrogen at 3 l/min. The result is shown in Fig. 7.8: Whenever the impurity level was changed, the total amount of adsorbed HMDS adapted to the new impurity level (p in Eq. 7.3). The adaptation is well described by an exponential relation

$$\Delta m(t) = a + b \cdot e^{-c \cdot (x-d)} \tag{7.11}$$

that was fitted to the data for each contamination level. The results of the fit can be found in the table next to Fig. 7.8. From these measurements a maximum adsorption of 5.2 g HMDS for a filling weight of 108.7 g zeolite is deduced.

7.4.4 Adsorption of other gases/vapours

Besides volatile impurities zeolites can also adsorb other constituents of the gas, for example CO_2 and water. If exposed to air, nitrogen and other constituents of air can be adsorbed. From [66] a specific nitrogen adsorption of 1.3 ml/g at 1 bar was reported. For an ATLAS MDT gas filter, with a total filling weight of $\approx$ 120 g, this corresponds to an absolute mass of 0.2 g nitrogen. Further experiments were carried out to measure the specific adsorption capacities of the filters. Their results are summarized in Tab. 7.1. The experiments were carried out as follows:

CO_2 and Ar:CO_2 : To measure the adsorption of CO_2 two tests were performed. In a first test a filter was connected to a CO_2 supply line operated at 3 bar. The filter outlet was closed for this test. After about 20 min a weight increase of $\Delta m \approx 4$ g was measured, in addition the filter became warm. Flushing the filter with dry nitrogen at a flow rate of 1 l/min restored its original weight within 5 minutes. By

Gas / Vapour	amount	Removal time	Remark
N_2 / O_2	0.2 g	not measured	[66]
CO_2	4 g	≤ 5 minutes	Maximum CO_2 adsorption
Ar:CO_2 93 : 7	0.5 g	≤ 5 minutes	CO_2 adsorption in ATLAS
water	0.85 ± 0.15 g	1 week	situation when filters are filled
water	78 g	several weeks	water poured over zeolite

Table 7.1: *Absolute adsorption of different gases or vapours by the ATLAS MDT gas filter. The removal times were measured by flushing the filter with dry nitrogen at a flow rate of* 1 *l/min.*

doing so the filter cooled down.
In the second test the filter was connected to a gas supply line with Ar:CO_2 93 : 7, again with a closure on its outlet side. This time a weight gain of only ≈ 0.5 g could be measured. A cross-check with a filter connected to an argon supply line verified that argon, as a noble gas, is not adsorbed by the filter. Hence the measured weight difference in the second test was solely due to the adsorption of CO_2.

Water: As a polar substance water will be adsorbed by any zeolite. To estimate the absolute amount the following experiment was performed: Approximately 100 ml of distilled water were poured over 140 g of zeolite. Immediately the zeolite beads adsorbed most of the water, thereby changing their colour. Then the beads were put under a fume hood for 2 hours. Now the remaining water had gone and the original colour of the zeolite beads returned partly. Subsequently an empty filter case was filled with these zeolite beads. When the weight was determined an increase of $\Delta m_{water} = 78$ g with respect to a filter filled with dry zeolite beads was measured. Again the filter was flushed with dry nitrogen at 1 l/min. The removal of water required a lot more time. After 24 hours only 25 g water were released.

Status at filling time: In order to estimate the impurity level of the gas system, the weight of the filter is measured at its production time. But this weight depends on the amount of already adsorbed gases and/or vapours. Air is composed mainly of nitrogen, oxygen and argon. These substances are not adsorbed in large amounts[4]. The next frequent constituent of air is water as humidity. To estimate the impact of humidity on the filter weight the following experiments were made (see also Fig. 7.9):

- Flushing a filter after its production with about 10 m^3 of nitrogen results in a filter weight $0.7 - 1.0$ g below the production weight. Hence the zeolite beads, filled into the filter cases, contain already little amounts of water (black in Fig. 7.9).

[4]Oxygen is similar to nitrogen in its structure and molecular weight. Hence the adsorption of both substances can be estimated to 0.2 g in total at atmospheric pressure.

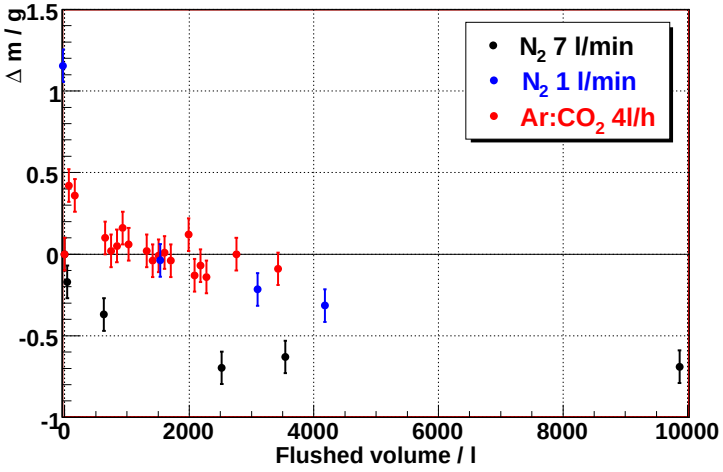

Figure 7.9: *At production time, little amounts of water are already accommodated in the zeolite. They can be removed by flushing with dry gases. When using Ar:CO_2 (red) the filter will adsorb CO_2 in the beginning. The blue data points correspond to a filter wrongly sealed after its production. Hence 1.3 g of additional water were accumulated within 7 month.*

- One filter was left open after its production. Within 7 month its weight increased constantly up to 6 g. The amount of the weight gain and the fact, that the removal by flushing the filter with dry nitrogen required a lot of time, revealed the additional weight as water.

- Normally the filters are sealed after their production. But some filters were sealed with wrongly designed closures on the gas outlet side. These filters increased their weight constantly to about 1.3 g after 7 month. This time the removal of the additional weight by flushing with nitrogen proceeded quicker, because the water could only enter the filter from one (the gas outlet) side (Fig. 7.9, blue data points).

- One filter was flushed with Ar:CO_2 at a low flow rate of 65 ml/min immediately after its production. Its weight increased quickly by about 0.5 g due to the adsorption of CO_2. But after a few days, a weight slightly below the weight at production time was reached (see Fig. 7.9, red data points).

Conclusions:

- The water content of the zeolite beads at production time Δm_W^0 is the key to a correct estimation of impurity levels when filters are exchanged. For Δm_W^0 a range of 0.7 to 1.0 g was found.

- When a filter is flushed, water is released in such an amount, that an equilibrium with the water content in the operating gas mixture is achieved.

7.4.5 Real condition tests

To verify the usability of the filter in the ATLAS MDT gas system, a test under real conditions was needed. Therefore a circulation system as shown in Fig. 7.10 was set up: Two filters were operated at 3 bar and flushed with Ar:CO_2 93 : 7 at a flow

rate of 8 l/min. After the outlet of the second filter the gas was compressed and forwarded with a diaphragm pump [74] to a buffer volume operated at 3.8 bar. The fixed delivery rate of the pump was higher than the required flow rate of 8 l/min. Hence part of the gas was bypassed. To compensate for leaks and to allow for a pressure regulation with p_1 and p_2, the setup was supplied with fresh gas at a low flow rate of $f_{in} = 50$ ml/min. With this setup most of the water, which is already contained in the zeolite beads at start-up, is circulated. Thus the filter weight should remain rather stable. The following experiments were performed:

Dust: Dust was a major concern when constructing the filter. If the zeolite beads rub against each other they can raise dust. Therefore the filter case is always completely filled with zeolite beads, so that no margin for movement is left. As a further precaution fine wire meshes were foreseen in the design. To estimate the dust production, one of the final ATLAS filters (filled with 118.3 g zeolite) was flushed with the setup described above (Fig. 7.10) at a flow rate of 8 l/min. The weight of the filter was checked regularly. Since most of the water from the zeolite beads is circulated, this experiment is not biased by water desorption.

Adsorption capacity and gas purity after the filter outlet: An approximate value for the adsorption capacity was already determined with the experiment described in the previous sections. The circulation system provided the possibility to check this value with Ar:CO_2 as working gas at the designated flow rate for the ATLAS MDT muon chambers. Additionally the outlet purity of the filter could be checked. For these measurements an impurity level of ≈ 1.7 ppm HMDS was inserted in front of the first filter. The second filter, put in series, measured the purity of the gas after the outlet of the first filter.

Results: The result of all measurements is shown in Fig. 7.11. Several important parameters of the filter were measured:

- In the start-up phase the weight of both filters increases by about 0.5 g within a few hours. This is due to the adsorption of CO_2 from the gas mixture.

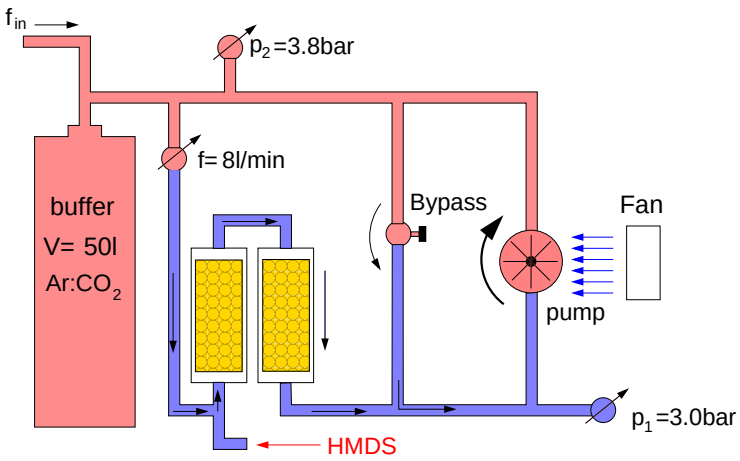

Figure 7.10: *Schematic setup of the circulation system to simulate conditions as during ATLAS operation. This setup was used to determine the dust production (with and without adding HMDS), adsorption capacity and outlet purity.*

- For the first five days filter 1 was flushed without adding HMDS. During this period of time its mass remained constant within an uncertainty of 0.1 g. Hence the dust production of the filter is negligible. Further most of the water was still in the circulation loop.
- After 5 days, filter 2 was added in series and the contamination with HMDS was started. The weight of filter 1 increased immediately, whereas the weight of filter 2 decreased by 0.2 g within 46 days (t_1 in Fig. 7.11). The weight reduction is presumably due to the slow release of water from the circulation loop.
- This measurement can be used to estimate an upper limit for the gas purity after the outlet of filter 1. Assuming a weight increase for filter 2 of less than 0.1g one can give the concentration of HMDS after the outlet of filter 1 to:

$$c_{out} = \frac{0.1\text{g} \cdot V_{mol}}{46\text{days} \cdot m_{mol} \cdot f} \leq 30\text{ppb} \tag{7.12}$$

  with V_{mol} = 22.4l/mol, the molecular weight of HMDS m_{mol} = 162.4 g/mol and f = 11520 l/day.
- At t_1 filter 1 had adsorbed ≈ 5.5 g of HMDS. The rate of its weight increase was in perfect agreement with the expectation (in blue), calculated from sensor data provided for the HMDS source.

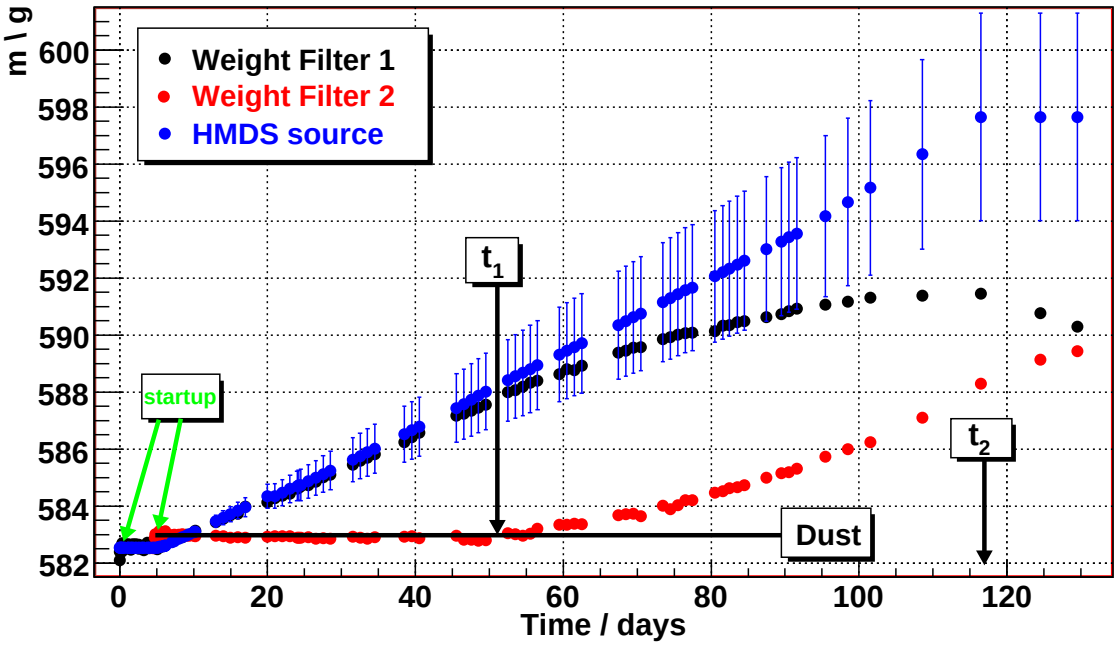

Figure 7.11: *Weight of the two filter (black and red) during the test at real conditions. The estimated mass increase based on HMDS sources sensor data is shown in blue. During the start-up water and CO_2 were adsorbed until the filter had adapted to their concentrations in the gas flow. At t_2 the HMDS source was switched off.*

- After t_1 filter 1 still adsorbed HMDS, but some molecules were capable to pass the filter. Nevertheless the sum of the weight increases in both filters still fits with the expectation.
- At t_2 the HMDS source was switched off to keep the circulation pump free from impurities. Now the concentration of HMDS in the inlet of filter 1 became zero. Thus HMDS molecules, adsorbed previously (at 1.7 ppm), were released again to the gas. These impurities were immediately adsorbed by filter 2.

As the most important result the adsorption capacity for HMDS could be determined to 5.5 g. Additionally the gas mixture after the outlet of a gas filter contains less than 30 ppb HMDS.

7.4.6 CO_2 and water adsorption during operation

The experiments described so far already revealed the amount of absolutely adsorbed CO_2 and water. But for the operation of the MDT chambers after the filters, the change of the water and CO_2 content with time is also important. Both contents have an impact on the maximum drift time (Section 2.2.2) and thus on the precision of the MDT muon system.
From the Langmuir equation Eq. 7.3 it is known, that the ratio of adsorption rate to desorption rate K depends on environmental parameters like the temperature. Hence the total amount of adsorbed water and CO_2 can vary if temperature changes occur. To estimate the release of water and CO_2 due to temperature changes intensive tests were carried out:

Heating the filter: To measure the CO_2 adsorption and desorption rate of the zeolite, a drift tube was supplied with Ar:CO_2 via a prototype filter, filled with 65 g of zeolite, at a flow rate of 66 ml/min. Around the filter case a heating wire was wrapped to vary the temperature of the filter. Then the pulse height of the drift tube close to the gas inlet was monitored while the temperature was changed at three different heat rates. The result of the pulse height scans is shown in Fig. 7.12. Fitting the pulse height minimum with a Gaussian distribution for every heating period results in the values given in Tab. 7.2: A pulse height reduction of 1.1% per $\frac{K}{h}$ was obtained as maximum.
To translate this relative value into an absolute release of CO_2, the experimental setup was modified: The filter was removed from the setup and CO_2 was added manually to the gas mixture at a rate of $f_{add} = 0.75$ mg/min. This caused a pulse height drop of $R_0 = 11.5\%$ with respect to Ar:CO_2 93 : 7. Taking into account the higher zeolite weight in the final ATLAS filter, one ends with the following estimation for the absolute CO_2 release per K/h:

$$\frac{dm_{rel}}{dt} = \frac{R}{R_0} \cdot 1\frac{\mathrm{K}}{\mathrm{h}} \cdot f_{add} \cdot \frac{m_{final}}{m_{prot}} \leq 0.15\frac{\mathrm{mg}}{\mathrm{min}} \tag{7.13}$$

At a flow rate of 8 l/min (ATLAS), the filter is flushed with CO_2 at a rate of 1.1 g/min. Hence the CO_2 release due to temperature effects is negligible except for

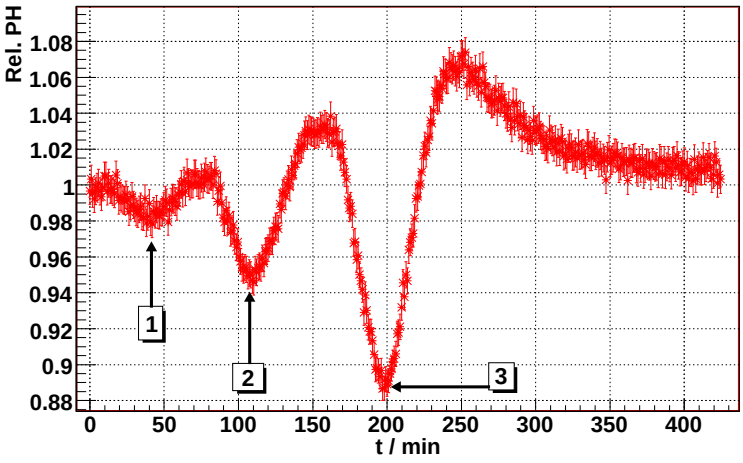

Figure 7.12: *Relative pulse heights versus time as measured when the filter was heated at three different rates. The numbers in the boxes denote the different heating periods listed in the first column of Tab. 7.2.*

Period	Δ T	Δ t	% change	change rate R
1	+0.7 K	37 min	−1.25%	1.10% /(K/h)
2	+1.95 K	25 min	−4.6%	0.98% /(K/h)
3	+5.1 K	31 min	−10.8%	1.09% /(K/h)

Table 7.2: *Relative change of the pulse heights when the filter was heated. The values in the last column give the relative change of the pulse height, determined by fitting the minima of the pulse height in Fig. 7.12*

rapid temperature changes.

Drift time measurements: To estimate the adsorption and desorption rates of CO_2 a pulse height scan is sufficient. To determine the impact of a changing water content due to temperature changes, the drift time can be measured. This was done with two different setups:

ATLAS gas monitoring system: To monitor the gas quality for the ATLAS MDT muon chambers a monitor chamber was built in Freiburg [75]. With this device the gas composition can be checked by measuring the drift time of electrons, released with a laser beam via the photo effect.
To estimate the impact of the zeolite on the drift time, 10 g of zeolite were put in a stainless steel case and mounted into the gas distribution line in front of a drift tube (Fig. 7.13, left). This drift tube was previously used to demonstrate the working principle of the monitor chamber. For this purpose a hole was drilled into the tube wall and sealed with a crystal window. With a pulsed laser beam, UV-light of 266 nm wavelength was transmitted through this window. Hereby electrons were released on the opposite side of the aluminium tube wall. The time difference Δt between the trigger signal of the laser pulse and the signal from an amplifier connected with the drift tube was used as a measure for the drift time. The drift tube was operated at 3 bar with a flow rate of 20 ml/min. Subsequently the stainless steel case was heated with a heat gun within 5 minutes from 21°C to 37°C. The temperature was

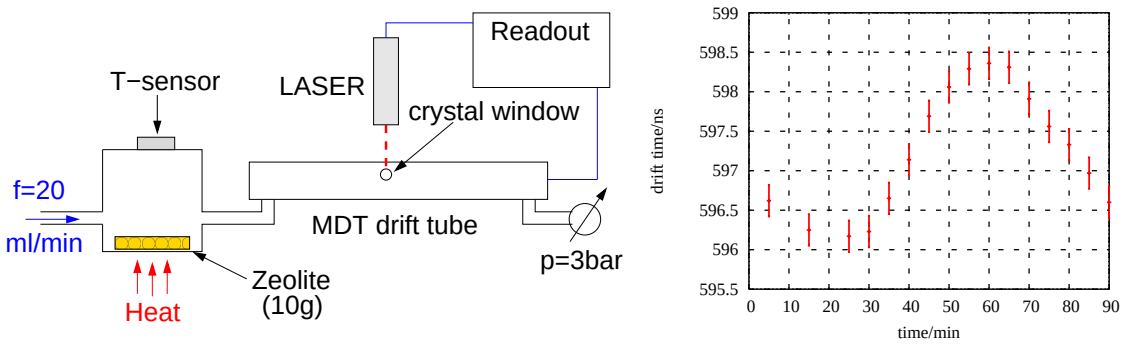

Figure 7.13: **Left:** *Setup used to measure the change of drift times due to temperature changes of the zeolite.* **Right:** *A rise in the drift time of only 2 ns was observed, although the temperature change was rapid.*

measured on the opposite side of the case. Afterwards the case cooled down to room temperature. The recorded time differences Δt are shown in Fig. 7.13 (right): Although the temperature change was rapid, the drift time increased only by 2 ns. Further, the drift tube was operated at a flow rate of $\frac{1}{300}$ the flow rate at ATLAS. With a total zeolite weight of $\frac{1}{12} m_{ATLAS}$ a factor of 25 remains for the dilution of the measured effect. Hence a change of the drift time in the order of $\Delta t < 0.1$ ns can be estimated from this measurement.
However, it can not be said how much of the heat actually reached the inside of the case. Additionally the effects could be bigger if the gas is flushed through the zeolite. Nevertheless, the result of this measurement allows to exclude rapid drift time changes due to the zeolites in the gas system.

MDT prototype chamber: For the work concluded in [76] a MDT prototype chamber, consisting of 3×8 drift tubes, was built. The prototype chamber features a parallel gas distribution system and pre-series front end electronics. With a plastic scintillator, mounted above the prototype chamber as trigger close to the gas inlet, drift time spectra of cosmic muons were acquired. The chamber was operated at 3 bar and supplied with Ar:CO_2 at a flow rate of 80 ml/min. Before the gas entered the on-chamber gas distribution system it was flushed through a case containing 10 g of zeolite. Again the zeolite was heated rapidly to cause a change of the gas mixture, while the drift times of all 24 tubes were recorded continuously. In this way drift time spectra as shown in Fig. 7.14 were obtained. The following two functions were fitted to the falling and rising edge of the spectra:

$$N_{rise}(t) = \frac{A}{1 + \exp\left[-B \cdot (t - t_0)\right]} \tag{7.14}$$

and

$$N_{fall}(t) = \frac{A + C \cdot t}{1 + \exp\left[-B \cdot (t - t_1)\right]} \tag{7.15}$$

The difference of the times t_1 and t_0, determined in the fit, is called the maximum drift time. As a consequence of a changing gas mixture the maximum drift time will

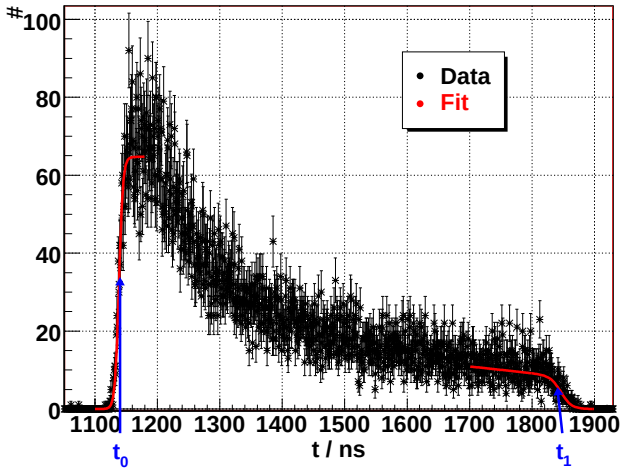

Figure 7.14: *Drift time spectrum recorded with the MDT prototype chamber. Two functions are added to the plot. The rising edge of the spectrum was fitted with Eq. 7.14, the falling edge with Eq. 7.15. The time difference* $\Delta t = t_1 - t_0$ *is called the maximum drift time.*

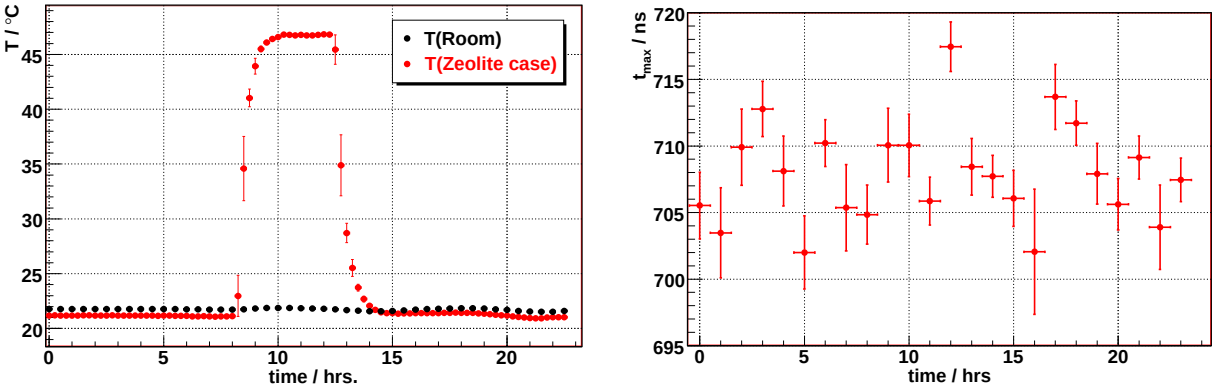

Figure 7.15: *In the left plot the temperature measured on the outside of the zeolite case is shown. The right plot shows the corresponding maximum drift time as measured with the MDT prototype chamber. The impact on the maximum drift time can be seen hardly, although the temperature increase was huge.*

also change. In Fig. 7.15 the temperature (left) of the zeolite case and the measured maximum drift times (right) with the MDT prototype chamber are plotted for one day. With a delay of about 4 hours a small change of the drift time in the order of a few ns can be recognized. The ratio of zeolite weight to flow rate gives a factor of 8 compared to what is expected at ATLAS. Thus the impact of the zeolite on the maximum drift time was confirmed to be negligible.

Remark: The drift time measurements were performed with un-humidified gas from bottles. Therefore the water content of the gas mixture was in the order of 100 ppm. The amount of released water will therefore be higher at ATLAS, where a water content of 600 ppm is desired. With respect to the huge safety margin and the stable temperature conditions in the ATLAS pit 100 m underground, no problems are expected. A further positive impact is given by the slow release of water measured in section 7.4.4.

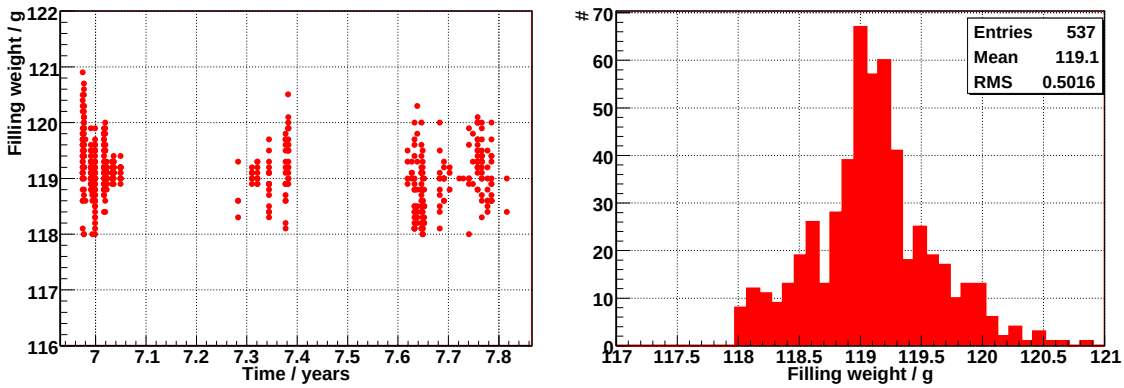

Figure 7.16: **Left:** *Weight of the zeolite filling as a function of the production time: The weight remained constant.* **Right:** *Distribution of filling weights. In average* 119.1 *g of zeolite could be filled into a filter case. The required minimum filling weight of* 118 *g can be seen clearly as cut-off in the distribution.*

7.4.7 Summary

From all measurements described in this section the following important results are summarized:

- With a pressure drop of less than 5 mbar the filter can be used at ATLAS without problems.
- When drift tubes were supplied with highly contaminated gas over the filter, no ageing effects were observed.
- In several different tests the adsorption capacity of the zeolite filter to the silicone HMDS was tested. For the ATLAS MDT gas filter an adsorption capacity of ≈ 5.5 g HMDS was measured.
- The gas mixture after the filter outlet contains less than 30 ppb of impurities up to an adsorbed weight of 5.5 g HMDS.
- The zeolite beads in the filter do not raise dust.
- The impact of the filter on the drift time seems negligible. This was shown with several different experiments. The filter changes the gas mixture only if rapid temperature changes occur.

7.5 Filter production and usage in ATLAS

For the use in the ATLAS MDT gas system 272 filters are required; one for each gas channel. They will be replaced regularly to minimize the risk that impurities reach the muon chambers. In addition the actual impurity level of the gas system is monitored by analysing the exchanged filters.

7.5.1 Filter production and installation

A total of 537 filters was produced in Freiburg between November 2006 and September 2007. The required filling weight of zeolite beads in a gas filter is 118 g, in average 119.1 g were achieved. The distribution of the filling weights and their independence from the time of production is shown in Fig. 7.16. After their filling the filters were sealed with aluminium screwings until they will be installed at ATLAS. A picture of filters already installed on top of a gas distribution rack is shown in Fig. 7.17. For the first run only 272 filters are required. The remaining filters are stocked until they will be needed for the first exchange.

7.5.2 Exchange procedure

With the measurements described in section 6.4 it was found that the impurity level is highest in the beginning. Thus the filter will accumulate most volatile compounds during the first time of the ATLAS MDT chamber operation. Consequently an exchange of all filters is recommended for the first shut-down periods.
The old filter bodies are then unmounted as described in section 7.3.2 and replaced by new ones. The connectors with the brass screwing will remain in place so that a quick exchange is possible. In the following the removed filter bodies will be sealed with aluminium screwings and brought to Freiburg.

7.5.3 Determination of the impurity level

The removed filters will be used to estimate the impurity level in the gas system. As an important premise the filters have to be closed subsequent to their deinstallation to avoid the adsorption of water from air moisture. From the measurements described in Section 7.4.4 it was learned that two effects have to be considered: The filter weight will increase by 0.5 g due to the adsorption of CO_2. At the same time an unknown amount ΔM of water, that depends on the water content of the operating

Figure 7.17: 12 *Filters on top of a gas distribution rack for the ATLAS MDT gas system. One can see the connections to the gas rack (lower connections) and to the copper pipes (upper connections). The copper pipes which are connected to the gas rack without a filter are the return pipes from the MDT chamber outlets.*

gas mixture, will have been released. The range of ΔM spreads from 0 g, in case of a very humid gas mixture, to 1 g for a very dry gas mixture. Thus the filter weight will change by 0.5 g at most, if the gas system is free from impurities. For a gas mixture with an average humidity the weight of the filter should be identical with the weight at production time ($+0.5g$ due to the adsorption of CO_2 and -0.5 g due to the release of water).
The following procedures are defined to determine the impurity level in the gas system:

- If the filter is less than 0.5 g heavier compared to the weight at production time, the impurity level is compatible with zero.
- If the weight of the filter has increased by more than $\Delta m = 0.5$ g the impurity level can be estimated with the following formula (equivalent to HMDS):

$$c_{Si} = \frac{\Delta m}{162.38\text{g/mol}} \cdot \frac{22.4\text{l/mol}}{\bar{f} \cdot t} \approx 0.138\frac{\text{l}}{\text{g}} \cdot \frac{\Delta m}{\bar{f} \cdot t} \tag{7.16}$$

  where t is the flushing time with an average gas flow rate $\bar{f}$. The uncertainty of this estimation is (with $\sigma_{\Delta m} = 0.5$ g) :

$$\sigma_c = \frac{0.07\text{l}}{\bar{f} \cdot t} \tag{7.17}$$

However, for the filters currently in operation this method can not be applied. The reason is explained in the following section.

7.5.4 Uncertainties determined by production flow

When the ATLAS MDT gas filters were produced in Freiburg, their weight was determined with a balance and written to a database (Appendix C). The reading of the balance was done manually, which is fault-prone. When checking carefully the weight of 12 filters from the series production errors were found: It occurred four times, that the weight of the filters in the database was wrong by 1 g. Such a cross-check of the filter weight was not performed before the filters were shipped to CERN. Consequently about one third of the filters installed currently at CERN are registered with a wrong weight. Nevertheless, errors larger than 2 g are very unlikely, since the weight of the filling has to be in a certain range to be accepted. This is checked by the software used during the filter production.
The impact of the human factor was clearly underestimated. To avoid this for the future two possible solutions are conceivable: Either the weight has to be cross-checked any time after the filter production, or the weight has to be measured with a balance with an electronic interface.
Thus the possibility to determine impurity levels is not possible with the filters currently installed in the MDT gas system. Only if an exceptionally high filling weight is found after an exchange, one can assume that impurities are the reason for that. Other possibilities are given by statistical methods, for example if one looks at the weight distribution of several filters after an exchange.

7.5.5 Exchange intervals

With the ATLAS detector, data will be collected only during half of the time of a year. In the remaining time, when no proton-proton collisions will occur, maintenance tasks of detector components will be performed. In these intervals an exchange of filters will be possible. With a total adsorption capacity of 5.5 g for HMDS, a filter can be operated with a maximum impurity level of 350 ppb at a flow rate of 8.3 l/min (the average flow rate for the gas channels supplying MDT chambers in the barrel) for 180 days. As a precaution a filter should be exchanged if its weight has increased by

$$\Delta m \geq 3\text{g} \tag{7.18}$$

during operation. From measurements will real contaminations (section 6.4), it is known that the impurity level will decrease with time. This is of course only true if impurities are not newly introduced during the maintenance periods. Hence a continuous replacement of some filters in the shut-down periods is suggested. That way the actual impurity level can be measured and thus the exchange intervals can be adapted.
For the reason described in the previous section the impurity level at the start-up of ATLAS has to be estimated with different methods. Presumably it will only be possible if a rather high impurity level occurs. Therefore an exchange of all filters is recommended for the first shut-down.

7.5.6 Experiences from first test runs

In November 2007, after the *M4* test run[5], six filters were exchanged. Thus the actual impurity level of the gas system was checked; further the exchange procedure was tested. The replaced filters were already installed in December 2006. At the time of deinstallation they were operated for half a year with a gas flow rate of ≈ 8.3 l/min. During this time the gas was taken from bottles, without adding or checking

[5] A test of part of the muon system with cosmic muons.

Number	weight before	weight after	difference	Impurity level Eq. 7.16
37	584.2 g	584.3 g	+0.1 g	-
38	584.4 g	584.6 g	+0.2 g	-
57	577.5 g	577.6 g	+0.1 g	-
65	573.9 g	575.1 g	+1.2 g	77 ± 32 ppb ??
67	576.5 g	576.9 g	+0.4 g	-
74	584.7 g	585.9 g	+1.2 g	77 ± 32 ppb ??

Table 7.3: *Mass gain of* 6 *filters operated under real conditions in the ATLAS pit. For two gas channels impurity levels are given. These levels were calculated with Eq. 7.16 assuming an operation time of* 180 *days and a flow rate of* 8.3 *l/min. Anyhow, these impurity levels have to be doubted due to the uncertainties described in section 7.5.4.*

the desired amount of 600 ppm water.
According to [77] no problems with the gas mixture due to the filters were reported. In general no filter related problems were reported.
After the replacement of these six filters their weight was determined. The result can be found in Tab. 7.3: Two filters showed a significantly increased weight which could not be explained due to the adsorption of CO_2 and water. Since all six filters were operated in parallel, it is unlikely that only two of them became heavier due to impurities in the gas system. It is more likely that the additional weight is due to the errors in the weighing procedure (Section 7.5.4). Filter number 65 was given to a chemical analysis to verify this assumption.
Subsequently two filters were flushed with dry nitrogen. After a few minutes their weight was reduced by 0.5 g (CO_2 adsorption from the operating gas mixture). In the end, after being flushed with more than 5000 l of nitrogen, their weight has been reduced by 0.9 g and 1 g respectively. Thus the results described in section 7.4.4 were confirmed with filters that were in operation for some time at CERN. The properties of the ATLAS MDT gas filters are therefore well understood.

Chapter 8

Summary

The ATLAS muon spectrometer is a detector with a very ambitious goal: The tracks of muons from the interaction point are to be measured with an absolute precision of 50 μm within a volume with a length of 40 m and a diameter of 25 m.
Monitored Drift Tube (MDT) chambers are used predominantly as precision device for these measurements. The drift tubes in these chambers are operated with a gas mixture of argon and CO_2 in a ratio of 93 : 7. This gas mixture was selected because ageing effects had been observed with the desired gas mixture containing CH_4. Ageing effects make a reliable operation of the drift tubes impossible and reduce the precision of the MDT chambers significantly. These undesired effects were also observed with Ar:CO_2 as operating gas mixture; they were then caused by tiny amounts of impurities in the gas system. These impurities are deposited on the anode wire where they change the electric field. Silicon compounds were either found in these deposits or assumed to be the reason for the observed ageing effects. When a circulation pump was tested for the use in the ATLAS gas system, ageing effects were observed after a short time. They could be clearly attributed to silicon compounds, contained in components previously used in other experiments for many years without causing trouble. Therefore it was concluded that the ATLAS gas system had to fulfil stricter cleanliness requirements than any other particle physics experiment before. Consequently ageing tests with gas system components were planned, to avoid silicon compounds in the gas system.
For this purpose a new ageing experiment using drift tubes was designed and assembled in Freiburg. With 38 drift tubes in total several components could be tested in parallel. The drift tubes were irradiated with photons with an energy of E= 59.5 keV from nine ^{241}Am-sources. To test the long term properties of a drift tube when irradiated with a different type of radiation, an ageing test with an α-source was also set up. Furthermore, systematic studies with a well defined impurity level of silicon compounds were carried out. With different operation parameters, such as flow rate, high voltage or irradiation density, their impact on the extent of the drift tube deterioration could be determined qualitatively.
During ATLAS operation a counting rate of up to 1.5 kHz/cm is expected from simulations at the maximum (including a safety factor of 5). With this counting rate the drift tubes will collect an integrated charge of 0.6 C/cm during 10 years of

ATLAS operation. After this time the drift tubes should still be fully operational. In ageing studies carried out with the newly designed experiment, it was found that an impurity level well below 1 ppm will deteriorate the drift tubes significantly already after few months of operation.
Tests with components of the ATLAS MDT gas system were carried out; In particular a fully assembled gas distribution rack was tested. The outcome of this test was positive with respect to ageing effects. Again, silicon compounds were found to be the reason, the source of which was investigated in subsequent tests. As one source of impurities o-rings were found. These o-rings were used in the manifolds of the gas distribution rack. They were supplied by industry and were ordered silicone-free. This example showed that a different approach to avoid silicon compounds in the gas system is necessary: A filter for the gas system of the MDT chambers.
For this gas filter zeolites were used as active filter component. Intensive experiments were carried out to make sure, that the filter itself does not introduce new problems into the gas system. In particular the pressure drop, adsorption properties and the problem of dust was examined. In the end a filter with a high purity of the outlet gas mixture was built. The filter could adsorb up to 5.5 g of volatile silicon compounds from the gas mixture at the desired flow rate of 8 l/min.
Due to the limited adsorption capacity of the filter they have to be exchanged after some time. After their deinstallation the weight of these filters will be determined to estimate the impurity level in the gas system. These results will be used to adapt the exchange intervals in the future.
In total 537 filters were built in Freiburg. For the first run of ATLAS 272 filters were connected to the gas distribution lines to the MDT chambers. When six of these filters were exchanged recently, a rather low level of impurities in the gas system could be detected. Thus the ATLAS muon system is ready for exciting new physics without negative ageing effects.

Appendix A

Radiation distribution

In this appendix the current density distributions along the individual drift tubes mounted in the component test are shown. They were calculated with the Monte Carlo simulation described in chapter 5. The distributions are shown for the default source arrangement (section A.1) used throughout the component tests. In section A.2 the distributions for the studies with a different source arrangement and partly shielded tubes are shown.
The current density distributions shown in both sections were calculated with a mean gas gain of $\bar{G} = 2 \cdot 10^4$. The simulations were performed including space charge effects, calculated with the procedure described in 5.4.1.
To ease the comparison with results obtained in pulse height scans, the x-axis of the following plots is given in the coordinate system used throughout the pulse height scans. The inside of the brass box, where the drift tubes were irradiated, is located within a range from x= 100 . . . 1080 mm in this coordinate system. With a wall thickness of 10 mm, positions below 90 mm and above 1090 m are outside the brass box. The pulse heights obtained at the positions 0 mm and 20 mm served as reference in most measurements.

A.1 Source arrangement for the component tests

The current densities in this section were calculated for the source arrangement used throughout the component tests and for some of the earlier tests with HMDS. This refers to all results concluded in the section 6.4 and 6.5.1:
The current density distribution of some of the tubes show prominent peaks. The peak found at position 950 mm for tube number 11 can be clearly identified with the enhanced deterioration observed in the beginning of the studies with the Molykote 111 (Fig. 6.8).
Since the ageing experiment was set up symmetrically (Fig. 4.2, left), the current density distribution is identical for drift tube pairs of the outer (inner) layers. They are shown in Fig. A.1 for the outer layers, those for the inner layer are shown Fig. A.2. The tables Tab. A.1 and Tab. A.2, put below the figures, summarize the corresponding trigger rates, irradiation rates and current densities.

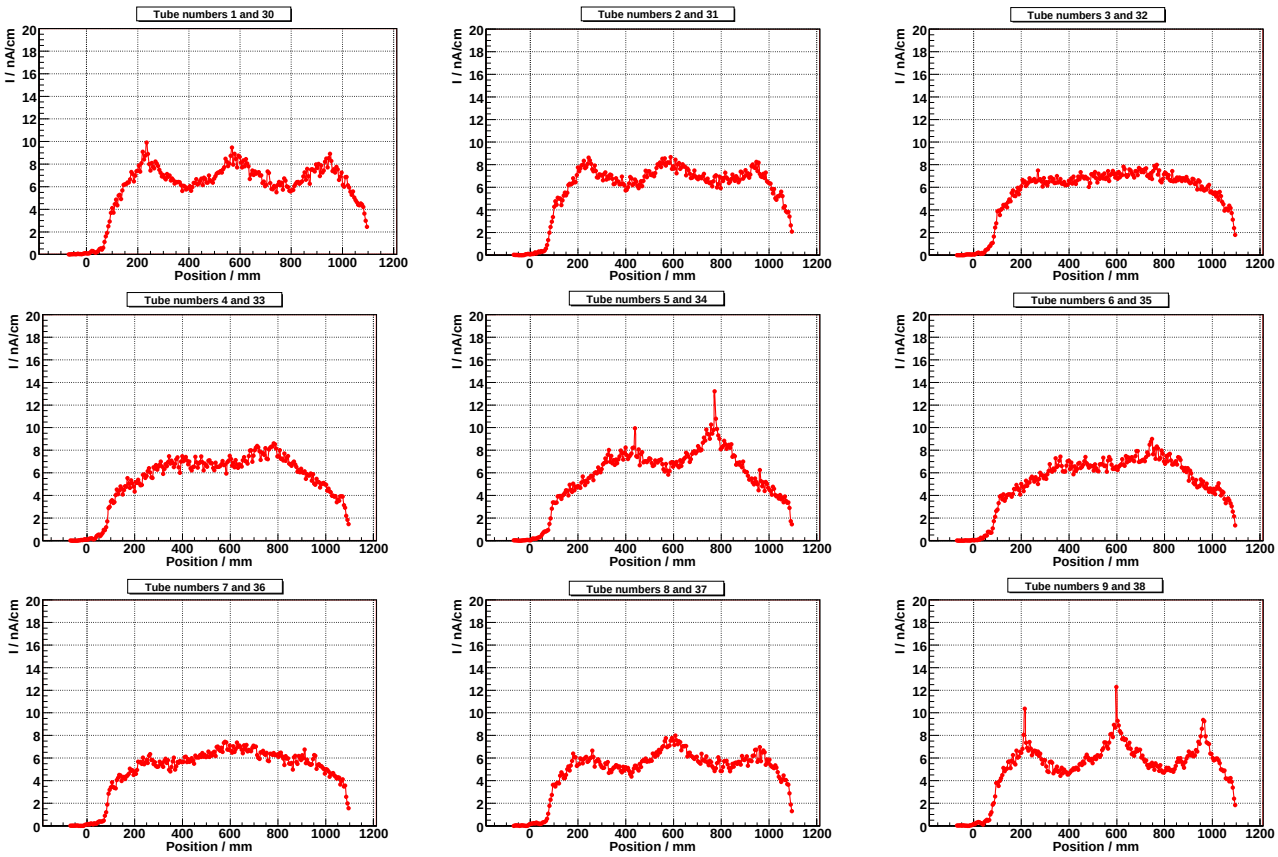

Figure A.1: *Current density distributions along individual drift tubes for the outer layers of the component test. These distributions are only valid for the measurements described in the sections 6.4 and 6.5.1. The given tube numbers are as defined in Fig. 4.2 (left).*

Tube numbers	Irradiation Rate (kHz)	Trigger Rate (kHz)	Current μA
1 and 30	186	151	0.68
2 and 31	188	151	0.68
3 and 32	174	141	0.64
4 and 33	167	135	0.62
5 and 34	178	144	0.65
6 and 35	161	130	0.60
7 and 36	152	124	0.57
8 and 37	151	122	0.57
9 and 38	161	131	0.60

Table A.1: *Irradiation rate, trigger rate and overall current for the drift tubes shown in Fig. A.1. The accuracy of the estimated trigger rates from the Monte Carlo simulation is about* 1%.

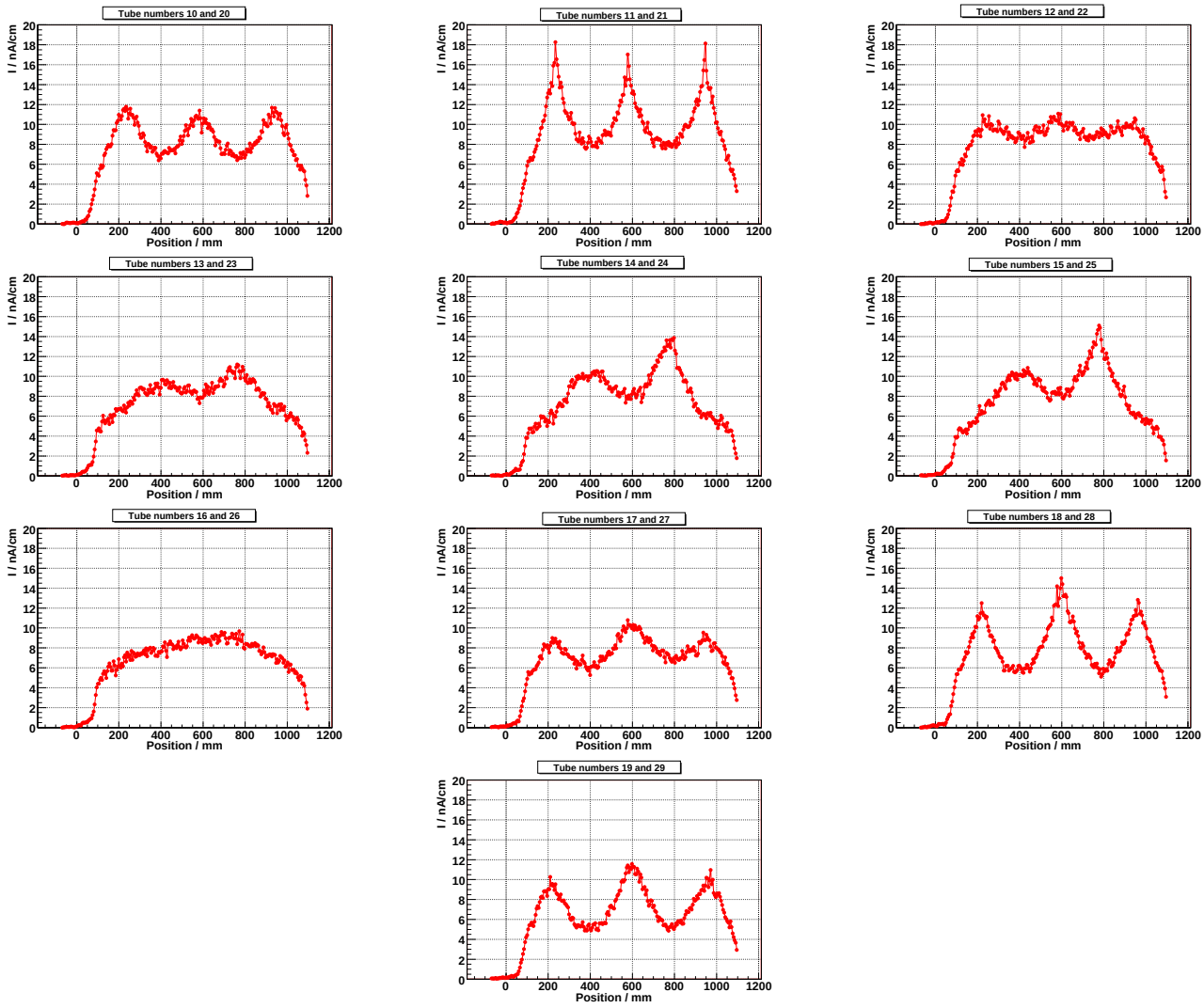

Figure A.2: *Current density distributions along the drift tubes of the inner two layers. They correspond to the same measurements as in Fig. A.1.*

Tube numbers	Irradiation Rate (kHz)	Trigger Rate (kHz)	Current μA
10 and 20	245	197	0.86
11 and 21	302	239	1.02
12 and 22	254	203	0.90
13 and 23	223	179	0.80
14 and 24	231	185	0.82
15 and 25	234	188	0.83
16 and 26	209	168	0.76
17 and 27	208	169	0.77
18 and 28	238	190	0.84
19 and 29	202	163	0.74

Table A.2: *Irradiation rate, trigger rate and overall current for the drift tubes shown above in Fig. A.2.*

A.2 Systematic studies

For the systematic studies described in 6.5.2 the radioactive sources were arranged slightly different. In addition parts of the drift tubes were shielded wit lead. A first, the rearrangement of the sources was done such, that a lower but more uniform irradiation of the tubes was achieved. The current densities obtained with this arrangement are shown in Fig. A.3 in black. Later, one source in the middle of the setup was moved closer to the drift tubes. Thus a highly non-uniform irradiation of the tubes was achieved. The resulting current density distributions are shown in Fig. A.3 in red. The corresponding currents, irradiation and trigger rates for both source arrangements are listed in Tab. A.3.

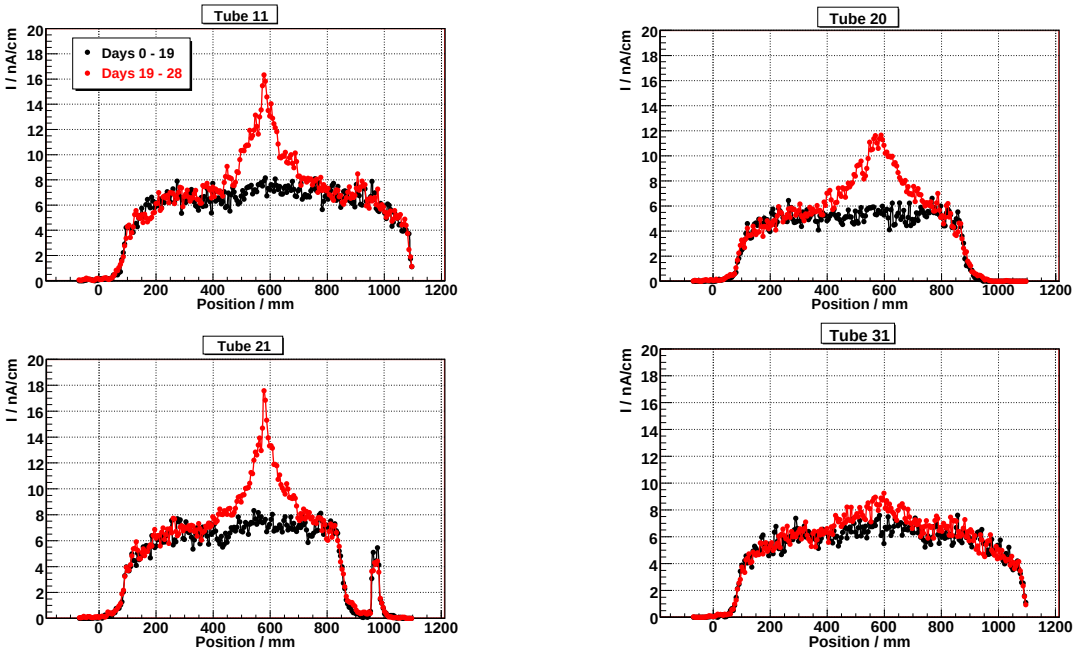

Figure A.3: *Current density distribution for the four drift tubes used for the systematic studies where some tubes were partly shielded with lead (section 6.5.2). After* 19 *days one source was moved closer to the drift tubes. The key, shown in the upper left plot, applies to all plots.*

Tube number	Irradiation Rate	Trigger Rate	Current μA
11	176 (215)	143 (171)	0.65 (0.76)
20	108 (142)	88 (115)	0.40 (0.52)
21	142 (183)	115 (146)	0.53 (0.65)
31	159 (171)	128 (139)	0.59 (0.63)

Table A.3: *Irradiation rate, trigger rate and overall current for the drift tubes shown in Fig. A.3. The values given in brackets correspond to the source arrangement where one source was positioned closer to the drift tubes (red points in Fig. A.3).*

Appendix B

Electronics

In this appendix, the impact of the front end electronics on the pulse shapes measured with the drift tubes is explained. The procedure is basically geared to [19] and [14]. For details one may look up these references. The ATLAS drift tube is treated as a coaxial transmission line with a vanishing transconductance. The electronics on the readout- and high voltage side allow (cause) a frequency dependent transmission (reflection) of the signal to (from) the readout side where the amplifier is located.

B.1 Wave impedance of the drift tube

The electrical resistance of the signal wire is generated by several effects. For low frequencies only the ohmic resistance is of importance. When the frequency increases, the current in the wire is confined to a thin layer near the wire surface (skin effect). At frequencies above 1 GHz leakage through the dielectric overcomes the skin effect. The whole dependence of $R(\omega)$ per unit length can be approximated as

$$R(\omega) = \left(\begin{array}{ll} \frac{1}{\pi\sigma a^2} + \frac{\sigma\mu_0^2 a^2\omega^2}{192\pi} & \text{for} \quad \omega < \frac{8}{a^2\sigma\mu_0} \\ \frac{1}{2\pi a}\sqrt{\frac{\mu_0\omega}{2\sigma}} + \frac{1}{4\pi\sigma a^2} + \frac{3}{32\pi a^3}\sqrt{\frac{2}{\sigma^3\mu_0\omega}} & \text{for} \quad \omega > \frac{8}{a^2\sigma\mu_0} \end{array} \right) \tag{B.1}$$

with the conductivity σ and radius a of the wire. The functional progression of $R(\omega)$ is shown in Fig. B.1 (left). With the inner drift tube diameter b, the capacitance C and inductance L per unit length

$$L = \frac{\mu}{2\pi} \cdot \ln\frac{b}{a} \qquad C = \frac{2\pi\epsilon}{\ln\frac{b}{a}} \tag{B.2}$$

the impedance Z_0 of the wire (neglecting the transconductance) can be calculated to:

$$Z_0(\omega) = \sqrt{\frac{L}{C} - i \cdot \frac{R(\omega)}{\omega \cdot C}} \tag{B.3}$$

For high frequencies the known behaviour $Z \to \sqrt{L/C}$ is obtained, see also Fig. B.1 (right). With the geometrical dimensions of a drift tube an impedance of 382 Ω is obtained.

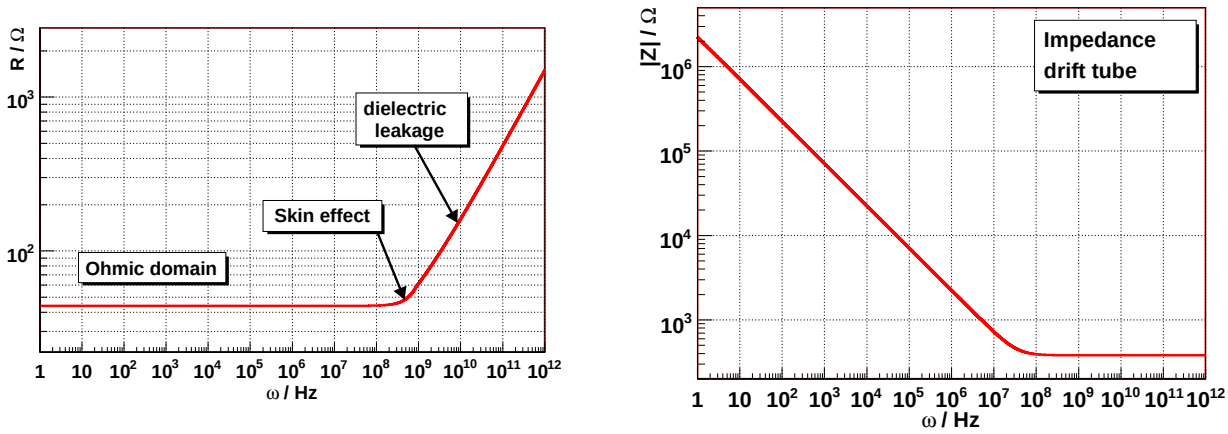

Figure B.1: **Left:** *Resistance of the drift tube wire per meter. The different effects contributing to the resistance are explained in the boxes.* **Right:** *Absolute value of the drift tube impedance, taking into account the capacitance and inductance of the tube as well as the resistance of the wire (Eq. B.3).*

B.2 Electronic components

In Fig. B.2 the electronic circuits on the readout and high voltage side of a drift tube in the ageing experiment are shown. With the Kirchhoff laws the impedances on both sides are determined to:

$$Z_{HV}(\omega) = \frac{R_1 + R_2 + i\omega R_1 R_2 (C_1 + C_2)}{1 + i\omega R_2 C_2} \tag{B.4}$$

$$Z_{RO}(\omega) = \frac{1 + i\omega R_3 (C_3 + C_4)}{i\omega C_3 - \omega^2 R_3 C_3 C_4} \tag{B.5}$$

The progression of both impedances is shown in Fig. B.3. The values of the resistors and capacitors are:

$$R_1 = 1M\Omega \quad R_2 = 332k\Omega \quad C_1 = 10\mu F \quad C_2 = 100nF \tag{B.6}$$

and

$$R_3 = 360\Omega \quad C_3 = 1nF \quad C_4 = 68pF \tag{B.7}$$

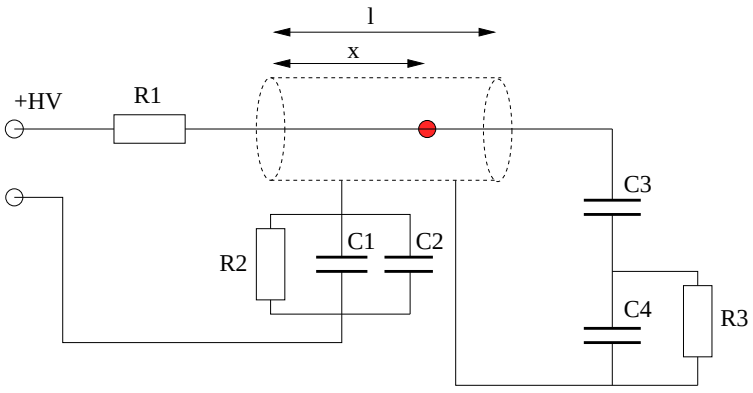

Figure B.2: *Electronic components connected to the drift tube for HV supply and signal readout. R_3 includes the adaptation resistor and the AC impedance of the amplifier of $Z \approx 30\Omega$ [40]. The red mark denotes the position x where the signal is generated.*

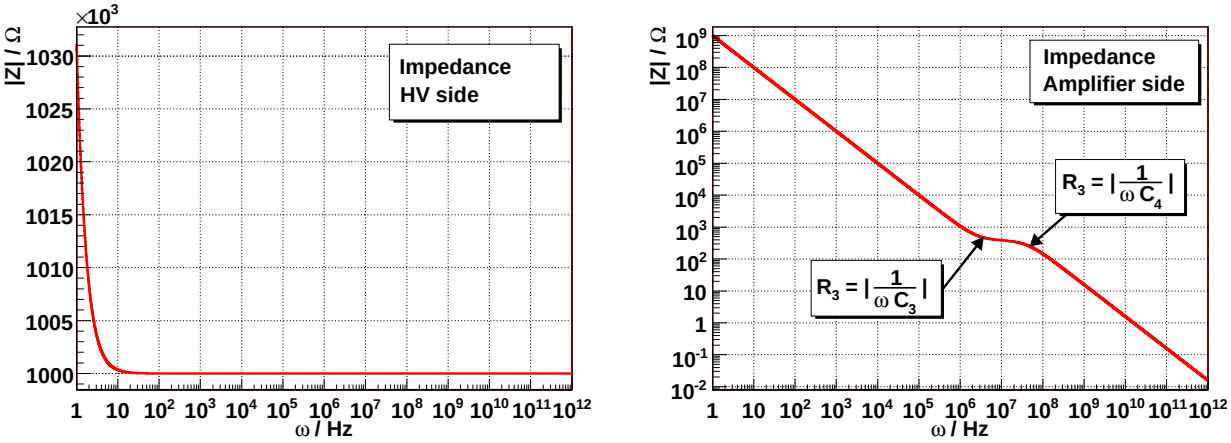

Figure B.3: *Impedances of the electronic circuits.* **Left:** *On the high voltage side R_2 is bypassed via C_1 and C_2 already for frequencies below 10 Hz. Hence the impedance is mainly given by R_1.* **Right:** *On the readout side the impedance is driven by R_3 and C_3 for frequencies below 1 MHz. For frequencies above 40 MHz the signal is mainly bypassed from the amplifier via C_4.*

B.3 Transfer function

B.3.1 Impedance matching

When the impedances of the drift tube and the electronics on the readout side match exactly for all frequencies, the signal is completely transferred to the amplifier. By looking at Fig. B.1 and Fig. B.3 one immediately realizes that this is not the case for the drift tubes in the ageing experiment. Thus part of the signal is reflected. The reflection (ρ_i) and transmission (τ_i) coefficients are:

$$\rho_i = \frac{Z_i - Z_0}{Z_i + Z_0} \qquad \text{and} \qquad \tau_i = 1 - \rho_i \tag{B.8}$$

where i stands either for "RO" or "HV". Note that all quantities are frequency dependent complex numbers.

B.3.2 Wave propagator

The propagation of the signal along the drift tube wire is expressed by the following "propagator":

$$P(x) = e^{[ik(\omega) - \alpha(\omega)]\cdot x} \tag{B.9}$$

where $k(\omega)$ describes the oscillating behaviour and $\alpha(\omega)$ the attenuation of the signal. From [14] it follows that:

$$\alpha(\omega) = \sqrt{\frac{1}{2}\Big(\omega^2 LC + \omega C\sqrt{R^2(\omega) + \omega^2 L^2}\Big)} \tag{B.10}$$

and

$$k(\omega) = \sqrt{\frac{1}{2}\Big(-\omega^2 LC + \omega C\sqrt{R^2(\omega) + \omega^2 L^2}\Big)} \tag{B.11}$$

B.3.3 The Transfer function $\Psi(\omega)$

The transfer function describes that part of the signal, that reaches the amplifier. If a signal is created at position x, as shown in Fig. B.2, it splits into two halves to both sides of the drift tube (length l). For the part of the signal travelling directly to the amplifier side the transfer function is:

$$\Psi_1 = \frac{1}{2} P(l-x) \cdot \tau_{RO} \tag{B.12}$$

The other half of the signal has to be reflected on the high voltage side to reach the amplifier. For this the following transfer function holds:

$$\Psi_2 = \frac{1}{2} P(x) \cdot \rho_{HV} \cdot P(l) \cdot \tau_{RO} \tag{B.13}$$

Since the transmission coefficient on the amplifier side is not 1 for all frequencies, parts of the signal are always reflected. These parts travel along the wire several times before they are extracted or attenuated. Hence the final transfer function is a sum of infinite many transfer functions as in Eq. B.12 and Eq. B.13. The infinite sum yields:

$$\Psi(\omega) = \frac{1}{2} \tau_{RO}(\omega) \cdot P(l-x) \frac{1 + \rho_{HV} P(2x)}{1 - \rho_{HV} \rho_{RO} P(2l)} \tag{B.14}$$

The transfer function in Eq. B.14 depends on two parameters: The frequency ω of the signal and the position x along the wire where the signal was created.

The role of C_4: Not all of the signal current, extracted on the read out side is passed to the amplifier. Part of it is bypassed via C_4, especially at high frequencies. Taking this into account one arrives at the final transfer function describing the signal propagation to the amplifier input. This function is shown in Fig. B.4.

B.4 Examples

The following examples illustrate the abstract object "transfer function".

Signal created in the middle:
If a signal is created in the middle of the drift tube the transfer function in Fig. B.4 is obtained. In a frequency range between 600 Hz and 70 MHz more than half of the signal is transferred to the amplifier. Below 600 Hz most of the signal is extracted on the high voltage side, where the current measurement is performed. The signal parts with higher frequencies than 70 MHz are bypassed to ground via C_4. From Fig. B.1 and Fig. B.3 (right) it can be seen that the impedances of the drift tube and the amplifier side match quite well around 10 MHz.
At $\omega \approx 370$ MHz the denominator in Eq. B.14 becomes close to zero. The reason is a resonance of the tube, so that the product of the complex quantities ρ_{RO}, ρ_{HV} and $P(2l)$ becomes real and close to 1. Only the attenuation factor $\alpha(\omega)$ in $P(2l)$ (Eq. B.9) prevents from a higher resonance amplitude. Noise signals with a frequency around $\omega \approx 370$ MHz are therefore likely.

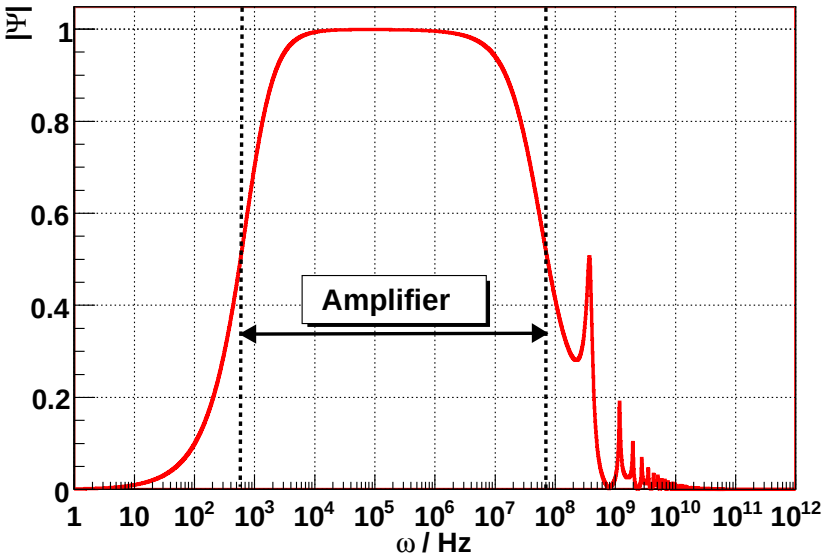

Figure B.4: *Transfer function* $|\Psi(\omega)|$ *obtained for a signal generated in the middle of the drift tube. At low frequencies most of the signal is extracted on the high voltage side (current measurement). At frequencies above* 70 *MHz the signal is bypassed via* C_4.

Signals created at the tube ends:
When a signals is created close to the tube's end plugs, the transfer function does not really change, see Fig. B.5. The reason is, that most of the signal is reflected on the high voltage side. The value of a pulse height, obtained in pulse height scans, does therefore not depend on the position along the drift tube. Thus a pulse height correction is not needed.

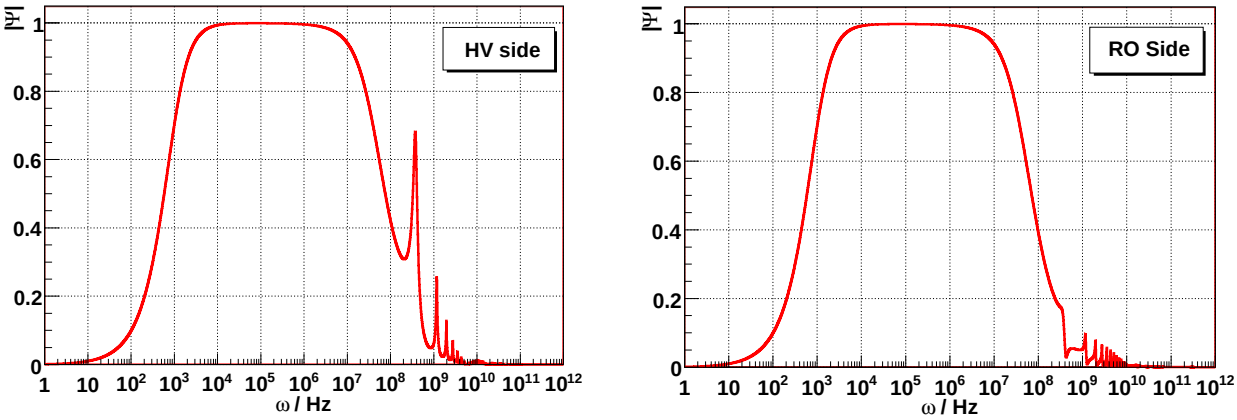

Figure B.5: *When signals are created close to the end (***Left:** *high voltage side,* **Right:** *readout side) of a drift tube, the shape of the transfer function in an interval from* 600 *Hz to* 70 *MHz is preserved. Only the resonance at* $\omega \approx 370$ *MHz changes its position and height.*

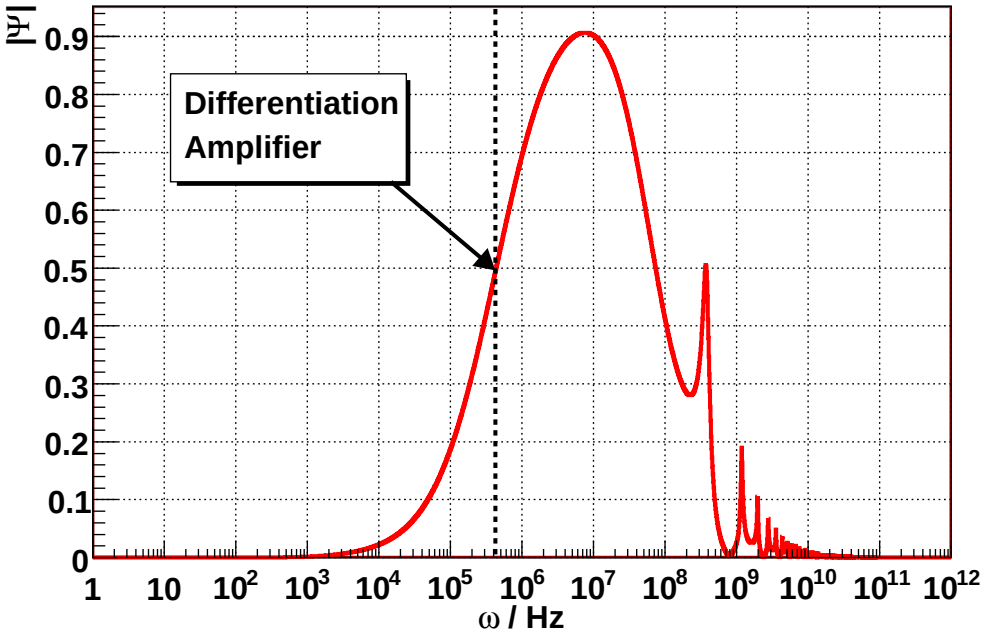

Figure B.6: *Final transfer function* $|\Psi(\omega)|$ *taking into account the RC differentiation element in the amplifier. Frequencies below* $\omega = 430$ *kHz are suppressed significantly.*

B.5 Amplifier

The amplifier also changes the pulse shape. The part in the amplifier circuit which changes the pulse shape most is a *RC* differentiation element [40] with a resonance frequency of $\omega \approx 430$ kHz. This element suppresses low frequencies to restore the baseline quickly. Thus the amplifier can deal with high rates. The impact of this RC-element is the last step included into the calculation of the transfer function. Finally the transfer function in Fig. B.6 is obtained.

Appendix C

The filter database

In order to keep track of all filters built for the use in ATLAS, a database was set up (Section C.1). This filter database can be administrated easily with a graphical user interface (Section C.2).

C.1 Filter database

The filter database was set up with `Oracle`. It consists of two tables: One table describes the filter cases, the other table describes filter fillings. The fields of these tables are shown in Tab. C.1 and Tab. C.2. Data can be added into the database either with `SQL` commands or with the graphical user interface described in the following section. The connection of the fields of these tables allows to calculate further properties of a filter, such as the full weight (sum of GASFILTER:WEIGHT and FILTERFILL:WEIGHT) of a filter or the weight increase during operation (difference of FILTERFILL:WEIGHT and FILTERFILL:REMVWEIGHT).

Field	Purpose
FILTERID	Unique ID for a filter case. Format: $20MGALUFiiiiii$
ASSDATE	Assembly Date: Date when the zeolite was filled in.
INSTDATE	Installation Date: Date when the filter was installed.
REMVDATE	Removal Date: Date when the filter was exchanged.
RACK	Number of the gas distribution rack, where the filter was installed.
CHANNEL	Gas channel on rack RACK, where the filter was installed.
WEIGHT	Empty weight of the filter case in grams.
LABELPRT	Counts the number of labels printed for this filter.
NOTE	Remarks on the installation.

Table C.1: *Fields of the the table* `GasFilter` *in the* `Oracle` *DB. iiiiii denotes a number between* 000001 *and* 999999*. A date has to be written in the format* $DD-MMM-YY$ *were* MMM *denotes the commonly used abbreviations for the corresponding month ("MAR" for march).*

Field	Purpose
ID	Unique ID for a filter filling. This number always increases.
FILTERID	Unique ID for a filter case. Format: $20MGALUFiiiiii$
INSTDATE	Installation Date: Date when the zeolite was filled in.
REMVDATE	Removal Date: Date when the zeolite filling was removed.
WEIGHT	Weight of the filling in gramme.
BATCH	Number of zeolite barrel.
REMVWEIGHT	Weight of the filling when removed.
SHIPFLAG	Used to mark filters before shipped to CERN.
NOTE	Remarks on the filling.

Table C.2: *Fields of the the table* `FilterFill` *in the* `Oracle` *DB. iiiiii denotes a number between* 000001 *and* 999999. *A date has to be written in the format* $DD-MMM-YY$ *were* MMM *denotes the commonly used abbreviations for the corresponding month.*

C.2 Graphical user interface

The Graphical User Interface (GUI), named "FilterManager.tcl", was programmed in `Tcl/Tk`. This software incorporates tools for the filter production, installation and exchange. As an example a screen shot of the installation tool can be found in Fig. C.1. Control structures of the programme and the underlying database prevent errors to a large extent[1]. Furthermore simple analysis tools are included into the "FilterManager.tcl". The plots shown in Fig. 7.16 were generated with this tool.

[1]Examples: Installation of empty filter cases, several filters for the same channel and rack at the same time, wrong weights of fillings and filter cases ...

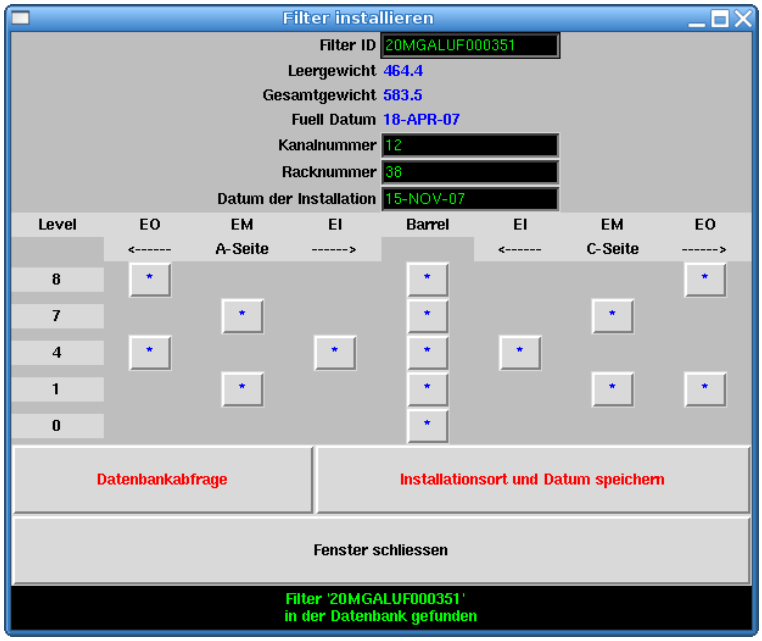

Figure C.1: *Screen shot of the filter installation tool. With buttons the gas distribution rack can be selected as installation location. The software allows the installation on only one filter per channel and rack at the same time.*

List of Figures

Bibliography

[1] Phys. Rev. Letters 97, 191801 (2006): Observation of Muon Neutrino Disappearance with the MINOS Detectors in the NuMi Neutrino Beam.

[2] ATLAS Inner Detector TDR Vol. 1, ATLAS TDR 4 CERN/LHCC 97-16, 30-Apr-1997, Inner Detector Community http://atlas.web.cern.ch/Atlas/GROUPS/INNER_DETECTOR/TDR/tdr.html

[3] taken from http://cdsweb.cern.ch/record/40525, copyright by CERN

[4] ATLAS Liquid Argon Calorimeter, Technical Design Report, 15 December 1996, ATLAS LARG Unit, CERN/LHCC 96-41, http://atlas.web.cern.ch/Atlas/GROUPS/LIQARGEXT/TDR/

[5] ATLAS Tile Calorimeter TDR, CERN/LHCC 96-42, 15-December-1996, ATLAS/Tile Calorimeter Collaboration http://atlas.web.cern.ch/Atlas/SUB_DETECTORS/TILE/TDR/TDR.html

[6] ATLAS Muon Spectrometer, TDR, 5 June 1997, ATLAS Muon Collaboration, CERN/LHCC 97-22 http://atlas.web.cern.ch/Atlas/GROUPS/MUON/TDR/Web/TDR_chapters.html

[7] ATLAS Collaboration: ATLAS Detector and Physics Performance TDR, CERN-LHCC 99-15, Geneva (1999) http://cdsweb.cern.ch/record/391177

[8] LEP-SLC: Standard modell fits to Z parameters from LEP/SLC data, 2005 http://pdg.lbl.gov/2007/listings/s055.pdf

[9] http://tevewwg.fnal.gov/higgs/

[10] Top physic prospects at LHC, Florian Beaudette, CERN, XLth Recontres de Moriond, http://moriond.in2p3.fr/EW/2005/Transparencies/3_Tuesday/2_evening/7_F_Beaudette/Beaudette.pdf

[11] ATLAS Muon Collaboration, Assembled Drift Tube, Internal Drawing ATLMMACA0031, Geneva 1999

[12] Claus Grupen, University of Siegen: Particle Detectors, Cambridge University Press (1996)

[13] H. Fischle, J. Heintze and B. Schmidt: Experimental determination of ionization cluster size distribution in counting gases, NIM A 301 (1991) 202-214

[14] W.R. Leo: Techniques for nuclear and particle physics experiments, Springer-Verlag (1994)

[15] F. Cerutti et al: Study of the MDT drift properties under different gas conditions, ATL-MUON-PUB-2006-004; ATL-COM-MUON-2003-022, CERN (2003)

[16] R. Veenhof: Garfield - simulation of gaseous detectors
`http://garfield.web.cern.ch/garfield/`

[17] Aufbau einer Apparatur und Messung der Gasverstärkung in den Driftröhren des ATLAS-Myondetektors, Staatsexamensarbeit, Karen Handrich, 1998, Universität Freiburg, Fakultät für Physik.

[18] M. Aleksa: Performance of the ATLAS Muon Spectrometer, PhD-thesis, Technische Universität Wien, 1999

[19] M. Deile, J. Dubbert, N.P. Hessey: Charge Division and Intrinsic Pulse Shaping in Drift Tubes, ATLAS Internal Note, MUON-NO-105 (1995)

[20] W. Blum, L. Rolandi: Particle Detection with Drift Chambers, Springer Verlag Berlin Heidelberg 1993

[21] S. Baranov, M. Bosman et al: Estimation of Radiation Background, Impact on Detectors, Activation and Shielding Optimization in ATLAS, ATL-GEN-2005-001, CERN (2005)

[22] John A. Kadyk: Wire chamber Aging, Nuclear Instruments and Methods in Physics Research A 300 (1991) 436-479

[23] C. Soll: Plasmapolymerisation von Hexamethyldisiloxan zur Abscheidung von quarzähnlichen Schichten bei gepulster Leistungszufuhr, Bergische Universität-Gesamthochschule Wuppertal, FB Elektrotechnik (2000)

[24] S. Zimmermann, C. Cernoch: MDT Ageing Studies - Results of the measurements conducted at the Gamma Irradiation Facility GIF between autumn 2001 and summer 2003

[25] S. Zimmermann: High Rate and Ageing Studies for the Drift Tubes of the ATLAS Muon Spectrometer, Dissertation, Universität Freiburg, March 2004

[26] K. A. Gerdes: Alterungsstudien an Driftröhren für das ATLAS Myonspektrometer, Diplomarbeit, Universität Freiburg, April 1999

[27] M. Kollefrath: Entwicklung, Aufbau und Durchführung von Alterungsuntersuchungen an Driftröhren für das ATLAS-Myonspektrometer, Dissertation, Universität Freiburg, Februar 1999

[28] S. Kircher: Parameter des Alterungsprozesses und der Reanimation von Driftröhren, Dissertation, Universität Freiburg, Mai 2001

[29] V. Paschoff: Studies on Ageing and Reanimation of Drift Tubes for the ATLAS Muon Spectrometer, Dissertation, Universität Freiburg, October 1999

[30] Christian Stegmann: The outer tracker for HERA-B, Desy-Zeuthen, Zeuthen, Germany

[31] A. Schreiner: Aging Studies of Drift Chambers of the HERA-B Outer Tracker Using CF_4-based Gases, Dissertation, Mathematisch-Naturwissenschafltiche Fakultät 1 der Humboldt-Universität Berlin (Juli 2001)

[32] J. Kadyk: Anode wire aging tests with selected gases, IEEE Transactions on Nuclear Science, Vol. 37, No. 2, April 1990

[33] J. Va'vra: Review of wire chamber ageing, Nuclear Instruments and Methods in Physics Research A252 (1986) p. 547-563.

[34] A. Kramer: Aufbau eines Alterungsexperimentes für Driftrohre zum Test von Gassystemkomponenten des ATLAS Myonspektrometers, Diplomarbeit (2004), Fakultät für Mathematik und Physik, Universität Freiburg

[35] Private communication with L. Schmidt (2004), responsible for radiation protection at Physikalisches Institut, Universität Freiburg.

[36] PT 100 Datasheet, available from
`http://www.thermocouple.co.uk/Downloads/TD-TV_PT1A.pdf`

[37] Benutzerhandbuch 1179/2179 Gasflussregler, MKS Instruments Deutschland GmbH (1996)

[38] MKS Massendurchflussmesser Typ 1259, Instruction Manual

[39] Bronkhorst Hi-Tec, Digital mass flow meters and controller for gases (1989)

[40] P. Rewierma, F/B-μChamber Frontend-Electronics. Nikhef, Amsterdam (1986).

[41] Isel Schrittmotor Controller C 142-4.1, Hardware-Beschreibung (1998)

[42] LeCroy CAMAC Model 2249A, Charge Sensitive 12-Channel ADC, Technical Information Manual (1975)

[43] LeCroy NIM 620 Series, 8-Channel Discriminator, Technical Information Manual (1975)

[44] LeCroy, Model 429A, Logic Fan-In/Fan-Out, Operator's Manual (1995)

[45] LeCroy, NIM Model 465/466, Triple 4-Fold Coincidence Units, Technical Information Manual (1974)

[46] S.E.N. Electronique: Timing Unit Model FE 276, Manual

[47] LeCroy, CAMAC Model 2551, 12-Channel 100 MHz Scaler, Operator's Manual (1983)

[48] S.E.N. Electronique, Outregister OR 2088, Manual

[49] M. Maassen: Planung und Aufbau der Regelung einer Strahlführung, Diplomarbeit, Freiburg (1999)

[50] Amersham Buchler GbmH & CoKG, Braunschweig, now QSA Global `http://www.qsa-global.com`

[51] Scott, Messerly, et al.: Hexamethyldisiloxane: chemical thermodynamic properties and internal rotation about the siloxane linkage, J. Phys. Chem., 1961, 65, 1320-1326.

[52] Eltec Elektronik Mainz, BAB-40/60 Basic Automation Board, Hardware Manual, Revision 1 A (1995)

[53] Hewlett Packard, HP 3488A Switch/Controll Unit, Operating, Programming and Configuration Manual, Model 3488 A (1983)

[54] Hewlett Packard, HP 3458A Multimeter Datasheet (1988)

[55] T. Haas: Ageing Phenomena in the LHCb outer tracker, NIM-A 581, Issues 1-2, 164-166, Physikalisches Institut, University of Heidelberg (2007), Transparencies:
`http://lhcb-doc.web.cern.ch/lhcb-doc/presentations/conferencetalks/postscript/2007presentations/Vienne_Haas.pdf`

[56] Private communication with Dr. Margraf (QSA-global).

[57] Amersham Catalogue 1981/1982: Construction plans of α-foils and α-sources.

[58] E. Brown & R.B. Firestone: Table of radioactive isotopes, John Wiley & Sons Inc., USA (1986)

[59] ESTAR Database on the web
`http://physics.nist.gov/PhysRefData/Star/Text/ESTAR.html`

[60] ASTAR Database on the web
`http://physics.nist.gov/PhysRefData/Star/Text/ASTAR.html`

[61] XCOM Database on the web
`http://physics.nist.gov/PhysRefData/Xcom/Text/XCOM.html`

[62] J. Heintze: Die Röntgen-K-Fluoreszenzausbeute des Neon, Argon, Krypton und Xenon, II. Phys. Institut der Univ. Heidelberg (1955).

[63] F. Hahn et al.: Engineering layouts for the ATLAS Muon Gas System Modules, ATC-TG-EP-002, Cern (2002)

[64] W. Kast: Adsorption aus der Gasphase, VCH Verlagsgesellschaft, Weinheim (1988)

[65] H. Kuchling: Taschenbuch der Physi, 18. Auflage, Fachbuch Verlag Leipzig (2004)

[66] Private communication with Dr. Unger (Chemiewerke Bad Köstritz). `http://www.cwk-bk.de`

[67] Molecular sieve Koestrolith UK8, Product Datasheet, Chemiewerke Bad Köstritz (05/06)

[68] G. Sprachmann: Aging and Gas Filtration Studies in the ATLAS Transition Radiation Tracker, Vienna (2006), CERN-THESIS-2007-005

[69] Private communication with Sandro Palestini (CERN).

[70] `http://detector-gas-systems.web.cern.ch/detector-gas-systems/Equipment/ componentValidation.htm` → Link `Ageing Test result (pop up)`
The Voegtlin Rotameter can be found as Sample 2004, Prototype 25.

[71] A. D'Auria: P&I Drawing, General MDT distribution rack layout (2004)

[72] Private communication with Andrea Kramer, IKZ Berlin (2005).

[73] Private Emails with F. Hahn (CERN gas group).

[74] Hyco Vakuumtechnik GmbH: Betriebsanleitung Membranpumpe Baureihe LAB, 82152 Krailing, Germany (2000)

[75] F. Ahles: Entwicklung einer Gasüberwachung für das ATLAS Myonsystem durch präzise Messung der Driftgeschwindigkeit, Diplomarbeit, Physikalisches Institut der Universität Freiburg (2006).

[76] S. Koenig: Entwicklung einer Testkammer und Datenaquisition für den Freiburger Höhenstrahlteststand, Diplomarbeit, Physikalisches Institut der Universität Freiburg (2003).

[77] J. Dubbert: Private communication with Jörg Dubbert (CERN, MPI Munich).

Acknowledgements

I would like to express my gratitude to many colleagues for supporting me with the work concluded in this thesis.
In particular, I would like to thank Prof. Gregor Herten for giving me the opportunity to carry out a PhD in his department and for his support, in particular when important decisions about the exigence for ageing tests were needed. A very special thanks goes to Bernhard Pfeifer: With his help the filters were constructed and installed into the gas distribution lines. I will never forget our dinners in the restaurant *Nova* in Divonne-les-bains and the discussions afterwards in "our" *Hotel-du-Parc* in Gex. I would also like to thank Jürgen Tobias for his helping hand and his experience with electronic circuits.
My former colleague Andrea Kramer worked with me on the construction of the component test. Even beyond this, she helped me by making SEM pictures of wires and performing EDX analyses.
The layout of the component test was significantly influenced by the experience of Michael Kollefrath with previous ageing tests. I am grateful for his support and the many important and interesting discussions about the mysteries of ageing. The same can be said for Wolfgang Mohr and Ulrich Landgraf. Their vast experience in experimental particle physics made my life a lot easier. A big thanks goes to my colleagues in the office, Florian Ahles and Song Xie for making our office the place to be.
Many thanks also to Tobias Raufer; he reduced the number of mistakes in this thesis significantly.
Some experiments would not have been possible without the help of people at CERN. In particular I would like to thank Gerald Sprachmann from the TRT group and Ferdinand Hahn from the CERN gas group. For the development and installation of the filters further helpful support was given by Thomas Meyer and Jan Godlewski.
Finally, it is very important for me to also thank my family and my girl-friend Nicole for supporting me during this thesis. Sometimes it may have seemed that I ignored them because I was too busy with my work. Thanks so much for your love and support!